ABSTRACT

Title of Dissertation: LIGHT ABSORBING AEROSOLS: CALIBRATION, MEASUREMENTS, AND EMISSIONS FOR NEW YORK CITY

Courtney D. Grimes, Doctor of Philosophy, 2021

Dissertation directed by: Professor Russell R. Dickerson, Department of Atmospheric and Oceanic Science & Department of Chemistry

Light absorbing aerosols such as black carbon (BC) impact weather, climate, and human health. Several instruments have been developed to measure light absorbing aerosols. Filter-based techniques, due to the simplicity of operation, are used on airborne platforms and ground sites across the globe. One such instruments, the Aethalometer, determines the attenuation of light passing through a filter but is known to have inherent errors that need to be corrected. One part of this dissertation focuses on characterizing BC instruments in the laboratory using a well-studied BC surrogate and other atmospherically relevant aerosols. The second part focus on measurements of light absorbing, ambient aerosols to evaluate emissions inventories.

I characterize BC instrumentation using a commercially available BC surrogate, Cab-O-Jet 200. This BC surrogate was first size selected at 300 nm mobility diameter, and then the particle mass, m_p, was determined with an aerosol particle mass analyzer (APM). A condensation particle counter (CPC) served as a

reference method for measurement of number concentration, N_p; when multiplied by m_p, N_p gives the mass concentration. I evaluated an Aethalometer (Model AE31) as a function of particle loading, size, wavelength, and coating. Uncertainty in filter-based BC measurements increases substantially for BC particles coated with minimally absorbing ammonium sulfate or with brown carbon (BrC). A Thermal optical absorbance (TOA) instrument was also characterized with a binary, aqueous mixture consisting of the same BC surrogate plus sucrose to test separation of elemental carbon (EC) from organic carbon (OC). A Model AE33 Aethalometer was also successfully evaluated with particles from the BC surrogate, and it performed with good accuracy when compared to in-situ laboratory measurements.

Ambient measurements of light absorbing aerosols from campaigns in Xingtai, China were used to determine the mass absorption cross section (MAC) – critical to understanding radiative forcing and climate. Relatively high ambient MAC values in Xingtai, China were found by using airborne data from the single particle soot photometer (SP2) and the particle soot absorption photometer (PSAP). Particles from Xingtai were also collected on filters and classified using Scanning electron microscopy and energy dispersive X-Ray (SEM-EDX); both BC and mineral dust were found. Using a well characterized Aethalometer for BC mass concentration, total BC emissions from the NYC region were calculated from ambient BC/CO ratios and emission inventories of CO. Results indicate BC emissions are somewhat underestimated in existing inventories, suggesting issues of environmental health and justice.

LIGHT ABSORBING AEROSOLS: CALIBRATION, MEASUREMENTS, AND EMISSIONS FOR NEW YORK CITY

by

Courtney D. Grimes

Dissertation submitted to the Faculty of the Graduate School of the
University of Maryland, College Park, in partial fulfillment
of the requirements for the degree of
Doctor of Philosophy
2021

Advisory Committee:
Professor Russell R. Dickerson, Chair
Professor Neil Blough
Dr. Xinrong Ren
Professor Alice Mignerey
Professor Akua Asa-Awuku
Dr. Joseph Conny

Dedication

I dedicate this work to my dearest family. I am so thankful for their love throughout this journey. I am extremely grateful for my parents who love me unconditionally. Mom, thank you for showing me the importance of perseverance. Dad, thank you for showing me the value of true hard work. Thank you both for being my rock through all my trials and joys. No words can truly express my gratitude. I would also love to thank my older sisters, Tiffany, and Brittney. They have been my best friends since the beginning. I am so appreciative of their love, guidance and support.

I would also like to dedicate this work to my extended family. I truly appreciate the **prayers**, wisdom and care packages made to make me remember that I am truly loved.

Acknowledgements

I would first like to give all honor and Glory to God for His provision during this journey. I would also love to thank the many people for helping me be where I am today.

As for people, I would first like to thank and acknowledge my advisor, Professor Russell Dickerson for all his guidance, support, and care. I deeply appreciate his patience with me throughout my years as a graduate student in his lab. Dr. Dickerson's passion for atmospheric science was so contagious to everyone in the group. I will never look at atmospheric chemistry the same! His encouragement has truly shaped me into the scientist that I am today. I will forever be thankful for his teachings and advice in the lab, and about life in general. I was truly blessed to be a member of his group.

I am very grateful to Dr. Xinrong Ren during my years at UMD. I have learned so much from him about flight and field campaigns. His work ethic is truly admirable. I will miss those days installing instruments on the Cessna at Tipton airport. I would like to express my gratitude towards Professor Akua Asa-Awuku for allowing me to work in her lab to finish up some aerosol studies. She truly took me under her wing, and kindly allowed me to work with her awesome postdoc, Dr. Qi Yao. I am forever thankful for her mentorship, and support. Thanks to Prof. Zhanqing Li and Dr. Hao He for help with securing aerosol samples from China, and to the MPI research group of Dr. Yafang Cheng for SP2 data.

I would also like to thank Dr. Joseph Conny for his support during my time as a guest researcher at NIST. Dr. Conny was so kind and patient with me as I worked in

his lab. I am truly grateful for his mentoring, care and encouragement. His positive outlook on the nature of scientific research is something I will take with me for the rest of my life. Next, I would like to thank Dr. Christopher Zangmeister and Dr. James Radney for allowing me to use their equipment in their laboratory at NIST. I am very thankful for their guidance on how to be a strong researcher, and I appreciate their guidance on understanding aerosol science. I owe sincere gratitude towards Dr. Robert Willis at the EPA. I would not have been able to complete the SEM-EDX work without him. I would also like to thank Gary Norris of the EPA for loaning the Model AE31 Aethalometer. Thank you to Dr. Brian McDonald (NOAA) for his work with emission inventories in the New York City region.

I owe great thanks to Professor Neil Blough and Professor Alice Mignerey for serving on my committee. I appreciate their patience concerning the defense date, and their advice during my time in the PhD program.

Additionally, I owe my sincerest gratitude towards my mentor Dr. Alicia Cheek. I am thankful for her taking the time out of her busy life to talk to me whenever I needed advice. I have been blessed to have her in my life encouraging me continuously. Seeing her complete her doctorate as a fellow black woman in the sciences has been so inspiring to me. I would gladly like to thank Dr. Marcus Carter too. He has been extremely helpful with tackling obstacles during my time as a graduate student.

Lastly (and certainly not least), I want to deeply thank my dearest family. The Lord has blessed me with loving, supportive parents who taught me to never give up. My mom and dad stressed the importance of education, and I am eternally grateful for

that lesson. My two older sisters have been my rock. I appreciate the joy, love, and happiness they bring in my life every single day (despite being 220 miles away).

Table of Contents

Dedication ii
Acknowledgements iii
Table of Contents vi
List of Tables viii
List of Figures ix
List of Acronyms xiv
Chapter 1: Introduction 1
1.1 Light Absorbing Aerosols 5
1.1.1 BC and Terminology 5
1.1.2 BrC and Mineral Dust 10
1.2 Background of Light Absorption by aerosols 11
1.2.1 Basic theory of absorption 11
1.3 BC instrumentation 13
1.3.1 Need for a reference material 13
1.3.2 Aethalometer 13
1.3.3 Particle Soot Absorption Photometer 18
1.3.4 Single Particle Soot Photometer 19
1.3.5 Thermal Optical Analysis 20
1.4 Instrumentation used for characterization 22
1.4.1 Differential Mobility Analyzer 22
1.4.2 Aerosol Particle Mass Analyzer 25
1.4.3 Condensation Particle Counter 25
1.4.4 Scanning Electron Microscopy 27
1.4.5 Aerosol Aerodynamic Classifier 28
1.5 Scope of this Dissertation 30
Chapter 2: Evaluation of a filter-based black carbon (BC) instrument using a brown carbon (BrC) surrogate as well as pure and coated BC surrogates (Accepted 2020, *Aerosol Science and Technology*) 33
2.1 Introduction 33
2.2 Materials and Methods 37
2.2.1 Aerosol Generation 39
2.2.2 Thermal Optical Analysis and SEM 39
2.2.3 Determination of Particle mass 40
2.2.4 Tandem DMA 40
2.2.5 Comparison of CPC to Aethalometer 41
2.2.6 Uncertainty Analysis (CPC) and Limit of Detection (Aethalometer) 42
2.3 Results 42
2.3.1 Evaluation of the performance of the Aethalometer: Low mass concentrations. 42
2.3.2 Wavelength Response for the BC Surrogate & *SG* Correction Factors 45
2.3.3 Evaluation of the performance of the Aethalometer: Larger range of BC mass concentrations. 47

2.3.4 BC Coating with Ammonium Sulfate 51
2.3.5 Brown Carbon Absorptivity 52
2.3.6 Coated with a BrC surrogate 53
2.4 Discussion 55
2.5 Conclusions 57
Chapter 3: Evaluation of Thermal Optical Analysis (TOA) using an aqueous binary mixture (Published 2020, *Atmospheric Environment*) 59
3.1 Introduction 59
3.2 Materials & Methods 61
3.3 Results and Discussion 61
3.4 Results and Discussion 66
Chapter 4: Ground and aircraft-based measurements of black carbon (BC) and carbon monoxide (CO) in the New York City (NYC) metropolitan area: Comparison to emissions inventories. *This chapter is an advanced copy of a paper to be submitted to Environmental Science and Technology 68
4.1 Introduction 68
4.2 Materials & Methods 72
4.2.1 Laboratory Evaluations of the Aethalometer using a BC surrogate 72
4.2.2 Ambient Measurements in the NYC Area 74
4.3 Results and Discussion 76
4.3.1 Calibration and characterization with 200 nm BC particles 76
4.3.2 Wavelength dependence of the Aethalometer 78
4.3.4 Measured BC and CO at the Near Road (NR) site in Queens, Summers 2018 and 2019 85
4.3.5 Emission values for BC and CO in the NYC metropolitan area 90
4.4 Conclusions 93
Chapter 5: Strong light absorption by atmospheric particles in the planetary boundary layer over Hebei, China derived from aircraft observations 95
5.1 Introduction 95
5.2 Materials & Methods 97
5.3 Results 99
5.4 Discussion 105
5.5 Conclusions 107
Chapter 6: Characterization of Particulate Matter in Xingtai, China using Scanning Electron Microscopy (SEM) and Thermal Optical Analysis (TOA) for Source Identification 109
6.1 Introduction 109
6.2 Materials and Methods 110
6.2.1 Site description 110
6.2.2 Sample Description 111
6.2.3 Computer Controlled SEM 112
6.2.4 Thermal-Optical Transmission (TOT) Analysis 114
6.2.5 Back Trajectory Analysis 115
6.3 Results and Discussion 117
6.3.1 Data Reduction 117
6.3.2 Carbonaceous Species of Particulate Matter 122

6.4 Conclusions 124
Chapter 7: Conclusion and Future Work 126
Appendices 131
A. Supplemental Information for Chapter 2 131
A.1 Determining the Contribution of Particles Possessing a charge (q) > +1 .. 131
A.2 Correcting Data Using the Jimenez Correction 132
A.3 BC Coated with Ammonium Sulfate 135
B. Supplemental Information for Chapter 4 138
B.1 Theory and Calculations: Tandem DMA and AAC to determine Particle Mass 138
B.2 Intercomparison of the filter-based and the CPC mass concentration for 300 nm particles 139
B.3 Wavelength dependence of the AE 33 model for 300 nm particles 140
B.4 Determining the 24 hour average of BC and CO at the Queens NR site during Summers 2018 and 2019 141
Bibliography 144

List of Tables

Table 1.1 *Instrumentation used in this dissertation and brief description……32*

Table 2.1 *Calculated SG values (and standard deviations) for three separate runs with 300 nm Cab-O-Jet particles for mass concentration up to ≈2.5 μg m^{-3}. Also shown is the percent deviation from the manufacturer's constant values for SG at multiple wavelengths..... 46*
Table 2.2 *Best fit slope (where the y-intercept is forced through zero) values for BC up to 2.5 μg m^{-3} for the raw data and the data corrected for the newly determined SG values. 46*
Table 2.3 *Best-fit slope (where the y-intercept is forced through zero) values up to 20 μg m^3 for the raw data and the data corrected for the shadowing effect and newly determined SG values. 50*
Table 2.4 *Values of the slope and 1σ when the y-intercept is forced through zero for the multiple mass fractions of BC with AS. Best fit correction factors are the inverse of these slope values..... 51*

Table 3.1 *Temperature steps and residence times for the NIST-EPA-A,-B and -C protocols…… 65*
Table 3.2 *Temperature steps and residence times of the Quartz protocol. 65*
Table 3.3 *Averages and standard deviations of OC, EC, TC and EC/TC for different temperature protocols compared to the calculated reference values. Uncertainties of the reference values are propagated errors from glassware and the balance used for volume and mass measurements. The numbers of replicates are given by n..... 65*

Table 4.1 *Measured BC and CO data from the LISTOS flights. The linear least-squares regression fits are from the BC/CO correlations. The CO concentrations are*

plotted as the independent variable and the BC mass concentrations are the dependent variable……81

Table 4.2 *Linear regression fits for BC equivalent mass concentrations at 370nm (BC_{UV}, dependent variable) vs. BC mass concentrations at 880 nm (independent variable)..... 83*
Table 4.3 *The average, standard deviation (STD, 1σ), standard deviation of the mean, maximum and minimum values for 1 hour averages of BC and CO concentrations. All values are from the Queens NR site during the summers of 2018 and 2019..... 86*
Table 4.4 *Total emission values of CO and BC (or EC for NEI) in the NYC metropolitan area. BC emission values from the Cessna aircraft and Queens NR site were calculated using the CO emissions from the bottom up inventories (NEI and FIVE) and the ambient ΔBC/ΔCO ratios..... 92*

Table 5.1 *Experimental studies determining the MAC of BC. Table is from Nordmann et al. 2013……97*

Table 5.2 *Average values of BC mass concentration from the SP2 and Absorption coefficients from the PSAP. The MAC values for each flight are also provided. Uncertainty is standard error of the slope of the linear regression. 101*
Table 6.1 *Classification rules for ambient particles collected in Xingtai using hierarchical analysis involving elements..... 112*
Table 6.2 *Temperature steps and residence times for the Quartz and NIST-EPA-C protocols. 115*
Table 6.3 *The percentages of particles assigned to each class. 120*
Table 6.4 *Average and standard deviation values (1σ) for the concentrations of OC, EC, TC and EC/OC..... 124*

Table A1 *Mass concentration ranges measured by the Aethalometer are provided along with ATN ranges at λ= 880 nm. The linear regression coefficients are shown above for the varying mass concentrations that exhibited a non-linear response due to the shadowing effect.....* 135
Table B1 *The average, standard deviation (STD, 1σ), standard deviation of the mean, maximum and minimum values for 24 hour averages of BC and CO concentrations. All values are from the Queens NR site during the summers of 2018 and 2019. .....* 141

List of Figures

Figure 1.1 *An illustration of the possible interactions between a particle and incident radiation.[6] .....* 2
Figure 1.2 *An image of aerosol optical thickness using MODIS data. The red color represents fine or small particles from pollution, and smoke. The yellow color*

represents coarse or large particles that are typically associated with desert dust (source Robert Simmon, NASA Earth Observations). 3

Figure 1.3 *BC's role in the climate system. Also shown are the major sources and sinks of BC.* 6
Figure 1.4 *Carbonaceous aerosol classified according to their thermochemical and optical properties.*[9] 8
Figure 1.5 *The Structure of Graphene. It has a honeycomb lattice with sp2 carbons.*[38] 9
Figure 1.6 *Aerosol laden air is deposited on the filter with a certain spot area. The light detectors are meant to measure the transmission of light through the filter.*[46] .. 14
Figure 1.7 *Schematic diagram of the PSAP.*[49] 18
Figure 1.8 *Schematic of the SP2 instrument. Shown are the optics, incandescence and scattering detectors of the instrument.*[53] 20
Figure 1.9 *Schematic Diagram of the Sunset Thermal Optical Carbon Analyzer. Filter samples can be either 1.0 cm^2 or 1.5 cm^2.*[55] 22
Figure 1.10 *The Differential Mobility Analyzer. This instrument size selects based on electrical mobility. (www.cac.yorku.ca)* 24
Figure 1.11 *Schematic diagram of the Condensation Particle Counter (Condensation Particle Counters. Centre For Atmospheric Science). The CPC determines total number concentration.* 26
Figure 1.12 *Schematic diagram of the components of the SEM instrument.* 27
Figure 1.13 *Schematic diagram of the components of the AAC instrument. Q_a is the aerosol flow, Q_{sh} is the sheath flow rate, Q_{exh} is the exhaust flow rate, Q_s is the sample flow rate and ω is the rotational speed.*[58] 30

Figure 2.1 *Schematic diagram of the experimental setup for comparisons between the Aethalometer and the CPC. Aerosols were generated through liquid atomization before entering the DMA to select the mobility diameter (in this case 300 nm). Mass distributions were measured to determine particle mass with a removable APM in line. The CPC measured aerosol N_p, while the filter-based instrument or Aethalometer measured BC mass concentration.* *38*
Figure 2.2 *(a) Correlation of CPC mass concentration with eBC (BC equivalent mass concentration: μg m^{-3}) at three different instrumental wavelengths: 370, 660 and 880 nm. Observations are for low mass concentrations (< ≈2.5 μg m^{-3}) for particles with a mobility diameter of 300 nm. (b) Correlation at low mass concentrations with corrected SG values (described above). Intercepts of best-fit lines were forced to zero. Less than a 1% impact was observed on the slope.* *44*
Figure 2.3 *Results for eBC up to ≈20 μg m^{-3} (a) Correlation of CPC-determined mass concentration with uncorrected filter-based eBC. (b) Correlation of CPC mass concentration eBC up to 20 μg m^{-3} with only the loading correction (described in Appendix A) applied. (c) Correlation of CPC mass concentration with eBC with both the loading correction and corrected SG applied.* *49*

Figure 2.4 *Response of Aethalometer at 370 nm (blue diamonds), 660 nm (red squares) and 880 nm (black circles) to the CPC-derived BC using a 14% BC mass fraction solution with BrC. The coating causes a positive interference that increases at shorter wavelengths.* *54*
Figure 3.1 *Thermograms produced in response to the binary solution with a reference TC value of 15.03 μg/cm^2 and EC/TC ratio 0.213. The red solid line is the split point, the blue dashed lines are the temperature steps. The black solid line is the FID response. Thermograms using (a) NIST-EPA-A (reported values of TC=15.19 μg/cm^2 and EC/TC=0.215); (b) NIST-EPA-B (reported TC=14.89 μg/cm^2 and EC/TC=0.209); (c) NIST-EPA-C (reported values of TC=15.17 μg/cm^2 and EC/TC=0.222); (d) Quartz (reported values of TC=15.51 μg/cm^2 and EC/TC=0.218).* *64*

Figure 4.1 *Schematic diagram of the experimental setup for comparisons between the AE33 and the CPC. Aerosols were generated through liquid atomization and conditioned by a heater (100 °C) and diffusion dryer. The AAC generated monodisperse aerosol with aerodynamic diameters of 200 nm and 300 nm. The condensation particle counter (CPC) measured aerosol number density, while the AE33 measured BC equivalent mass concentration at multiple wavelengths. The DMA (component of SMPS) was used in tandem with the AAC for particle mass determination.* *73*
Figure 4.2 *Correlation of CPC mass concentration with the Aethalometer BC mass concentration (λ=880 nm). Particles had an aerodynamic diameter of 200 nm. Data points are averages of the entire run, and the error bars are 1σ. The dashed line shows 1:1. The root mean squared error is 0.48 μg m^{-3}, or approximately 8%.* *78*
Figure 4.3 *Wavelength response to 200 nm particles during one 45 minute run at 7 different wavelengths. All error bars are 1σ. The red data point is representative of BC measured at 880 nm.* *79*
Figure 4.4 *a) Flight tracks for the LISTOS flight campaign in 2018. Green is 1 July 2018, blue is 2 July 2018, yellow is 15 August 2018 and magenta is 16 August 2018 (b) Flight tracks for the LISTOS flight campaign in 2019. Red is 19 June 2019, green is 20 June 2019, blue is 21 June 2019, yellow is 22 June 2019 and magenta is 29 June 2019.* *80*

Figure 4.5 *Correlations of BC mass concentration (y-axis) and CO mixing ratio (x-axis) for each flight during the LISTOS campaign. Circles are 1-minute averaged data below 1000 m. (a) 1 July 2018 (Sunday); (b) 2 July 2018 (Monday); (c) 15 August 2018 (Wednesday); (d) 16 August 2018 (Thursday); (e) 19 July 2019 (Friday); (f) 20 July 2019 (Saturday); (g) 21 July 2019 (Sunday); (h) 22 July 2019 (Monday); and (i) 29 July 2019 (Monday). The average weekend ΔBC/ΔCO ratio is 4.19 ± 0.14 and the average weekday ratio is 7.66 ± 1.25 ng m^{-3} ppb^{-1}.* *82*

Figure 4.6 *Relationships between BC and CO for summers 2018 and 2019. Blue circles are 1-hour averaged data. (a) Weekday data for summer 2018 (b) Weekend data for summer 2018 (c) Weekday data for Summer 2019 (d) Weekend data for Summer 2019. ..... 87*
Figure 4.7 *(a) Counts of cars on the Long Island Expressway (LIE) during weekdays and the weekend. (b) Counts of trucks on the LIE during the weekdays and weekends. 90*

Figure 5.1 *Scatterplots of the absorption coefficient from the PSAP on the y-axis, and BC mass concentration from the SP2 on the x-axis for the research flights conducted on (a) 20160517 (b) 20160519 (c) 20160528 (d) 20160611. Slopes determined by linear regression analysis are equivalent to the MAC..... 103*
Figure 5.2 *Back trajectories during the flights on (a) 20160517 (b) 20160519 (c) 20160528 (d) 20160611. These back trajectories were provided courtesy of Sarah Benish, PhD. 104*

Figure 6.1 *Xingtai's location with respect to other major cities in China (Source Z. Li)……111*
Figure 6.2 *HYSPLIT 24 hour back trajectories initiated at 500 m altitude (mid-PBL) for (a) 16 May 2016 (b) 17 May 2016 (c) 18 May 2016 and (d) 21 May 2016. 104*
Figure 6.3 *SEM images of particles that represent each class and their respective average diameter: a) aluminum silicate (coal fly ash particle, 1.58 μm) b) Mixed aluminum silicate (1.71 μm) c) Quartz (4.88 μm) d) calcium rich particle (3.87 μm) e) calcium sulfate (gypsum, 2.28 μm) f) carbon rich (soot aggregate, 2.29 μm) g) iron oxide (3.96 μm) h) metals (Cu, 1.40 μm) i) miscellaneous (calcium phosphate, 3.10 μm)……121*

Figure A1 *An example of the distribution of the 1:1000 dilution of the BC surrogate with Tandem-DMA within a range of 250 nm to 650 nm. The first DMA set to an electrical mobility diameter of 300 nm. The prominent peak at ~300 nm represents particles with a +1 charge and the smaller peak at ~500 nm are particles possessing a charge of +2..... 132*
Figure A2 *Mass Shown above is an example of how the linear regression coefficients are calculated during one run. Loading correction linear regression coefficients are defined where T is on the x-axis while K(ATN) is on the y-axis: a=0.17 (y-intercept) b=0.90 (slope)..... 133*
Figure A3 *Time series BC data where the shadowing effect is observed. The uncompensated data is depicted with black diamonds while the corrected data is depicted by red triangles. The in-situ CPC data is shown by the blue circles. 134*
Figure A4 *(a) Correlation of CPC mass concentration with eBC with a 7% BC mass fraction solution with ammonium sulfate. Three different instrumental wavelengths are represented: 370 (blue diamonds), 660 (red squares) and 880 nm (black circles).*

(b) Correlation of CPC mass concentration with eBC at 880 nm using a 14% BC mass fraction solution with ammonium sulfate. (c) Correlation of CPC mass concentration with eBC at 880 nm using a 20.5% BC mass fraction solution with ammonium sulfate. *136*

Figure B1 *Correlation of CPC mass concentration with the Aethalometer BC mass concentration (λ=880 nm). Particles had an aerodynamic diameter of 300 nm. Data points are averages of the entire run, and the error bars are 1σ.* 140
Figure B2 *Wavelength dependence for a 300 nm particle during one 45 minute run at 7 different wavelengths. All error bars are 1σ.*..... 141
Figure B3 *FIVE (a) BC emissions and (b) CO emissions for the NYC region. Color bar denotes the tons per day of emissions. The outlined area is the region of study.* ……*142*

List of Acronyms

AAE: Absorption Ångström Exponent; Also referred to as A_bAE in Chapter 2

AS: Ammonium Sulfate

A_{tt}AE: Attenuation Ångström Exponent

ATN: Attenuation

BC: Black Carbon

BC_{mass}: Black Carbon mass concentration

BrC: Brown Carbon

BSE: Backscattered Electrons

CO: Carbon Monoxide

COSMOS: Continuous Soot Monitoring System

CCN: Cloud Condensation Nuclei

DPF: Diesel Particulate Filter

eBC: Equivalent Black Carbon

E_{BC}: Black Carbon Emissions

EC: Elemental Carbon

E_{CO}: Carbon Monoxide Emissions

EDGAR: Emissions Database for Global Atmospheric Research

EDX: Energy Dispersive X□ray Spectroscopy

FIVE: Fuel-based Inventory of motor-Vehicle Emissions

HULIS: Humic-Like Substances

IMPROVE: Interagency Monitoring of Protected Visual Environments

IN: Ice Nuclei

IPCC: Intergovernmental Panel on Climate Change

IR: Infrared

LAC: Light Absorbing Carbon

LII: Laser Induced Incandescence

LISTOS: Long Island Sound Tropospheric Ozone Study

LPM: Liters per Minute

MAAP: Multi-Angle Absorption Photometer

MAC: Mass Absorption Cross Section

MODIS: Moderate Resolution Imaging Spectroradiometer

MOVES: Mobile Vehicle Emission Simulator Model

m_p: Particle Mass

NEI: National Emissions Inventory

NOAA: National Oceanic and Atmospheric Administration

OA: Organic Aerosol

OC: Organic Carbon

OC:EC: Organic Carbon to Elemental Carbon

PAH: Polycyclic Aromatic Hydrocarbon

PBL: Planetary Boundary Layer

PSAP: Particle Soot Absorption Photometer

PM: Particulate Matter

$PM_{2.5}$: PM with an aerodynamic diameter less than or equal to 2.5 micrometers

PM_{10}: PM with an aerodynamic diameter less than or equal to 10 micrometers

rBC: Refractory Black Carbon

SE: Secondary Electrons

SEM: Scanning Electron Microscopy

SOA: Secondary Organic Aerosols

SP2: Single Particle Soot Photometer

SSA: Single Scattering Albedo

Tg: Teragram

TOA: Thermal Optical Analysis

TOR: Thermal Optical Reflectance

TOT: Thermal Optical Transmittance

UV: Ultraviolet

VOC: Volatile Organic Carbon

Chapter 1: Introduction

Atmospheric aerosols are an important component to the Earth's climate system and a threat to human health. Aerosols, a suspension of particles or liquids within a gaseous medium, arise from anthropogenic and natural sources. Some of these natural sources include sea spray, volcanoes, and windborne/mineral dust, while the major anthropogenic source is fuel combustion.[1] Aerosols can range in size from a few nanometers (nm) to tens of micrometers. Federal agencies often refer to these particles as particulate matter, $PM_{2.5,}$ or PM_{10}, depending on the size. Particles classified as $PM_{2.5}$, or particles of an aerodynamic diameter less than 2.5 μm, are called "fine," while particles greater than 2.5 μm are generally referred to as "coarse" particles. Primary aerosols are emitted directly into the atmosphere as particles (dust, black carbon etc.) and secondary aerosols (sulfates, nitrates etc.) are formed through gas-to-particle conversions in the atmosphere over time.[2, 3] Atmospheric particles can also impact precipitation patterns by serving as cloud condensation nuclei (CCN) and ice nuclei (IN) in supersaturated air.[4, 5] Air particulate matter is comprised primarily of sulfate, ammonium, sea salt, nitrate, mineral dust, elemental carbon, and organic carbon.[3]

Aerosols impact Earth's radiative budget through several potential interactions with light. Figure 1.1 depicts the many ways a particle can interact with electromagnetic radiation.[6] Refraction, diffraction and reflection comprise elastic scattering, while absorption of radiation can also occur. When particles absorb electromagnetic radiation, they fluoresce or re-radiate the absorbed energy as thermal emission.

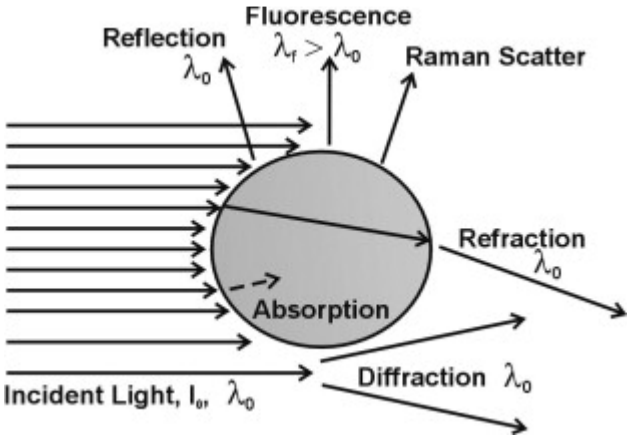

Figure 1.1 *An illustration of the possible interactions between a particle and incident radiation.*[6]

The net radiative forcing of atmospheric aerosols is negative (or cooling) due to scattering aerosols. Radiative forcing, used to compare climate impacts, is defined as a change in Earth's radiation balance. It is believed that aerosol radiative forcing ranges from -0.3 to -2.1 Wm^{-2} at the 90% confidence level.[7, 8]

Although the net aerosol radiative forcing is negative, there are aerosols that have a net radiative forcing that is positive (warming). These aerosols absorb light and convert electromagnetic energy into thermal energy, and thus heat up the atmosphere. Some of these light absorbing aerosols include mineral dust, black carbon (BC, commonly referred to as soot, or elemental carbon, EC), and brown carbon (BrC). BC is believed to be the second leading cause of global warming (on par with methane). Studies have shown that present day warming from BC is within the range of 0.3°C-0.4°C.[9-11] BrC is a light-absorbing organic carbon that is comprised of humic-like substances and usually appearing yellowish brown in color. BrC strongly absorbs in the ultraviolet, and has a strong wavelength dependence for

absorption. The magnitude of radiative forcing of BrC is approximately 25% (0.1−0.25 W m^{-2}) the radiative forcing of BC (1.07 W m^{-2}).[9, 12] Both light absorbing carbonaceous particles are known to affect the formation of clouds and reduce surface albedo on snow and ice.[13, 14] Figure 1.2 shows the aerosol optical thickness globally using the Moderate Resolution Imaging Spectroradiometer (MODIS). Aerosol optical thickness measures extinction (absorption + scattering) within a vertical column of the atmosphere.

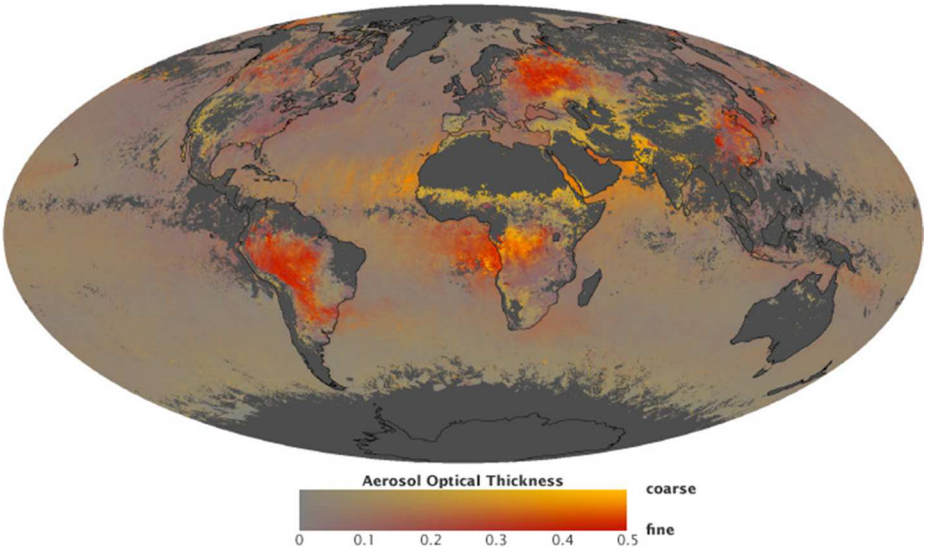

Figure 2.2 *An image of aerosol optical thickness using MODIS data. The red color represents fine or small particles from pollution, and smoke. The yellow color represents coarse or large particles typically associated with desert dust (source Robert Simmon, NASA Earth Observations).*

Several techniques are used to quantify light absorption by aerosols. The most frequently used techniques include the filter-based methods such as the Aethalometer (Magee Scientific, Berkeley, CA)[15, 16] Particle Soot Absorption Photometer (PSAP, Radiance Research, Seattle, WA),[17] and Multi-Angle Absorption Photometer (MAAP).[18] With these techniques, aerosol is deposited onto a filter by pulling a

known flow rate of air through it. The change in attenuation of light through the filter is then interpreted as light absorption. However, because a filter substrate is involved in the measurements, there are known artefacts associated with these instruments, and they need to be addressed. Systematic errors include: 1) an enhancement of attenuation from multiple scattering from the filter fibers and non-absorbing particles (multiple scattering correction) and 2) a non-linear response of attenuation with an increase of aerosols loading (shadow effect).[17, 19-21] Concomitant nephelometer scattering measurements are sometimes necessary. My research focused first is developing calibration procedures for these filter-based instruments, and the characterization of light absorbing aerosols.

BC is known to have a variety of names within the aerosol community. The different terminology is based on the method of measurement or characterization. BC is commonly referred to as elemental carbon (EC), when using thermal optical analysis (TOA) for measurement.[22-24] This technique differentiates EC from OC, however, different temperature protocols of TOA produce inconsistent EC and OC. BC is a refractory material where vaporization temperatures are as high as 4000K. Depending on the method of measurement, BC can also be referred to as refractory black carbon (rBC). The single particle soot photometer (or the SP2, Droplet Measurement Technologies, Longmont, CO) retrieves rBC mass concentrations through laser incandescence. There has been major development in instrumentation for measuring properties of these carbonaceous particles (i.e., light-scattering and absorption etc.), but obstacles remain for these techniques. To solve these issues, there needs to be a certified reference material that would allow for comparison of

different measurement techniques. This reference material would have to mimic atmospherically relevant BC with properties specific to that instrument's measurement technique.

In the following sections of this Introduction, I will first review the background of BC and other light absorbing aerosols. Then, I will discuss the theory behind aerosol light absorption. I will provide an overview of the filter-based and other instruments involved in the measurement and characterization of light absorbing particles. Lastly, the direction and scope of the dissertation will be discussed.

1.1 Light Absorbing Aerosols

1.1.1 BC and Terminology

Aerosols BC is a common term used to describe the portion of particulate matter that strongly absorbs across the visible portion of the spectrum. BC is commonly quoted as having a mass specific absorption cross section (MAC) of 7.5 ± 1.2 m^2 g^{-1} at a wavelength of 550 nm[25] and an absorption spectral power law dependence of nearly unity.[17] The MAC value may be reduced if the particles collapse into more compact forms, or it may be enhanced if the particle contains a coating. This enhancement of absorption will be further explored in Chapter 2 of this dissertation. Fresh BC has been reported as to having a single scattering albedo (SSA) within the range of 0.1-0.28.[25-27] SSA is the measurement of light extinction of aerosols due to scattering. Model studies have shown the BC SSA was within a similar range of 0.1-0.2.[28] More details about SSA can be found in Section 1.3 of this Introduction. These highly absorbing particles are considered refractory where they have a very high vaporization temperature of 4000 K. BC typically exists in the

atmosphere as aggregates and is insoluble in water and organic solvents. The small individual spheres are initially formed in the flame and later coagulate to form aggregates. The aggregates consist of spherules with diameters of approximately 20–40 nm.[1, 5, 26] As water and other gaseous materials condense onto the lacey aggregates, they collapse into dense clusters. These particles are produced from the incomplete combustion (when oxygen is insufficient) of carbon-based fuels. Reactions involving polycyclic aromatic hydrocarbons (PAHS) are known to be precursors to BC formation.[29] BC is primarily removed from the atmosphere through wet deposition and has a typical lifetime of a week. Fresh BC is hydrophobic and thus acts as poor CCN and IN. Figure 1.3 from Bond et al. (2013) clearly depicts the role of BC in the climate system and shows its sources and sinks.

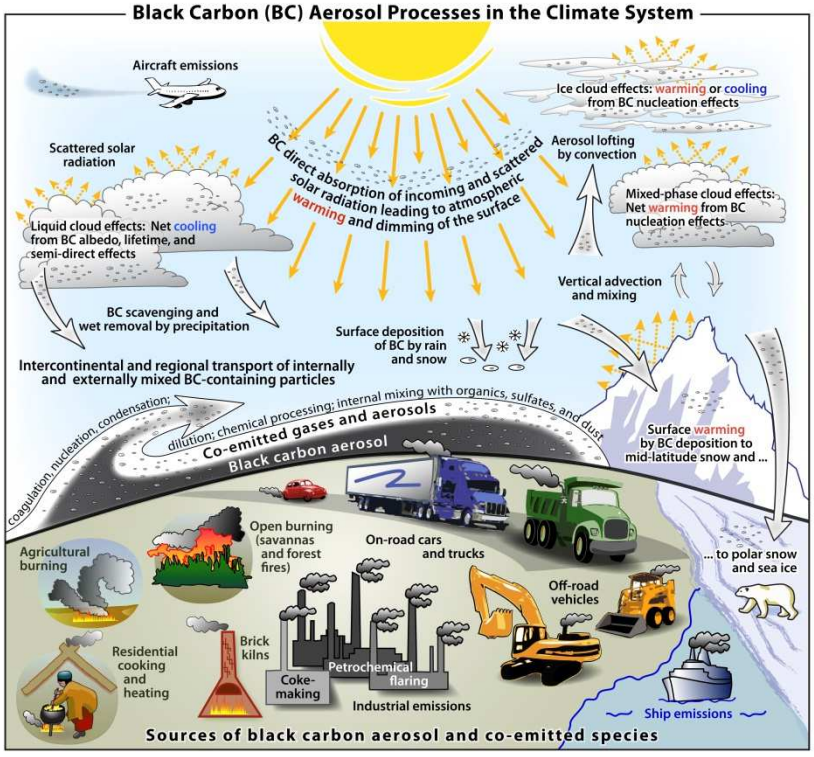

Figure 3.3 *BC's role in the climate system. Also shown are the major sources and sinks of BC. From Bond et al. (2013).*

Of all forms of particulate matter, BC is the most effective in absorbing solar radiation. However, BC has a complex role in climate change because of the direct and indirect effects it has on the climate. Although these light absorbing particles are known to absorb solar light, they can influence cloud formation that can either cool or warm the atmosphere. BC is also known to promote the melting of ice and snow when deposited on it. Researchers estimate the total climate forcing of BC is +1.1 W m^{-2} (with 90% uncertainty bounds of +0.17 to +2.1 W m^{-2}).[5] According to the EPA, the United States contributes approximately 8% of the total black carbon around the globe. Bond et al. (2013) estimated a total global BC emissions value of 7500 Gg yr^{-1}(using bottom up inventory methods).[5] According to the Intergovernmental Panel on Climate Change (IPCC), "Combustion processes are the dominant source for black carbon; recent estimates place the global emissions from biomass burning at 6 to 9 Tg yr^{-1} and from fossil fuel burning at 6 to 8 Tg yr^{-1}." Within the United States alone, major sources of BC are from transport and biomass burning.[30] Models[31] have predicted that black carbon contributes up to 0.3°C-0.4°C in warming, globally. However, there is great uncertainty with this prediction and accurate measurements of BC sources are essential.

The many different terms used to determine the complexity of BC are based on its thermochemical and optical properties. The terms associated with these properties can be alluded to in Figure 1.4.

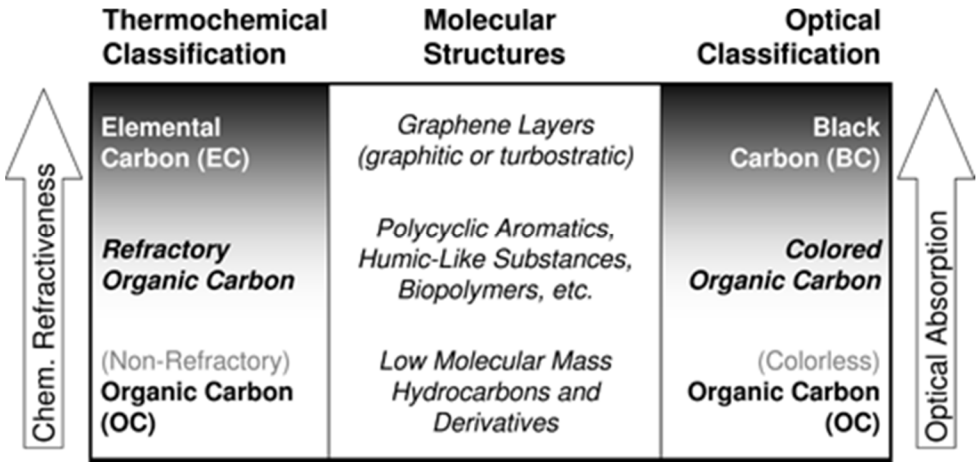

Figure 4.4 *Carbonaceous aerosol classified according to their thermochemical and optical properties.*[9]

Some of these terms include EC, soot, refractory black carbon (rBC) and light absorbing carbon (LAC, which includes BC and BrC).[32-34] Soot is often used interchangeably with BC, however the two definitions are not equivalent. Soot is formed from combustion processes (primarily diesel) and consists mostly of carbon atoms with traces of other elements. Organic vapors from the combustion process usually accumulate on the soot particle once it cools. Soot formation heavily depends on the carbon to oxygen ratio. When the hydrocarbon-air mixture has insufficient oxygen to form CO_2, the products will contain CO and soot. The stoichiometric equation is shown below.[1]

$$C_m H_n + aO_2 \rightarrow 2aCO + 0.5nH_2 + (m - 2a)C_s$$

The carbon to oxygen ratio is m/2a and C_s is the soot formed from the combustion reaction.

Soot is also formed from the incomplete combustion of organic matter, and it is comprised of black carbon and organic carbon. Thus, it is often called "BC-containing" particles. Particles of soot are thought to be insoluble in water and

organic solvents, but this is only true for pure graphite and other allotropes of carbon. Ambient soot behaves differently due to aging and coating. Depending on the source, soot can be composed of purely BC or a mixture of BC, organic carbon (OC), trace metals etc.[9, 31, 35, 36]

EC is often used interchangeably with BC in the literature. However, the term EC represents the operational definition for refractory thermal techniques such as thermal optical analysis (TOA).[37] A greater discussion on TOA can be found in Section 1.3.5 and Chapter 3 of this dissertation. The thermodynamically stable form of elemental carbon is graphite, an allotrope of carbon, composed of sheets of graphene. Graphene has a 6-carbon ring structure that allows for great electron mobility. It is oxidized in air at temperatures over 600°C in air. The structure of graphene is shown in Figure 1.5 below.

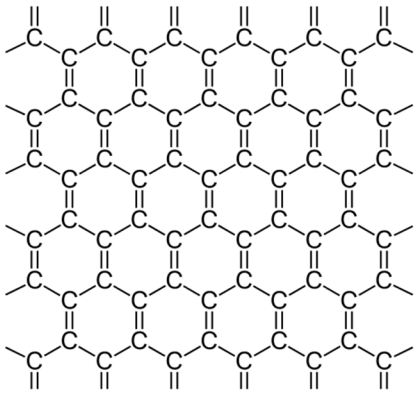

Figure 5.5 *The Structure of Graphene. It has a honeycomb lattice with sp^2 carbons.*[38]

Concentrations of EC found in urban areas are within the range of 1.5 to 20 μg m^{-3}. Over the remote oceans, the EC concentration is within the range of only 5-20 ng m^{-3}.[1] Within the United States, the highest concentrations of EC are found in the Northwest, southern California, and on the east coast.

1.1.2 BrC and Mineral Dust

The BrC is an absorbing organic aerosol (OA) that absorbs from the mid-visible to the near ultraviolet wavelengths. Strongest absorption occurs at the lower wavelengths. This colored organic carbon is comprised of a variable mixture organic compounds that cannot be formally defined. The mass absorption efficiency increases greatly at the lower wavelengths where UV absorption is significant. Instead of looking black, this property makes the particles appear brown due to the spectral dependence. Due to the high absorption at lower wavelengths, the Absorption Ångström Exponent (AAE) of BrC is generally higher than the value of 1 for BC. Hoffer et. al. 2006 determined the AAE of extracted humic-like substances (HULIS) from biomass burning to be within the range of 6-7.[39] The MAC was less than 1 $m^2 g^{-1}$ at 550 nm. Unlike BC, BrC particles are soluble in some organic solvents, and both light absorbers are approximately the same in size. There is still great uncertainty concerning the actual sources for this BrC. Smoldering combustion and residential coal combustion were seen to act as large sources of BrC .[9]

Dust particles are known to be absorbers of light as well. Mineral dust absorbs little in the solar spectrum, with iron oxides being an exception. Asian dust particles are far weaker absorbers per mass then both BC and BrC. Clarke et. al. (2004) reported a MAC value of 0.009 $m^2 g^{-1}$ for Asian dust particles at 550 nm,[40] and Lack et al. (2009) reported a MAC of 0.04 $m^2 g^{-1}$ for long range Saharan dust.[41] Saharan dust has the ability to absorb 1-10% of the radiation it encounters.[41] As with BrC, dust absorption decreases substantially as the wavelength increases.[42] Ferric iron oxides (such as hematite and goethite) resulted in dust absorption when internally

mixed with clay minerals.[43] Dust from the Sahara, Gobi and Niger deserts had MAC values between 0.01-0.02 m^2 g^{-1} at 660 nm and 0.06-0.12 m^2 g^{-1} at 325 nm.[44] Typically dust particles (> 2 μm in diameter), are larger than BC particles, contain crustal/mineral elements (aluminum, silicon, iron and calcium), and are crystalline in structure.[5, 45]

1.2 Background of Light Absorption by aerosols

1.2.1 Basic theory of absorption

Aerosols have the ability to scatter and absorb solar radiation that result in warming or cooling of the Earth. BC is a major absorber and can lead to warming of the planet. The classic Beer Lambert law can be used to represent aerosol absorption:

$$\mathrm{I} = I_0 e^{-\alpha l c} \qquad (1.1)$$

where α is the absorption cross section, *c* is the concentration and *l* is the path length. The absorption coefficient (σ_{abs}, m^{-1}) is the product of α and *c*.[42] The absorption coefficient also commonly described as the absorption by suspended particles within a certain volume. In other words, it describes the loss of light intensity due to absorption per unit volume of particles. The equation below described the absorption coefficient's relationship to number density (*N*, n m^{-3}) and absorption cross section (C_{abs}, m^2).

$$\sigma_{abs} = N * C_{abs} \qquad (1.2)$$

C_{abs} represents the absorption per individual particle. The determination of the scattering coefficient (σ_{sca}) is analogous to equation 1.2 with scattering particles.

The mass absorption cross section (*MAC*, $m^2\ g^{-1}$) value is used to convert σ_{abs} to mass concentration (unit: $g\ m^{-3}$). This value is also defined as the aerosol absorption per unit mass:

$$MAC = \frac{C_{abs}}{m_p} = \frac{\sigma_{abs}}{m_p N} \quad (1.3)$$

where m_p is the particle mass.

The single scattering albedo (ω_0, SSA) is the fraction of light extinction (scattering + absorption) due to scattering:

$$\omega_0 = \frac{\sigma_{sca}}{\sigma_{abs} + \sigma_{sca}} \quad (1.4)$$

SSA is an intensive property determined by particle composition, and it is an important factor when determining whether an aerosol layer has a cooling or warming effect. Non-absorbing particles such as ammonium sulfate have an SSA near unity, while highly absorbing particles have a far lower value.[42]

The AAE is an optical property that defines the wavelength dependence of absorption as follows:

$$AAE = -log(\frac{\sigma_{abs,\lambda 1}}{\sigma_{abs,\lambda 2}})/\log(\frac{\lambda 1}{\lambda 2}), \quad (1.5)$$

where λ is wavelength (pairwise). The AAE of BC is generally near unity, while the AAEs of BrC and dust are higher.

1.3 BC instrumentation

1.3.1 Need for a reference material

Scientists have developed several pieces of instrumentation to quantify the source emissions, absorbance, and mass concentration of BC. However, there is currently no established reference material for calibrating and validating the instruments used to characterize BC. The properties of BC (or commonly referred to as soot) are highly complex and can differ greatly upon several environmental factors. The lack of BC reference materials creates a challenge when comparing different instruments and methods.[33]

1.3.2 Aethalometer

BC is often measured by commercial, filter-based instruments. One of these is Magee Scientific's Aethalometer.[15] The name Aethalometer is derived from the Greek word 'aethaloun', which means to blacken with soot. The Aethalometer (Model AE31) measures light absorbing aerosols at multiple wavelengths in real time. This robust instrument is user friendly and widely used because it provides unattended and automatic operation. However, this measurement technique suffers from several systematic errors as addressed in Chapter 2 of this dissertation. The range of wavelengths stretches from the ultra-violet (UV) to the near-infrared (IR) region of the electromagnetic spectrum, specifically: 370, 470, 520, 590, 660, 880 and 950 nm.

Air is sampled using a small internal pump and the air stream passes through a filter tape. The filter tape is composed of a quartz layer and a cellulose layer. As the stream passes through the filter, suspended particles are deposited onto the surface.

The filter tape does not move until the filter tape reaches a maximum attenuation (ATN). ATN is the reduction of light intensity as the light passes through the filter. The attenuation of the sample collected on the filter is calculated by the following equation:

$$ATN = 100 * \ln(\frac{I_0}{I}) \qquad (1.6)$$

I_0 is equal to the intensity of light through the original filter and I is the portion of filter where the aerosol is deposited. The light detectors of the Aethalometer serve to measure transmission of light through an aerosol laden filter and a pristine portion of the filter. Figure 1.6 below depicts how the Aethalometer works.

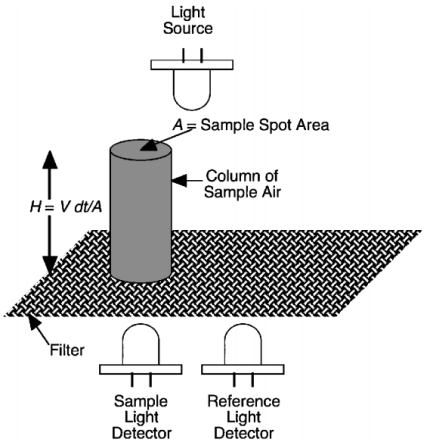

Figure 6.6 *Aerosol laden air is deposited on the filter with a certain spot area. The light detectors are meant to measure the transmission of light through the filter.*[46]

The time-based of the Aethalometer is the time at which measurements take place during that specific period. Data are output once every time-based period, usually set to 1-5 minutes. There are some tradeoffs; a shorter time-based should be used in areas of higher BC concentration (urban) while a longer time-based should be used for measurements in rural or remote areas.

Instead of measuring the actual absorption coefficient for ambient aerosols, the Aethalometer measures the attenuation coefficient (σ_{ATN}) because it monitors the attenuation of light through a filter. The equation below shows the calculation of the attenuation coefficient.

$$\sigma_{ATN}(atn.coefficient) = \frac{\Delta ATN}{\Delta t}\left(\frac{A}{V}\right) \qquad (1.7)$$

A is the surface area where the particles are being collected on the filter, V is the volumetric flow rate and Δt is the timebase. The attenuation coefficient is given in units of m^{-1}.

The Aethalometer determines the mass of black carbon by using a single value for the MAC. The manufacturer refers to this MAC value as SG or the "specific attenuation cross-section for the particle black carbon deposit on this filter, using the optical components of this instrument."[46] Magee Scientific provides values to compute the SG by using the following equation.

$$SG\ \left(\frac{m^2}{g}\right) = 14625/\lambda \qquad (1.8)$$

At 880nm, the SG value for AE31 is 16.6 $m^2\ g^{-1}$. This SG is used to convert attenuation coefficient into the mass concentration.

Filter-based instruments must be corrected for errors such as multiple light scattering within the filter. The filter matrix will increase the path length of the incident light due to scattering events taking place by the filter medium. Another correction needed is for the filter loading. As particles accumulate on the filter, the path length for light to travel is decreased. At low ATN values, the relationship between attenuation and BC surface loading is linear However, as the attenuation values rise, this relationship becomes nonlinear due to the shadowing effect, and the

BC mass concentration is underestimated.[16] The correction for this nonlinear artefact depends on the amount of absorbing particles and other optical properties. Lastly, the amount of scattering from the particles will influence the attenuation. When scattering particles such as ammonium sulfate are deposited on the filter, the light is scattered in multiple directions. When scattered in multiple directions, more particles already collected on the filter have the opportunity to absorb this light.[32]

There have been many Aethalometer algorithms developed to correct the absorption coefficient values. However, all the correction algorithms generate different results. Weingartner et al. (2003) developed a correction that takes into account the attenuation effect for filter loading and a calibration constant for different aerosol types.[21] Arnott et al. (2005) developed a correction that corrects for scattering aerosol[46] and Schmid et al. (2006) developed a scattering correction utilizing the single scattering albedo.[19, 47]

In this dissertation I also characterized the newer, 7-wavelength AE33 model of the Aethalometer (See Chapter 4). This version of the Aethalometer follows the same measurement principle of older models from Magee Scientific. The ATN is measured on two sample spots of different sample flows, and a reference spot.[48] The results of both spots are combined mathematically to remove any nonlinearities As with older models, BC is measured at λ = 880 nm. However, the SG value (referred to as mass absorption cross-section in the manual) is reduced from the previous value of 16.6 to 7.77 $m^2\ g^{-1}$. The filter tape automatically advances when the ATN reaches a certain threshold so that readings can take place on a pristine spot.

A series of equations are used to convert ATN into BC mass concentration and to correct for the non-linearity caused by the filter-loading effect. Firstly, the lateral airflow is accounted for by the following equation:

$$F_{in} = F_{out} \cdot (1 - \zeta), \quad (1.9)$$

where F_{in} is the input flow and F_{out} is the output flow (or measured flow). The ζ is equivalent to the leakage factor, where values range from 0.02 to 0.07. The attenuation coefficient measured by the AE33 (σ_{ATN_A33}) is determined by:

$$\sigma_{ATN\_AE33} = \frac{S*(\Delta ATN/100)}{F_{in}\Delta t}, \quad (1.10)$$

where S is the spot area, and t is the time. The absorption coefficient is then calculated as the following:

$$\sigma_{ABS\_AE33} = \frac{\sigma_{ATN\_AE33}}{C}, \quad (1.11)$$

where C is the multiple scattering parameter and it strongly depends on the filter material.[16, 21] The BC mass concentration (BC_{mass}) is equivalent to:

$$BC_{mass} = \frac{\sigma_{ABS\_AE33}}{SG}, \quad (1.12)$$

and the compensated BC mass concentration (BC_{mass_comp}) is determined by the following equation:

$$BC_{mass\_comp} = \frac{BC_{mass}}{(1 - k * ATN)} \quad (1.13)$$

with k being the compensation parameter. The final equation is:

$$BC_{mass\_comp} = \frac{S*(\Delta ATN_1/100)}{F1\,(1-\zeta)*SG*C*(1-k*ATN_1)*\Delta t}. \quad (1.14)$$

The dual spot algorithm used in the AE33 successfully compensates for the loading effect and does not require the knowledge of the origin of the aerosol collected on the

filter. The BC mass concentrations determined by the AE33 compared well to the compensated BC mass concentrations from legacy Aethalometers in various studies.[16] [48]

1.3.3 Particle Soot Absorption Photometer

The Particle Soot Absorption Photometer (PSAP), manufactured by Radiance Research (Seattle, WA), is used to measure the light absorption coefficient (σ_{abs}) of aerosols in real time. This filter-based instrument collects aerosol particles on a glass/cellulose filter and measures the decrease in transmittance over time. The PSAP operates at λ=565 nm, and the change in the intensity of the transmitted light correlates to the absorption coefficient. It consists of two spots, where the first spot is for particle collection and the second spot serves as a reference to monitor the changes in the LED light source. The primary spot collects particles from the air stream, while a clean airstream passes through the second reference spot. Figure 1.7 below depicts the operating principle of the PSAP.

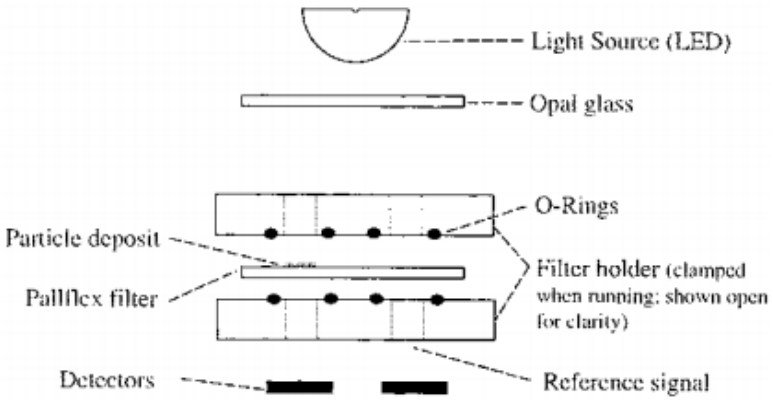

Figure 7.7 *Schematic diagram of the PSAP.*[49]

The relationship between the absorption coefficient and change in the light intensity is given by the equation below.

$$\sigma_{abs} = \frac{A}{V\Delta t}\left(ln\frac{I_0}{I}\right) \qquad (1.15)$$

A is the collection area of the filter, V is the volumetric flow rate of the air sample, Δt is the time-based, I is the transmitted intensity after the time period, while I_0 is the transmitted intensity from the previous time period. Because this measurement of absorption involves a filter medium (like the Aethalometer), there needs to be solutions to correct for the multiple artefacts associated with this instrument.

1.3.4 Single Particle Soot Photometer

The Single Particle Soot Photometer (SP2, Droplet Measurement Technologies, Inc., Boulder, CO) is used for quantitative measurements of rBC mass in real time using laser incandescence. The SP2 indirectly quantifies the refractory BC by measuring the peak intensity by thermal emission. [50] Particles flow into a chamber through a cavity with particle free sheath air and they pass through a Gaussian shaped laser beam operating at 1060 nm. Particle size is determined by the scattered light as particles pass through the laser's pathway. The radiation of the beam heats up the absorbing particle to incandescence at approximately 4000 K.[51] Due to the high temperatures from the beam, quantitative measurements of scattering aerosols are not possible. The SP2 is able to provide information about the mixing state of rBC containing particles with non-refractory materials. Accuracy is <10% and uncertainty is ~25%.[52]

Four optical detectors are focused on a precise position in which the aerosol sample interacts with the laser beam.[53, 54] Two of the detectors detect visible light within different wavelength bands (350-800 and 630-800 nm).[53] The other detectors

are used for quantifying the scattering component and to determine the position of the particle in the laser beam. Calibrations of this instrument are generally conducted with atomizing aqueous solutions of size selected fullerene soot, Aquadag[55] or glassy carbon.[33] Figure 1.8 presents a schematic diagram of the SP2 instrument.

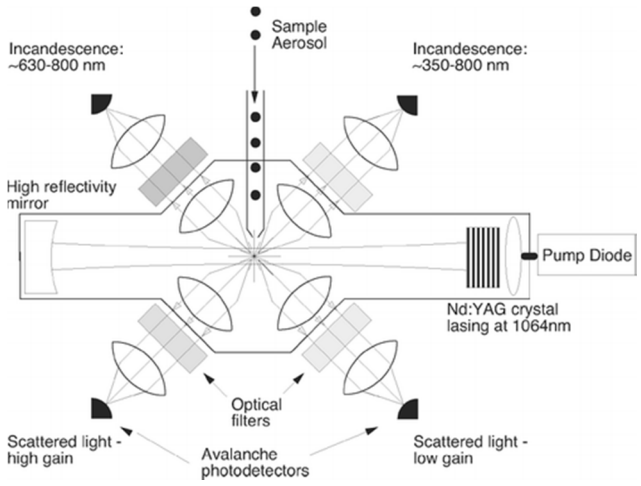

Figure 8.8 *Schematic of the SP2 instrument. Shown are the optics, incandescence and scattering detectors of the instrument.*[54]

1.3.5 Thermal Optical Analysis

TOA is a thermal optical technique used to determine the amount of EC and OC collected on a refractory quartz filter that can withstand the high temperatures used in the protocols. Problems arise when classifying the carbon as either organic or elemental, and different temperature programs generate different ratios.

In an oxygen-free environment, the sample is heated in four temperature steps with He used as the inert carrier gas. Examples of temperature steps using different protocols that are meant to remove all organic carbon are provided in Chapter 3 of

this dissertation. The transmission of the laser through the sample matrix is meant to monitor OC converted pyrolytically to elemental carbon. During this step, the organic compounds are oxidized to CO_2 in an oxidizing oven. With the flow of He, the sample then passes through the methanator oven. The methanator oven is a bed of Raney nickel particles heated to 500ºC. While passing through the methanator, the CO_2 reduces to methane. The methane produced is then measured by flame ionization detection (FID).

To determine the amount of EC, the carrier gas is switched to a 2% oxygen and helium mixture. During the temperature steps, the original elemental carbon and the organic carbon pyrolytically converted to elemental carbon are then oxidized to CO_2 due to the presence of the oxygen in the carrier gas. The CO_2 is then reduced to methane by passing through the methanator oven and detected by FID. EC is quantitatively determined when the laser signal returns to the initial level prior to OC pyrolysis. Lastly, methane is injected into the sampling oven so that the FID can be calibrated. A schematic diagram of the Thermal Optical Analysis technique is shown in Figure 1.9. More information about this technique can be found in Chapter 3 of this dissertation.

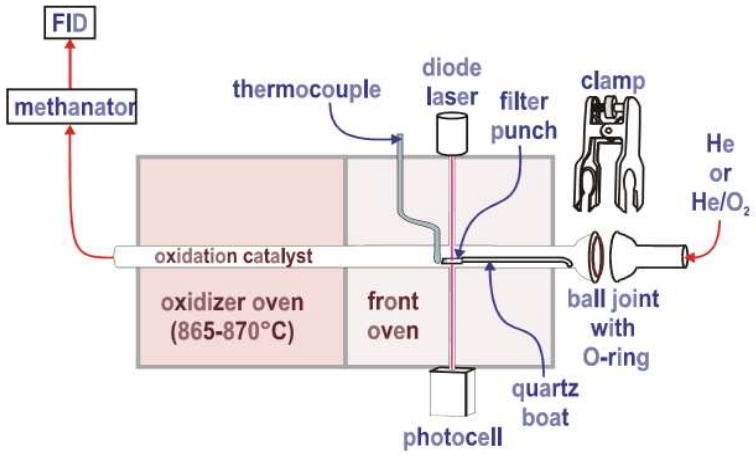

Figure 9.9 *Schematic Diagram of the Sunset Thermal Optical Carbon Analyzer. Filter samples can be either 1.0 cm^2 or 1.5 cm^2.*[56]

1.4 Instrumentation used for characterization

1.4.1 Differential Mobility Analyzer

The Differential Mobility Analyzer (DMA) size selects particles based on electrical mobility. It is one of the most widely used instruments for generating monodisperse aerosols. Particle size is determined from the mobility distribution. When in a gas medium, the charged particle experiences a force dependent on the electric field and the charge of the particle. The acceleration of the particle goes against the viscous forces within the fluid. The terminal velocity of the particle is reached when the viscous forces and the electrical forces are balanced. The electrical mobility of a particle is dependent on Stokes' law shown in the following equation.[57]

$$Z = \frac{qeC(D_m)x}{3\pi\mu D_m} \qquad (1.16)$$

Z is equal to the electrical mobility, q is the number of elementary charges on the particle, and e is the elementary charge of an electron with a value of 1.60 x 10^{-19}

C. Viscosity is shown as μ and D_m is equivalent to the mobility diameter. In this equation, x, is the dynamic shape factor, equal to unity for spheres, but it depends on aerodynamic drag due to difference in shape. It is essentially a ratio of the drag force of the particle to the drag force of a spherical particle having the equivalent volume. $C(D_m)$ is the Cunningham slip correction factor (of a specific mobility diameter), and this takes into account the impact of the drag force on smaller particles. Particles may settle more rapidly than previously noted with Stokes' Law. The equation for the Cunningham slip correction factor is shown below in equation 1.17.

$$C = 1 + \frac{2\lambda}{d} * (A_1 + A_2 * e^{\frac{-A_3 * d}{\lambda}}) \qquad (1.17)$$

The mean free path is shown as λ, d is the particle diameter, A_1 is equal to 1.257, A_2 is 0.400 and A_3 is equal to 0.55. These coefficients were experimentally derived. This slip correction factor is meant to modify Stokes' law for particle diameters that are on the order of the gas free mean path and smaller.

The DMA consists of a cylinder with a charged central rod. Figure 1.10 below depicts the mechanism of the DMA.

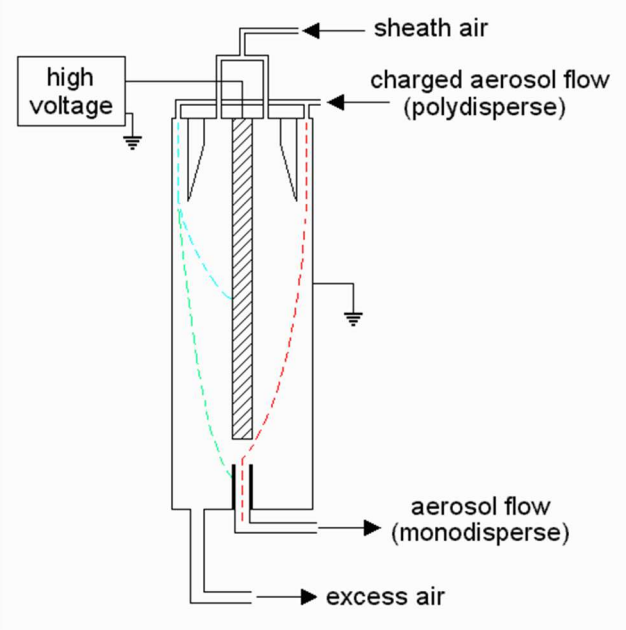

Figure 10.10 *The Differential Mobility Analyzer. This instrument size selects based on electrical mobility. (www.cac.yorku.ca)*

The space between the charged rod and the cylinder has an electric field in which the particle flows through. Particle-free sheath air is the main flow through the DMA. Particles are injected into the DMA where they move to the charged rod at a velocity corresponding to their electrical mobility. Particles of a given mobility will exit through a slit at the far end of the central rod, while the rest will exit through the exhaust. Because the DMA separates based on electrical mobility, there are some larger particles that have higher order charges and the same mobility diameter. However, these particles will not be separated out. To remove this uncertainty, a charge neutralizer, a second DMA or an aerosol particle mass analyzer (APM) could be used.[57]

1.4.2 Aerosol Particle Mass Analyzer

The aerosol particle mass analyzer (APM) is used to classify particles according to their mass-to-charge ratio by balancing electrostatic with centrifugal radial forces. The instrument contains two cylindrical electrodes that rotate around a common axis. There is an annular gap region where the charged particles enter and the inner electrode has a certain voltage. The outer electrode, on the other hand, is grounded and both electrodes rotate at an angular velocity. The particles of the chosen mass experience balanced centrifugal and electrostatic forces when passing through the APM. Unlike the DMA, the APM is not dependent on the orientation, size and shape factor of the particle. The particles passing through the APM satisfy the following equation:

$$m_p r\omega^2 = \frac{qeV}{rln(\frac{r_1}{r_2})}. \qquad (1.18)$$

The angular velocity is represented by ω, V is the voltage of the inner electrode and m_p is the particle mass. The variables q and e are the number of unit charges, and the elementary unit of charge (1.61×10^{-19} C), respectively. The terms r_1 and r_2 are the radii of the inner and outer electrode (respectively) where mass selection is taking place.

1.4.3 Condensation Particle Counter

The condensation particle counter (CPC) is used to determine the number concentration of ultra-fine particles within a sample. Condensation particle counters detect particles by laser scattering. First, the particles are grown by condensation so that they are easily detected. The aerosol sample passes through a heated saturator

where butanol enters the aerosol sample stream. Next, the aerosol and butanol stream pass through a cooled condenser, and the butanol vapor condenses. The particles from the aerosol stream behave as condensation nuclei where they eventually grow into large droplets in a supersaturated vapor. This is referred to heterogeneous nucleation. Supersaturation is the actual vapor mixing ratio divided by the saturation vapor mixing ratio at that specific temperature. The size of the particle will affect the rate of supersaturation. The Kelvin diameter is the smallest size of the particle at which condensation will occur. Then the droplets are counted as they pass through an optical detector with a laser beam. At high concentrations, the CPC will count the amount of light scattered from the particle converted droplets. Thus, particle count is directly related to scattered light. Figure 1.11 shows a schematic diagram of the condensation particle counter.

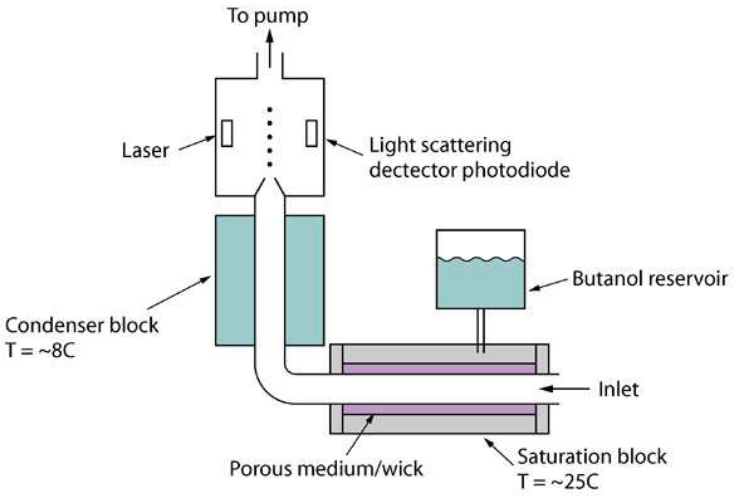

Figure 11.11 *Schematic diagram of the Condensation Particle Counter (Condensation Particle Counters. Centre For Atmospheric Science). The CPC determines total number concentration.*

1.4.4 Scanning Electron Microscopy

A Scanning Electron Microscope (SEM) is a powerful magnification tool used to characterize different materials. It uses a focused beam of high-energy electrons to interact with the atoms of a solid sample to produce signals that provide information about the composition and topography of the surface. The technique provides superior resolution compared to an optical microscope due to electrons having a smaller wavelength than visible light.

A general layout of the SEM is shown in Figure 1.12. The electron beam is generated by an electron source and the entire column is held under vacuum. Electromagnetic lenses are used to control the path of the beam. These lenses consist of wires within a metal pole and generate a magnetic field as current passes through. The lenses can be categorized into two types (*e.g.* condenser lens and objective lens). The condenser lens is meant to determine the size of the electron beam and the objective lens focuses the beam onto the sample being analyzed. Scanning coils are lenses that move or raster the beam.

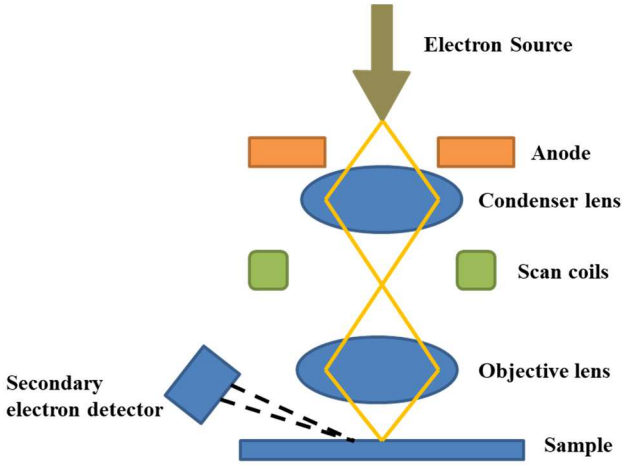

Figure 12.12 *Schematic diagram of the components of the SEM instrument.*

Two forms of electrons are generated when the high energy electrons come into contact with the sample's surface. These include backscattered electrons (BSE) and secondary electrons (SE). Backscattered electrons are a beam of electrons that are reflected backwards when hit with an electron beam after penetrating the sample close to the surface. They result from the elastic scattering events from the interactions of the beam with the sample. BSE are very sensitive to atomic number. Elastic scattering is a process where energy is not loss from the incident primary electrons. SE are generated from the inelastic interaction between the beam and the surface of the sample. SE have lower energies than BSE, and as SE reach a depth within the sample, they lose a lot of energy from the inelastic process. SE emission reveals fine surface features that give SEM its high lateral spatial resolution. Figure 1.12 also displays secondary electron detection.

Energy-dispersive X-ray Spectroscopy (EDX) is a non-destructive analytical technique that provides information on elemental composition of different samples. When coupled with SEM, the electron beam produces x-rays. With EDX, the electron beam ejects an electron from the inner shell. The energy difference is released in the form of an X-ray and different elements have unique X-ray emissions. EDX is commonly used for elemental mapping and can give quantitative information about the sample's elemental makeup.

1.4.5 Aerosol Aerodynamic Classifier

The Aerodynamic Aerosol Classifier (AAC, Cambustion) is a commercial instrument used to produce a monodisperse aerosol of a specific aerodynamic diameter.[58] The aerodynamic diameter is the equivalent diameter of a spherical particle with a density

of 1000 kg m^{-3} that has the same terminal settling velocity as the actual particle.[59] Unlike the DMA, APM and Centrifugal Particle Mass Analyzer (CPMA), particle charging is not required for particle classification. However, when combined in tandem with the DMA and CPMA, more particle properties (such as mobility diameter, particle mass, effective density, mass-mobility exponent, and dynamic shape factor) can be found. The AAC classifies the aerodynamic diameter of particles according to their relaxation time, τ, on the basis of the following equation:

$$\tau = \frac{C_c(d_{ae})\rho_0 d_{ae}^2}{18\mu}, \qquad (1.19)$$

where C_c is the Cunningham slip correction factor, d_{ae} is the aerodynamic diameter, μ is the viscosity of the gas and ρ_0 is the standard density.[59]

This instrument consists of two concentric cylinders rotating in the same direction at the same speed. The particles are carried through the instrument by the aerosol flow, Q_a, and enter the spacing between the two cylinders through a slit in the wall of the inner cylinder. The particle-free sheath air, Q_{sh}, flows within the spacing of the two cylinders. As the cylinders rotate the particles experience centrifugal and drag forces. Particles of a narrow relaxation time exit the classifier, while those with larger relaxation times impact the outer cylinder. Particles experiencing a shorter relaxation time exit with the exhaust. A schematic diagram of the AAC is provided in Figure 1.13

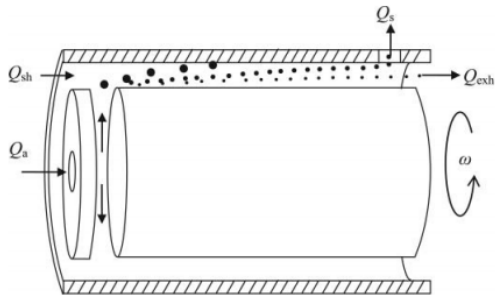

Figure 13.13 *Schematic diagram of the components of the AAC instrument. Q_a is the aerosol flow, Q_{sh} is the sheath flow rate, Q_{exh} is the exhaust flow rate, Q_s is the sample flow rate and ω is the rotational speed.*[59]

1.5 Scope of this Dissertation

This dissertation will focus on the measurement and characterization of light absorbing particulate matter and on using ambient measurements to evaluate emission inventories of BC for the New York City (NYC) area. All forms of instrumentation used in this dissertation are provided in Table 1.1. Firstly, the Aethalometer was evaluated using a well-characterized, size-selected BC surrogate. The work presented in this chapter was published in Zangmeister et al. 2019, and is currently in press in the journal of *Aerosol Science and Technology*. The output of BC mass concentration from the Aethalometer (Model AE31) was compared to *in situ* BC mass concentrations under controlled, laboratory conditions. To mimic ambient particles, I also created a BrC surrogate and coated BC particles, and evaluated the response of the Aethalometer to these internal mixtures (Chapter 2). A similar study was performed with BC in ammonium sulfate. Using the same BC surrogate and sucrose, I evaluated a different instrument used for BC (often used interchangeably with EC) and OC measurements: Thermal Optical Analysis. This work can be found in Chapter

3 of this dissertation and is published in the journal of *Atmospheric Environment*. Lastly, the same BC surrogate from Chapters 2 and 3 was used to develop a calibration procedure for the updated model of the Aethalometer: AE33. Results can be found in the first half of Chapter 4.

In the last phase, involving part of Chapters 4, 5, and 6, I evaluate ambient, absorbing particulate matter in the US and across the globe in China. In Chapter 5 I used refractory BC (rBC, and commonly referred to as just BC in the literature) mass concentrations from the SP2, and absorption coefficients from the PSAP to evaluate the MAC of ambient light absorbing aerosols. Back trajectory analysis was also used to aid in source analysis. Lastly, the particles from China were characterized at a microscopic level with SEM-EDX. With the help from Bob Willis from the Environmental Protection Agency (EPA, Raleigh, North Carolina), we were able to identify possible sources through hierarchical cluster analysis, and TOA. Finally, Chapter 7 will discuss the overall conclusions from this research and the future work ahead.

Once the AE33 was calibrated with the BC surrogate described in Chapter 4, that same instrument model was deployed on an aircraft and at roadside monitor in NYC. During the summers of 2018 and 2019, AE33 instruments were used to measure BC mass concentration within this metropolitan area both from the Cessna and on the ground. Using concurrent measurements of carbon monoxide (CO), I was able to determine the $\Delta BC/\Delta CO$ ratios for the weekday and weekend, and show how the differences related to highway traffic. With the ambient $\Delta BC/\Delta CO$ concentrations and ratios, I identified which of three published inventories is most consistent with

ambient measurements and used a combination of CO emissions and the ΔBC/ΔCO ratio to quantify total BC emissions for the NYC metropolitan area.

Table 1.1 *Instrumentation used in this dissertation and brief description.*

Instrument name	**Brief description**
Aethalometer	Filter-based instrument (Magee Scientific) that measures the mass concentration of BC.
Particle Soot Absorption Photometer	PSAP (Radiance Research); filter-based instrument that measures absorption coefficient.
Single Particle Soot Photometer	SP2 (Droplet Measurement Technologies); direct measurement of black carbon in individual aerosol particles using laser incandescence.
Scanning Electron Microscopy Energy-dispersive X-ray Spectroscopy	SEM-EDX; form of electron microscopy that provides elemental composition of samples
Differential Mobility Analyzer	DMA; size selects particles based on electrical mobility
Aerosol Particle Mass Analyzer	APM; classify particles according to their mass-to-charge ratio to define particle mass, m_p.
Condensation Particle Counter	CPC; counts the number of particles per unit volume (number concentration, N_p)
Aerodynamic Aerosol Classifier	AAC (Cambustion); classifies particles according to their aerodynamic diameter using relaxation time.
Thermal Optical Analysis	TOA; thermal optical technique used to determine the amount of EC and OC.

Chapter 2: Evaluation of a filter-based black carbon (BC) instrument using a brown carbon (BrC) surrogate as well as pure and coated BC surrogates

Grimes, Courtney D., and Russell R. Dickerson. "Evaluation of a filter-based black carbon (BC) instrument using a brown carbon (BrC) surrogate as well as pure and coated BC surrogates." *Aerosol Science and Technology* (2021): 1-18.

2.1 Introduction

There currently exists substantial uncertainty in trends of the concentration of black carbon (BC) due to imprecise knowledge of sources, sinks, and of measurement accuracy.[60] Radiative forcing due to BC is similar in magnitude to methane, although BC is known to have a shorter lifetime. The EPA characterizes BC as a component of particulate matter with an aerodynamic diameter under 2.5 μm (PM2.5) where the standard regulatory compliance annual average concentration is currently 12 μg m^{-3}. BC is also known to have a significant effect on cloud formation, the cryosphere through reduced snow and ice albedo, and an adverse effect on human health [61,62]. BC is comprised primarily of elemental, graphene-like carbon making it an effective material at absorbing solar radiation across the UV, visible, and near-IR. Prior assessments have estimated that atmospheric BC has a mass specific absorption cross section (MAC) of 7.5 ± 1.2 m^2 g^{-1} at λ=550 nm and a power law dependence near unity when particles are in the Rayleigh regime [5, 9, 25, 63]. The power law dependence or absorption Ångström exponent (AAE) of aerosols provides important input for calculations of atmospheric heating as a function of wavelength. Sun photometers [64, 65] and photoacoustic methods have been used to study the optical properties of biomass burning smoke containing brown carbon (BrC)[39]. Some models assume BrC

has optical properties of organic aerosol (OA) with only scattering [66]; this could produce a bias in the direct radiative effects of smoke. The wavelength dependent attenuation as measured by filter-based instruments has been used to approximate *AAE* [34, 67-69], but the optical properties of particles on a filter differ from those of particles suspended in air. We distinguish *AAE* (referred to here as A_bAE) from attenuation Ångström exponents (A_tAE) measured by the Aethalometer. As has been pointed out in Lewis et al. (2008),[70] A_tAE should not be used as *AAE* in radiative heating schemes, but it provides useful information on the optical properties and composition of aerosols. The A_bAE is fit using a single power law expression

$$\frac{MAC_\lambda}{MAC_{\lambda_0}} = \left(\frac{\lambda}{\lambda_0}\right)^{-A_bAE} \quad (2.1)$$

Where λ_0 represents the reference wavelength of 550 nm. The A_bAE of the mass absorption cross section (*MAC*) for size-and mass-selected with mobility diameter (D_m) of 300 nm BC surrogate has been measured using photoacoustic spectroscopy (PAS) spanning wavelengths of 405 nm $\leq \lambda \leq$ 780 nm. This *MAC* is size dependent; for D_m of 300 nm, Zangmeister et al. (2019) determined an A_bAE of 0.76 [71] and a refractive index (RI) at 550 nm of 1.77 (± 0.02) + 0.08(± 0.01)i [72] within the range of values for BC proposed by Bond and others[49]. The A_bAE, also varies with particle size, measuring as high as 1.25 for D_m of 150 nm and as low as 0.428 for D_m of 500 nm [71].

Among the methods used to quantify BC mass concentration and particle absorption are continuous, laser-induced incandescence (SP2) of individual BC particles, and PAS. Other, simpler and less expensive techniques such as the

Aethalometer (Magee Scientific, Model AE 31) and the Particle Soot Absorption Photometer (PSAP) measure light transmittance through a filter to quantify light absorbing aerosols [9, 15, 25, 33, 63, 73]. Many of these filter-based instruments generate BC data (mass concentration or absorption coefficient) over a range of wavelengths that stretch from the ultra-violet (λ=370 nm) to the near-infrared (λ=950 nm) to provide information about the spectral contribution of absorbing aerosol, and distinguish BC from brown carbon (BrC). The attenuation (*ATN*) of the sample collected on the filter is defined by

$$ATN = 100 * \ln(\frac{I_0}{I}) \quad (2.2)$$

where I_0 is the intensity of light transmitted through a clean portion of the filter and I is the intensity of light transmitted through the particle-laden portion of the filter. The conversion of attenuation values recorded by the Aethalometer to attenuation coefficients is given by the following equation:

$$b_{ATN}(m^{-1}) = \frac{A}{Q}\frac{\Delta ATN}{\Delta t} \quad (2.3)$$

The terms b_{ATN}, A, Q and Δt are the attenuation coefficient (m^{-1}), the spot area, volumetric flow rate, and the time interval, respectively [21].

The filter-based Aethalometer uses wavelength-dependent, specific attenuation cross sections (constants called *SG* in units of $m^2\ g^{-1}$) to determine BC equivalent mass concentration, *eBC*, in units of $g\ m^{-3}$. From b_{ATN}, mass concentrations are calculated as follows:

$$eBC(g\ m^{-3}) = \frac{b_{ATN}}{SG} \quad (2.4)$$

BC mass concentration is usually reported at λ=880 nm because of reduced effects of absorption from brown carbon, mineral dust, or other UV-active material [21, 46, 73-75].

Many assumptions and instrumental artefacts must be accounted for in the measurements of BC mass concentrations with commercially available, filter-based instruments [74]. It is assumed, for the Aethalometer, that attenuation increases due only to light absorption as BC accumulates on the filter.[75] However, BC aerosol absorption efficiency varies with composition, size, structure, and source. Loading (or shadowing) effects have been observed when measuring *eBC* for soot [76, 77], and Arnott et al. [46] observed this phenomenon where the Aethalometer under predicted *eBC* on a heavily aerosol laden filter. Use of the Aethalometer assumes the optical properties of the particles behave in the Rayleigh limit and that all light absorption is attributable to BC, as indicated by an A_bAE of unity. There are multiple correction schemes published [21, 46, 20, 47] where each is appropriate for different conditions. Weingartner et al. (2003) proposed calibration constants for different types of aerosols including spark-generated soot, diesel soot, and coated soot to correct for the multiple scattering effects due to the filter matrix itself [21]. Corrections have also been developed that include a scattering component derived from multiple scattering theory for highly absorbing materials under laboratory and ambient conditions. Arnott et al. 2005 derived a scattering correction for when the filter-based instrument did not measure zero for a purely scattering material. They concluded that scattering measured concurrently improves accuracy. Other schemes only apply a filter-loading correction. At high BC mass loadings, a shadowing effect occurs as the absorbing aerosol accumulates on the filter, and requires a correction [76, 77]. Newer models of this

instrument use a second sample spot to compensate for this effect, but are not evaluated here.

While in the atmosphere, BC is constantly modified (mixing, reactions, and coating) during the aging process. An example of one of these coatings may be BrC, as from biomass burning. An outer coating (or shell) on a BC particle will alter its optical properties and create additional uncertainties in measurement. The core-shell model of coated BC has shown that coatings enhance absorption (in comparison to uncoated particles) due to what is commonly called the lensing effect, more accurately referred to absorption enhancement, as has been demonstrated through theoretical calculations, laboratory experiments, and field measurements [35, 78, 79].

Evaluation of filter-based instruments requires use of a well characterized material to minimize measurement uncertainty and variability. This study uses a BC surrogate (Cab-O-Jet 200, Cabot Corp.), for evaluation of Aethalometers' *eBC* measurements when compared to CPC's *in-situ* measurements. New specific attenuation cross section values were developed for this material as a way to correct for BC_{eq} at multiple wavelengths. This surrogate has a known elemental carbon composition, size dependent *MAC* values, refractive index, and A_bAE, as determined in previous work [71, 72]. The optical properties of this substance, both pure and in mixtures, were evaluated by You et al. (2016) with PAS. Here, we evaluate pure BC and BrC surrogates along with BC coated with AS and BrC with a filter-based technique.

2.2 Materials and Methods

For all experiments, BC aerosols were generated from aqueous colloid suspensions of

Cab-O-Jet 200 (Cabot Corp., 20.03 wt. % solids) with a liquid jet cross-flow atomizer; the particles were dried by passing through a pair of diffusion dryers. BC aerosol concentrations were varied by adding deionized water.

The aerosol flow was sent to a differential mobility analyzer (DMA) with a sheath:aerosol flow ratio of 10:1 to produce a steady air flow containing particles of known mobility. The particle mass was determined by doing a mass scan with an aerosol particle mass analyzer (APM) for size selected particles. For Aethalometer (AE 31, Magee Scientific, Berkeley, CA) testing, the flow of size-selected aerosols was passed to the 7-wavelength Aethalometer and to a condensation particle counter (CPC) operated in parallel as depicted in Figure 2.1 below.

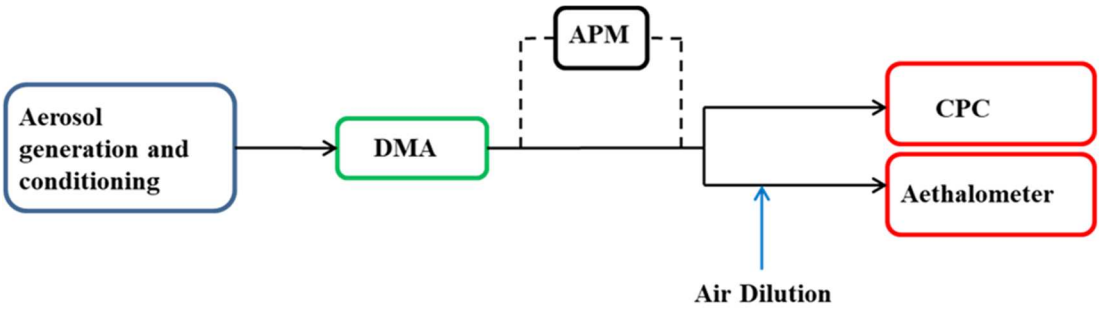

Figure 2.1 *Schematic diagram of the experimental setup for comparisons between the Aethalometer and the CPC. Aerosols were generated through liquid atomization before entering the DMA to select the mobility diameter (in this case 300 nm). Mass distributions were measured to determine particle mass with a removable APM in line. The CPC measured aerosol* N_p*, while the filter-based instrument or Aethalometer measured BC mass concentration.*

2.2.1 Aerosol Generation

As mentioned in You et al. 2016, Cab-O-Jet consists of monomers that upon drying they have a morphology similar to collapsed BC. Brown Carbon was generated from Ful-Humix (Faust BioAg Inc., 50 wt% humic acids) by the extraction procedure found in You et al. (2016).

Different mass fractions of BC in nearly transparent (ammonium sulfate, AS) and weakly absorbing (BrC) components were created to mimic the BC mass fractions found in for example in India [80] from burning of biomass fuels. We prepared a 5 mg ml^{-1} solution of BC and AS with BC mass fractions of 0.07, 0.14, and 0.205. These internal mixtures of BC with AS were co-atomized. A 5 mg ml^{-1} solution of 0.14 by mass BC mixed with the BrC surrogate, humic acid (HA), was also prepared and co-atomized.

2.2.2 Thermal Optical Analysis and SEM

The BC surrogate's elemental carbon to total carbon ratio, EC/TC, was determined using thermal optical absorbance (TOA) (following a modified NIOSH method) in Zangmeister et al. (2019) and Grimes et al. (2020). It was found to be 96 (+/- 2) % BC, with the remaining ~4% organic carbon and sulfur compounds.

SEM images have shown that the particles are composed of nearly spherical monomers aggregated into a larger spherical structure.[72] This morphology is comparable to collapsed or aged soot.[32, 81, 82] The mass-mobility exponent, D_{fm}, for this material is 2.83, proving a near spherical morphology.[72]

2.2.3 Determination of Particle mass

Following Radney and Zangmeister (2016) [83, 84] average mass for the 300 nm size-selected BC surrogate particles was determined by scanning an APM using a classification parameter of $\lambda_c = 0.32$; this parameter determines the aerosol penetration and mass resolution by using the ratio of axial and transversal times. Average particle mass was determined from a Gaussian fit of the resulting distributions with contributions of particles bearing a charge (q) = +1; see Radney, et al. 2013. [57 57 57 56 56]

2.2.4 Tandem DMA

The DMA size selects particles based on their mobility within an electric field. To account for multiple charges of the mobility selected particles [83], we performed tandem DMA measurements coupled with a CPC. After atomization and conditioning, the aerosol passed through two DMAs, one to size select the particles at 300 nm, and the other to scan the particles at multiple diameters with a Scanning Mobility Particle Sizer (SMPS). [84] This was performed at multiple dilutions (see Appendix A) of varying dilutions to account for the fractional contributions of +1 and +2 charges. The contribution of the +2 charge is dependent on the number concentration of this specific BC surrogate. Peaks of particles with a +1 and +2 charged were integrated to account for the contribution of each charge. Results indicate that for BC mass concentrations below 2.5 $\mu g\ m^{-3}$ the contribution of particles with charge of +2 is minor, <3%, and reached as high as ≈16% for higher concentrations. The multiple charges were accounted for in m_p determination.

2.2.5 Comparison of CPC to Aethalometer

The response of the filter-based attenuation measurement to a well-characterized aerosol at known mass concentrations (as determined by a CPC and known m_p) was evaluated using the BC surrogate. Aerosols were size selected using a DMA with 9.0 L min^{-1} sheath flow and 0.9 L min^{-1} of aerosol flow. Aerosols were not mass-selected by the APM. After the DMA, the aerosol flow was split between the CPC (0.3 L min^{-1}) and the Aethalometer (0.6 L min^{-1}) for determination of N_p (m^{-3}) and mass concentrations (M_{CPC}, μg m^{-3}). Aerosol flow entering the Aethalometer was monitored with a differential pressure monitor. To calculate M_{CPC}, the N_p was multiplied by the average m_p determined by the APM from mass distribution analysis. The particle mass was later corrected for the contribution of particles possessing a q + 2 charge using tandem DMA (See Appendix A).

The instrument's filter tape was advanced before each run of approximately fifty minutes. It automatically advances when the filter tape reaches an attenuation of 75%. The filter-sampled aerosol was diluted with HEPA-filtered, dry air to compensate for the additional ≈ 5.4 L min^{-1} of volumetric flow required; this also prevented excessive attenuation. This dilution factor was included when scaling the concentrations measured by the CPC (M_{CPC}) to those reported by the filter-based instrument. The volumetric flow rate of the Aethalometer was controlled by an external pump, and the HEPA filtered air dilution was controlled using a mass flow controller. The flow for the air dilution and the Aethalometer's volumetric flow rate were monitored for each run with a Bios Flow Calibrator.

2.2.6 Uncertainty Analysis (CPC) and Limit of Detection (Aethalometer)

The manufacturer's uncertainty for the CPC (TSI, Condensation Particle Counter 3775) is quoted as ±10 %. The stability and response of the Aethalometer was tested by sampling HEPA filtered air for approximately 6 hours with readings every two minutes. Due to instrument noise and drift, results showed an uncertainty (defined as three times the standard deviation, 3σ) of ±0.0802 μg m^{-3} at 880 nm (signal noise for every hour) and an average indicated concentration of -0.0023 μg m^{-3}. At 660 nm the average indicated equivalent mass concentration was -0.00074 μg m^{-3} with a 3σ uncertainty of ±0.054 μg m^{-3}, while at 370 nm the average equivalent mass concentration was -0.00057 μg m^{-3} with a 3σ uncertainty of ±0.0299 μg m^{-3}. The uncertainty in measurements of BC in ambient air is greater due to filter loading, coating, and interference from other absorbing species, as described below. Flows were measured using the Bios DryCal Definer 220 Flow Calibrator. The uncertainty associated with the flows for this experiment is approximately 2%.

2.3 Results

2.3.1 Evaluation of the performance of the Aethalometer: Low mass concentrations.

The BC surrogate was used to evaluate the performance of an Aethalometer by using particles with known size and mass. The BC equivalent mass concentrations measured by the filter-based instrument were compared to those measured by the APM (for particle mass) and CPC (M_{CPC}). The contribution of multiply charged particles to the number concentration was determined with tandem DMA (q>+1 particles were < 3%). The particle mass for D_m = 300 nm was 11.6 ±0.9 fg (1σ).

The *eBC* reported by the Aethalometer was compared to M_{CPC} at low *eBC* (< 2.5 μg m^{-3}) using the manufacturer's default parameters at λ = 880 nm, 660 nm and 370 nm; see Figure 2a (dashed line represents 1:1). This is the same Aethalometer data (for λ = 880 nm only) as presented by Zangmeister et al. 2019, [71 71 71, 70] where the fractional contribution of multiple charges was determined by a different set experiments involving tandem DMA and accounted for in m_p. The m_p values are within measurement uncertainty of each other. This mass concentration range is comparable to ambient BC mass concentrations observed within the continental United States. [85] For 0 μg $m^{-3} \leq eBC \leq$ 2.5 μg m^{-3} the liner regression of *eBC* versus M_{CPC} at λ = 880 nm exhibited a slope of 0.951 ± 0.004; fit uncertainties represent the 1σ standard errors of the residuals of the linear function. The slope at λ = 880 nm of *eBC* illustrates that over this concentration range, the BC surrogate is slightly underestimated by the Aethalometer in comparison to measurements by the APM and CPC. At shorter wavelengths (Figure 2.2b), weaker agreement between the two techniques was observed. At λ = 660 nm the slope was 0.919 ± 0.004 and at λ = 370 nm was 0.654 ± 0.003. The decreasing slope at decreasing wavelength (i.e. larger deviations from 1:1) and concomitant underestimation of eBC is attributed to size dependence, and the disagreement of the measured SG values compared to those recommended by the manufacturer. This disagreement is due to the assumption that all BC should have a wavelength dependence of unity, and the assumed SG size independence. These results illustrate that at low *eBC*, corrections are necessary, but linear; the uncorrected Aethalometer's BC mass concentration readings are

approximately 5% below the *in-situ* technique at λ = 880 nm and 35% below at λ = 370 nm.

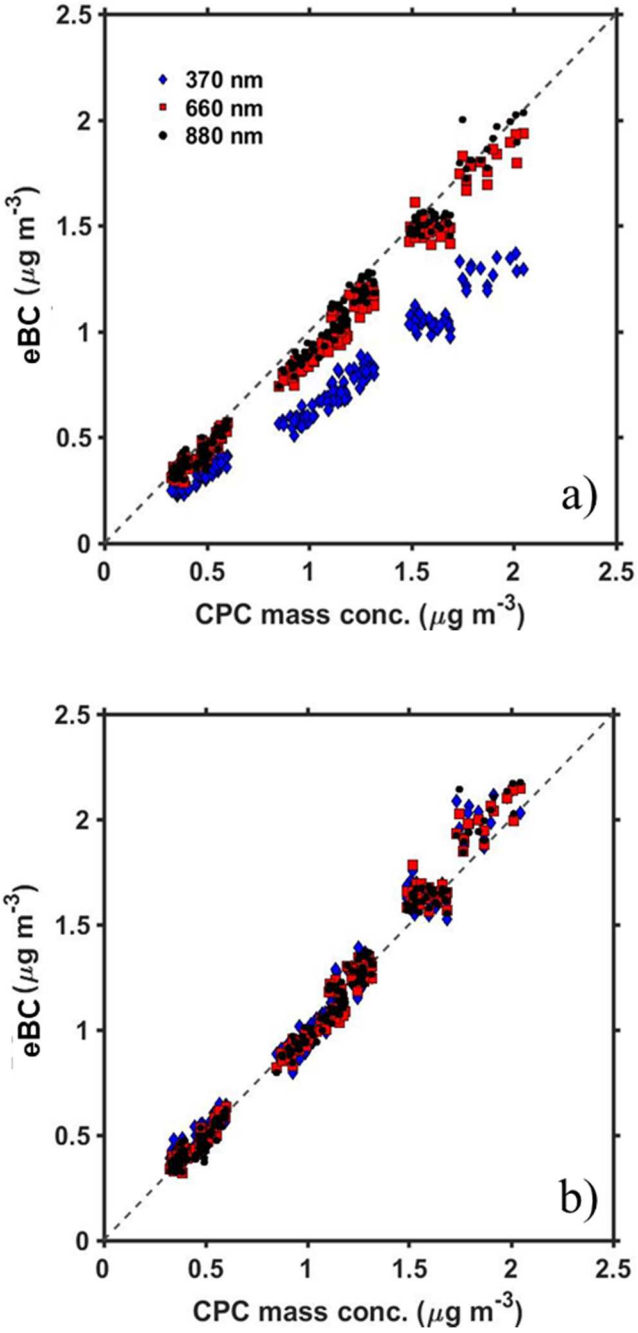

Figure 2.2 *(a) Correlation of CPC mass concentration with eBC (BC equivalent mass concentration: μg m^{-3}) at three different instrumental wavelengths: 370, 660 and 880*

nm. Observations are for low mass concentrations (< ≈2.5 μg m^{-3}) for particles with a mobility diameter of 300 nm. (b) Correlation at low mass concentrations with corrected SG values. Intercepts of best-fit lines were forced to zero. Less than a 1% impact was observed on the slope.

2.3.2 Wavelength Response for the BC Surrogate & *SG* Correction Factors.

The spectral response of the filter-based instrument was evaluated for BC surrogate particles. Previous studies have used the spectral response to infer the presence of BC and other light absorbing aerosols during ambient measurements [86-88]. For the 300 nm mobility selected aerosol, the A_tAE value [89] of the BC surrogate was calculated using the 7-wavelength Aethalometer and compared to the previously mentioned wavelength dependence determined by PAS. [71] The experimentally determined A_tAE from the Aethalometer was 0.71 ±0.05 over 520-880 nm. This data is representative of a run with a reported average *eBC* of 1.19 (±0.05) μg m^{-3}; in a regime where the filter-loading correction is not required. A_tAE is different (by approximately 7%) from the A_bAE (0.76) because attenuation measurements include absorption, scattering, and the filter substrate effects, while the A_bAE is determined *in-situ* with PAS for pure absorption.

Experimental SG values for Cab-O-Jet were determined by using the in-situ mass concentrations measured by the CPC, along with the m_p from the APM mass distributions (i.e. M_{CPC}) as the reference, and the calculated values of the filter-based attenuation coefficients (using Equations 2 and 3). This allowed us to define what the actual *SG* values should be for the Aethalometer at multiple wavelengths for this specific BC material (mobility diameter of 300 nm); see Table 2.1. There is greater

deviation from the manufacturer's recommendation for shorter wavelengths, as shown below.

Table 2.2 *Calculated SG values (and standard deviations) for three separate runs with 300 nm Cab-O-Jet particles for mass concentration up to ≈2.5 μg m^{-3}. Also shown is the percent deviation from the manufacturer's constant values for SG at multiple wavelengths.*

Wavelength (nm)	Calculated Avg. *SG* (m^2 g^{-1}) (+/-1σ)	Deviation from manufacturer (%) (+/-1σ)
370	25.2 ± 1.4	-36 ±6
470	24.0 ± 1.3	-23 ±5
520	22.7 ± 1.1	-19 ±5
590	20.6 ± 1.4	-17 ±7
660	20.0± 0.9	-9.8 ±5
880	15.6± 0.6	-6.3±4
950	14.5 ± 0.5	-6.0±3

The newly determined *SG* values for the BC surrogate (mobility diameter of 300 nm) were used to correct for the low and high mass concentration ranges of data as shown in Figures 2.2b and 2.3b for each individual data point. When the corrected *SG* values were applied for the lower mass concentration range correlation, the slope for all wavelengths moved closer to unity (Table 2). Slope values are not exactly 1.00, but are within 3% of unity because each individual mass concentration reading was corrected by the average *SG* values.

Table 2.2 *Best fit slope (where the y-intercept is forced through zero) values for BC up to 2.5 μg m^{-3} for the raw data and the data corrected for the newly determined SG values.*

Wavelength (nm)	Slope w/out correction (+/-1σ)	Slope with *SG* corrections (+/-1σ)	R^2
370	0.654 (±0.003)	1.025 (±0.005)	0.99
660	0.919 (±0.004)	1.019 (±0.004)	0.99
880	0.951 (±0.004)	1.018 (±0.004)	0.99

2.3.3 Evaluation of the performance of the Aethalometer: Larger range of BC mass concentrations.

Higher *eBC*, representative of ambient BC concentrations found near sources or in more polluted environments such as cities in China [90] and India,[80] can lead to different results. Shown in Figure 2.3a are results for BC surrogate mass concentrations between 0 and ≈20 μg m^{-3}. At this higher mass concentration range, the slope of *eBC* relative to M_{CPC} at all wavelengths decreased and deviations from unity increased. At λ = 880 nm, 660 nm and 370 nm the slopes were 0.728 ± 0.006, 0.656 ± 0.006 and 0.426 ± 0.005, respectively. When the wavelength decreases, the underestimation of *eBC* increases, and this is consistent with the low mass concentration study presented earlier. This is consistent with previous reports showing loading and shadowing effects.[21, 76]

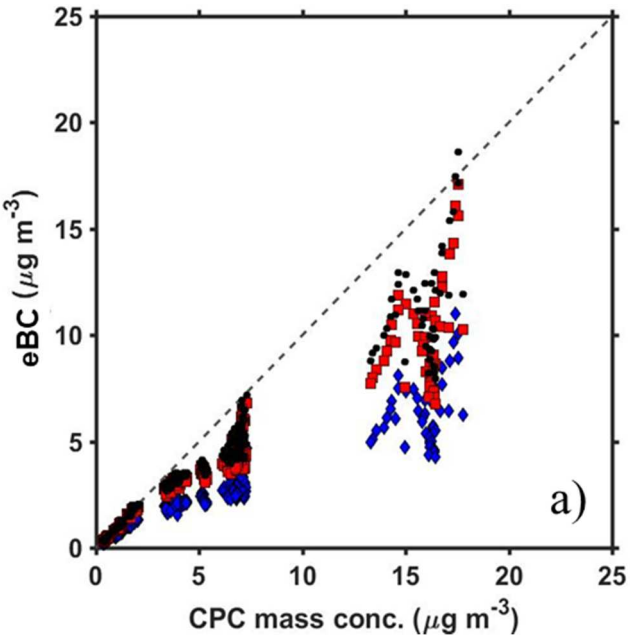
eBC (μg m^{-3})
CPC mass conc. (μg m^{-3})
0
5
10
15
20
25
a)

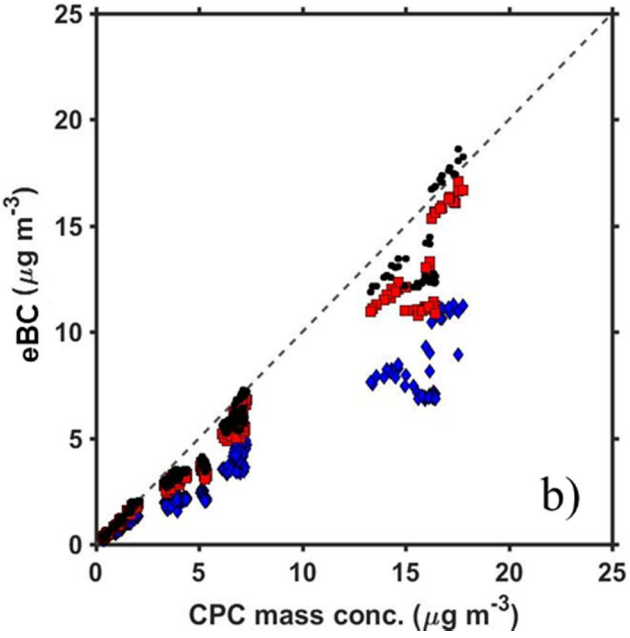
eBC (μg m^{-3})
CPC mass conc. (μg m^{-3})
0
5
10
15
20
25
b)

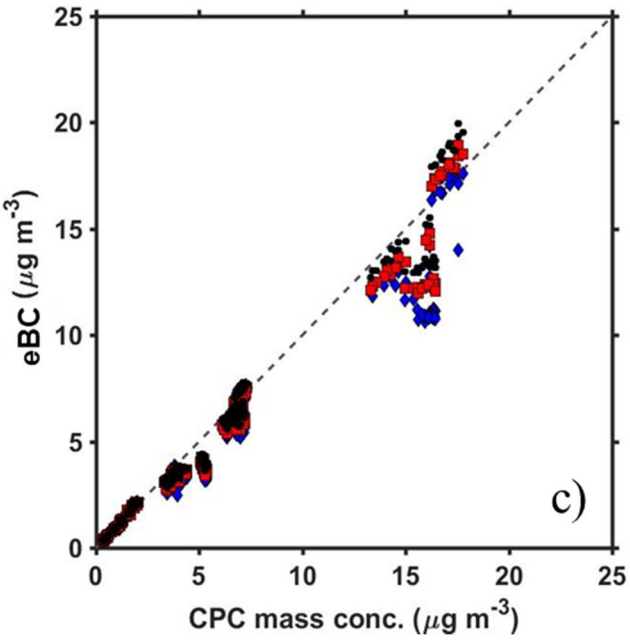

Figure 2.3 *Results for eBC up to ≈20 μg m^{-3} (a) Correlation of CPC-determined mass concentration with uncorrected filter-based eBC. (b) Correlation of CPC mass concentration eBC up to 20 μg m^{-3} with only the loading correction (described in Appendix A) applied. (c) Correlation of CPC mass concentration with eBC with both the loading correction and corrected SG applied.*

With the BC surrogate measured in this work, the Aethalometer signal decreased monotonically in time, as shown by the black diamonds in Figure S3 (Appendix A) (λ = 880 nm) due to shadowing. After 50 min, the indicated *eBC* was ~ 40% lower than at the onset of measurements as seen in Figure A3 in Appendix A. The CPC measured mass concentration indicated that the measured mass concentration (blue circles) remained constant within 3%. To correct for the nonlinear attenuation response as a function of filter loading at a constant loading rate (i.e., constant particle mass concentration), the loading correction technique described

in Jimenez et al. 2007 [76,75] was applied. More information on how this correction was applied can be found in Appendix A.

As depicted in Figure 3b above (and Table 2.3), for the larger range in mass concentrations, the slope of the M_{CPC} mass versus *eBC* at λ = 880 nm improves (from 0.728) to 0.881 (±0.005) (R^2=0.97) when just the loading correction is applied. The slope at λ = 660 nm and 370 nm also improve to 0.812 (±0.005) and 0.543 (±0.004), respectively, moving closer to unity, and showing the importance of a loading correction when operating at higher mass concentrations. However, the continued underestimation of *eBC* relative to M_{CPC} suggests that we examine the SG values for this surrogate at high concentrations.

Table 2.3 *Best-fit slope (where the y-intercept is forced through zero) values up to 20 μg m^3 for the raw data and the data corrected for the shadowing effect and newly determined SG values.*

Wavelength (nm)	Slope w/out correction (+/-1σ)	Slope with loading and *SG* corrections (+/-1σ)	R^2
370	0.426 (±0.005)	0.851 (±0.007)	0.95
660	0.656 (±0.006)	0.900 (±0.006)	0.97
880	0.728 (±0.006)	0.943 (±0.005)	0.97

After the loading correction was applied, our larger ranged BC mass concentration data (0-20 μg m^{-3}) was also adjusted with our newly determined *SG* values found in Table 3.3. At λ = 880 nm, 660 nm and 370 nm the slopes were 0.943 ± 0.005 (R^2=0.97), 0.900 ± 0.006 (R^2=0.97) and 0.851 ± 0.007 (R^2=0.95), respectively. Overall, the usage of the loading correction and the new, adjusted SG values are necessary to correct for BC mass concentration as observed in Figure 3c.

2.3.4 BC Coating with Ammonium Sulfate

To evaluate the Aethalometer's response to the BC surrogate for internally mixed particles, BC was co-atomized with AS. These coated particles (diameter = 300 nm), where the BC was embedded in an AS shell, were first used to evaluate the performance of the Aethalometer at BC mass fractions of 7%, 14%, and 20.5%, using the manufacturer's pre-programmed SG values. Upon atomization and drying, these internally mixed particles with differing amounts of BC exhibited similar total particle masses of 25.8 ± 0.2, 25.3 ±0.4 and 24.3 ±0.5 fg, respectively. All particles exhibited a q+2 < 4% by number. The greater the coating, the greater the deviation from values for pure BC. Table 2.4 provides best fit slope values when the y-intercept is forced through zero.

Table 2.4 *Values of the slope and 1σ when the y-intercept is forced through zero for the multiple mass fractions of BC with AS. Best fit correction factors are the inverse of these slope values.*

Mass Fraction of BC with AS mixtures	Slope (±1σ) 880 nm	Slope (±1σ) 660 nm	Slope (±1σ) 370 nm
0.07	1.456 (± 0.008)	1.594 (± 0.008)	1.545 (± 0.009)
0.14	1.185 (± 0.006)	1.286 (± 0.006)	1.168 (± 0.009)
0.205	1.183 (± 0.007)	1.246 (± 0.008)	1.018 (± 0.009)

For internal mixtures of BC with non-absorbing materials, the absorption as measured by the Aethalometer was enhanced, consistent with core-shell Mie calculations and laboratory experiments [78]. This absorption enhancement is most prominent at the lowest (7%) BC mass fraction internal mixture. The Aethalometer exhibits the strongest absorption enhancement at λ = 660 nm for an internal mixture

consisting of BC and AS. This artefact of the Aethalometer needs to be accounted for because ambient measurements often contain coated particles.

For internal BC and AS mixtures, the Aethalometer's wavelength dependence (or Attenuation Ångström Exponent, A_tAE, wavelength range 520-880 nm) using preprogramed SG values increases with a decrease in BC, climbing from 1.03 for 20.5%, to 1.21 for 14% and 1.31 for 7% BC. Retrieving spectral data may help approximate BC mass fraction in ambient particles, although spectral data also depends on particle size distribution.

2.3.5 Brown Carbon Absorptivity

We seek to determine the response and level of interference that brown carbon (BrC) causes in BC measurements with this attenuation-based instrument. Aerosols composed of organic brown carbon (BrC) absorb radiation at visible, and with increasing strength into near ultra-violet wavelengths. [78] It is imperative to properly quantify the absorptivity of BrC for its contribution to the radiative forcing budget. BrC is chemically distinct from BC, but generates a signal in absorption-based instruments. We generated 300 nm BrC aerosol using the HA surrogate as described above. All BrC particles exhibited a q+2 < 2% by number. Results, Table 5, depict a greater sensitivity at shorter wavelengths as indicated by the slope.

Table 2.5 *Response of the Aethalometer to pure BrC surrogate. The second column is the slope of Aethalometer signal vs. BrC mass concentration with the y-intercept*

forced through zero. Response of BrC decreases as the detection wavelength increases.

Wavelength (nm)	Slope (±1σ)
880	0.020 (±0.007)
660	0.058 (± 0.007)
370	0.200 (±0.020)

At the shortest wavelength reported, BrC attenuates radiation with approximately 20% of the efficiency of BC. However, at λ = 880 nm, this falls to 2%, and BC readings of the Aethalometer were near the limit of detection for up to 4.0 μg m^{-3} BrC. These results indicate that BC measured at 880 nm shows little interference from unmixed BrC particles.

The results presented in here indicate an A_tAE of 3.7 (± 0.2) for HA at λ = 520 nm and 880 nm. Prior work determined the A_bAE of this BrC surrogate as 5.31 ± 0.14 for particles with a smaller mobility diameter of 250 nm [72]. This large wavelength dependence is consistent with previous studies of organic aerosol [67]. Using a BrC surrogate to evaluate the wavelength dependence of the Aethalometer will help with aerosol classification when sampling ambient particles.

2.3.6 Coated with a BrC surrogate

BC absorption is also amplified when internally mixed with organics [72], [91]; see Bueno et al. 2011[35] and review by Bond and Bergstrom 2006. [25] [25] Here, we evaluated a 14% BC (mass fraction) internally mixed with the BrC surrogate and compared the Aethalometer to an *in-situ* technique. These experiments are meant to simulate internally mixed BC particles as seen in biomass burning [86],[64].

Multiple charging effects are assumed to be negligible (q+2 ≤ 2%) due to previous results of multiple charging from BrC particles at similar number concentrations. The response of the Aethalometer using the default SG (Figure 4) at λ = 880 nm is about 12% greater than unity, (1.12 ± 0.01) increases to 1.47 ± 0.01 at 660 nm, and reaches a maximum of 1.68 ± 0.01 at 370 nm. Even at the long wavelength of 880 nm and low mass concentrations, the signal is enhanced substantially when the BC is internally mixed with BrC.

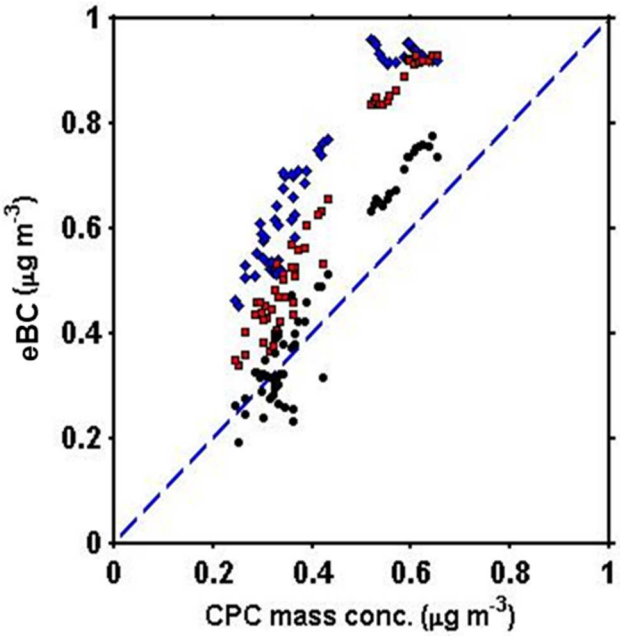

Figure 2.1 *Response of Aethalometer at 370 nm (blue diamonds), 660 nm (red squares) and 880 nm (black circles) to the CPC-derived BC using a 14% BC mass fraction solution with BrC. The coating causes a positive interference that increases at shorter wavelengths.*

These mass concentration values can also be used to measure the A_tAE from the Aethalometer. For this internal mixture of a low absorbing material embedding a highly absorbing material, the A_tAE was 1.7 ± 0.1 (λ = 520-880 nm). This is in rough

agreement with the value of 1.91 ± 0.05 derived for 250 nm particles at 13% BC in BrC, although different mobility diameters [72]. Our A_tAE value from the Aethalometer for the internally mixed particle of BrC with BC is more than double the A_tAE reported for the uncoated BC particle and sufficient to distinguish pure BC from such mixtures. Understanding the wavelength response of these internally mixed particles with the Aethalometer can provide more information about the composition of atmospheric particles in existing data sets.

2.4 Discussion

The BC surrogate Cab-O-Jet with high elemental carbon content and nearly spherical morphology appears a suitable material for the evaluation and calibration of the filter-based attenuation instruments. For pure BC and mass concentrations below 2.5 μg m^{-3}, the Aethalometer (with default values at 880 nm) responds linearly and with good precision, ~5%, when compared to a reference method. Greater corrections are needed at shorter wavelengths, nearing 35% at 370 nm.

The Aethalometer was also evaluated for high mass concentrations of nearly pure BC (up to 20 μg m^{-3}). This instrument showed a greater need for correction at higher loadings, with an underestimation of approximately 30% at 880 nm, increasing to 57% at the shortest wavelength of 370 nm. Each individual run accounted for this shadowing effect and loading correction. When the newly-derived *SG* values were applied, the indicated BC mass concentrations at multiple wavelengths improved, and were closer to unity.

BC particles coated with a non-absorbing material (AS) were generated to determine the response of the Aethalometer to internally mixed aerosols, common in

ambient air. In 2004 and 2005, for example, BC accounted for approximately 15-20% of PM 2.5 mass in NYC and 7-10% in Rochester, NY [92] suggesting that the Aethalometer would overestimate BC mass concentrations unless corrected for the absorption enhancement effect. Using at λ = 880 nm, the Aethalometer overestimated the reported BC mass concentrations by 46%, 19% and 18% for BC mass fractions of 7%, 14% and 20.5%, respectively. This indicates that ambient data where BC is a minor component of the total aerosol mass, may need large corrections to retrieve true BC mass concentration. The wavelength response (A_tAEs) to particles with 7%, 14% and 20.5% BC mass fraction are approximately 85% (1.31), 70% (1.21) and 45% (1.03) higher than for uncoated BC particles. Deriving the wavelength response does provide information about the mixing state and composition of sample aerosol. Speciation of aerosols (or knowledge of the bulk composition) will help with source identification for reduction purposes. For a given air parcel, the response at multiple wavelengths, can better characterize the nature and concentration of absorbing aerosols.

Our BrC surrogate generated a slight interference with BC measurement at 880 nm that gradually increased at shorter wavelengths. When using the default wavelength of 880 nm, the BrC surrogate showed a small SG of 0.332 $m^2 g^{-1}$ and the rejection ratios are approximately 50:1, 17:1 and 5:1 at wavelengths of 880 nm, 660 nm and 370 nm, respectively. In other words, 50 μg of this particular BrC surrogate generates a signal (λ= 880 nm) equivalent to 1 μg of BC. Although this instrument is meant to measure BC, BrC shows a strong wavelength response as denoted by its relatively high A_tAE value of 3.7. The wavelength response for this BrC surrogate

provides semi-quantitative information that will help distinguish mixtures of BC and BrC for ambient sampling.

To mimic possible conditions in the atmosphere, BC was also internally mixed with BrC (14% BC by mass). The wavelength response for this internally mixed material is approximately 2.4 times greater than the wavelength response of BC alone. The Aethalometer's A_tAE and its sensitivity to BrC coating will aid in aerosol classification for ambient measurements taken with this filter-based instrument.

. Having the ability to correct for the instrumental artefacts will allow for better understanding of light-absorbing aerosol. Knowledge of the bulk composition of the aerosol through complementary measurements with supplementary instrumentation may help improve quantification of this filter-based instrument.

2.5 Conclusions

The commercial filter-based instrument, the Model AE31 Aethalometer, was successfully evaluated using a well characterized BC surrogate under laboratory conditions. From this study we were able to make several conclusions in regard to using this specific light absorbing surrogate. The results and recommendations are summarized as follows:

- At lower mass concentrations (<2.5 μg m^{-3}), the Aethalometer responds with good accuracy at λ = 880 nm. *eBC* measurements at lower wavelengths require a greater correction for SG.
- Higher mass concentrations of BC require a correction that accounts for the loading effect.

- Internally mixed BC particles with AS overestimate (18-46%) reported BC mass concentration from the Aethalometer. The A_tAEs are higher for coated BC particles than for uncoated BC particles.
- The wavelength response from the Aethalometer provides information on the mixing state and may aid in source apportionment.
- The BrC surrogate showed strong wavelength dependence where the reported mass concentration peaked at the lower wavelengths, and generally decreased at longer wavelengths.
- BC internally mixed with BrC showed an absorption enhancement and a greater wavelength response than unmixed BC particles.
- Corrections presented in this work are applicable to this BC mimic.

Chapter 3: Evaluation of Thermal Optical Analysis (TOA) using an aqueous binary mixture

Grimes, C.D., Conny, J.M. and Dickerson, R.R., 2020. Evaluation of thermal optical analysis (TOA) using an aqueous binary mixture. Atmospheric Environment, 241, p.117647.

3.1 Introduction

Black carbon (BC), a form of atmospheric particulate matter (PM), influences Earth's radiative budget, local visibility, and adversely impacts human health [5]. BC is a component of soot with graphite-like structures, where the particles are chemically inert. As a refractory material, BC is also known as elemental carbon (EC). Due to different combustion conditions, atmospheric mixing and aging, these light absorbing particles often are combined with organic carbon (OC), mineral dust, and nitrates [93]. There is much discrepancy associated with the quantification of BC among different techniques. Some of the filter-based techniques include optical methods such as aethalometry [15] and the combination of optical and thermal based characterization [94] such as thermal-optical analysis (TOA). Since TOA functions optically as well as thermally, it is an appropriate method for determining the mass of BC as a light-absorbing material in the atmosphere. TOA is known to be problematic because different temperature protocols provide inconsistent results for BC, and measurements can disagree greatly with other BC quantification techniques [24, 95-97]. This study presents a new technique incorporating a binary solution of known concentrations of OC and BC to evaluate TOA methods involving different

temperature protocols. The technique presented here could serve as a calibration method for characterizing TOA.

A Sunset Thermal-Optical Carbon Aerosol Analyzer* was used in this work (Sunset Lab, Tigard, OR). A section from a quartz-fiber filter is placed on a quartz boat in the path of a 670 nm laser beam to monitor the change in transmittance through the filter as the sample is heated. The technique is known as thermal-optical transmission analysis when laser transmission is used and thermal-optical reflection analysis when reflection is utilized. Carbon species are evolved from the quartz filter in the front oven upon heating and converted to carbon dioxide in a MnO_2 oxidation back oven at 870^{o}C. The first phase of the analysis occurs in an oxygen-free helium environment, where some organic compounds are pyrolytically converted to EC in the front oven. As OC pyrolyzes and becomes darker, laser transmittance through the filter decreases. The second phase occurs in an oxygen/helium environment where the pyrolyzed OC and EC are oxidized to carbon dioxide and laser transmittance through the filter increases. This CO_2 is reduced to methane in a 500^{o}C Raney nickel catalyst oven before passing into a flame ionization detector. The instrument distinguishes the OC from EC when the transmittance of the filter returns to its original value – the split point. Carbon detected after the split point is measured as BC that was native to the sample. Following the detection of carbon, a known amount of methane is injected into the sample oven, then oxidized and reduced back to methane, which is the method's internal standard [22, 98-100].

3.2 Materials & Methods

A 1 mg/mL suspension of Cab-o-Jet 200 (19.92 % mass fraction, Cabot Corp.) was prepared with deionized water. [101] The carbon black material acts as an EC surrogate and has been well characterized.[71, 72] Prior research with TOA showed that this material is comprised of approximately 96 % EC and 4 % OC. A separate 4.0 mg/mL solution of sucrose was prepared to act as an OC surrogate. Sucrose is a suitable material for OC for ambient air organic aerosol because a substantial amount of its carbon pyrolyzes (chars) when heated in an inert atmosphere. From the two separate EC and OC preparations, a 10.0 mL binary mixture was prepared, where 7.0 mL was the OC solution and 3.0 mL was the EC suspension. A syringe was used to deposit 10.0 μL aliquots onto a 1.00 cm^2 quartz filter. The filter remained in the front oven until it was dry. Measurements of the binary mixture were taken with different temperature protocols. The concentrations of EC, OC, TC and EC/TC ratios were recorded. Details concerning the parameters of the different protocols are provided in Results/Discussion.

3.3 Results and Discussion

Tables 3.1 and 3.2 provide the temperature steps and residence times for the protocols developed between the National Institute of Standards and Technology (NIST) and the Environmental Protection Agency (EPA), and are modified versions of the NIOSH method. The temperature protocols include NIST-EPA-A, NIST-EPA-B, NIST-EPA-C and Quartz. The Quartz protocol (Table 2) was developed by the manufacturer early on and is based, in part, on work by Birch and Cary [100] which has

also led to the NIOSH 5040 method [102]. Background research for the NIST-EPA-A, NIST-EPA-B and NIST-EPA-C methods is given in Conny et al. 2007 [23]. The well-known Interagency Monitoring of Protected Visual Environments (IMPROVE) protocol is utilized primarily for thermal optical reflectance, and is not appropriate for the thermal optical transmittance instrument used in this work. The temperature steps for the IMPROVE protocol are significantly lower than the protocols used in this work, and may not evolve all of the OC [103].

Table 3.1 *Temperature steps and residence times for the NIST-EPA-A,-B and -C protocols.*

Carrier Gas (step)	Temperature (ºC)			Residence Time (s)		
	A	B	C	A	B	C
He (1)	200	200	200	60	60	60
He (2)	400	400	400	60	60	60
He (3)	600	600	600	60	60	60
He (4)	830	830	785	150	73	150
$He+O_2$ (1)	550	380	550	60	60	60
$He+O_2$ (2)	620	484	620	60	60	60
$He+O_2$ (3)	690	588	690	45	45	45
$He+O_2$ (4)	760	692	760	45	45	45
$He+O_2$ (5)	830	796	830	45	45	45
$He+O_2$ (6)	900	900	900	180	90	90

Table 3.2 *Temperature steps and residence times of the Quartz protocol.*

Carrier Gas (step)	Temperature (ºC)	Residence Time (s)
He (1)	315	60
He (2)	475	60
He (3)	615	60
He (4)	870	90
$He+O_2$ (1)	550	45
$He+O_2$ (2)	625	45
$He+O_2$ (3)	700	45
$He+O_2$ (4)	775	45
$He+O_2$ (5)	850	45
$He+O_2$ (6)	910	120

The NIST-EPA methods were derived from response surface models created from a factorial experimental design involving temperature, duration of the high temperature step, and the increase in heat in the He-Ox phase [24]. These protocols were designed to deal with the split point for differing sample types. Response surface models were calculated for absorption cross sections of pyrolyzed OC and EC. The models revealed the step temperatures and durations, and in the case of step 4 (final helium step), a range of possible step temperatures that ensures OC charring is minimized to avoid OC being measured as EC by the instrument after the split point. The primary differences between NIST-EPA-A and NIST-EPA-B are the step 4 duration times and first step in the He-Ox phase. In comparison to NIST-EPA-A, the NIST-EPA-C protocol has a relatively low temperature for step 4 in helium. The NIST-EPA-C protocol is considered suitable protocol for a variety of sample types (high-charring and low-charring) [23]. Examples of temperature profiles, split points and FID responses are shown in Figures 1a-d.

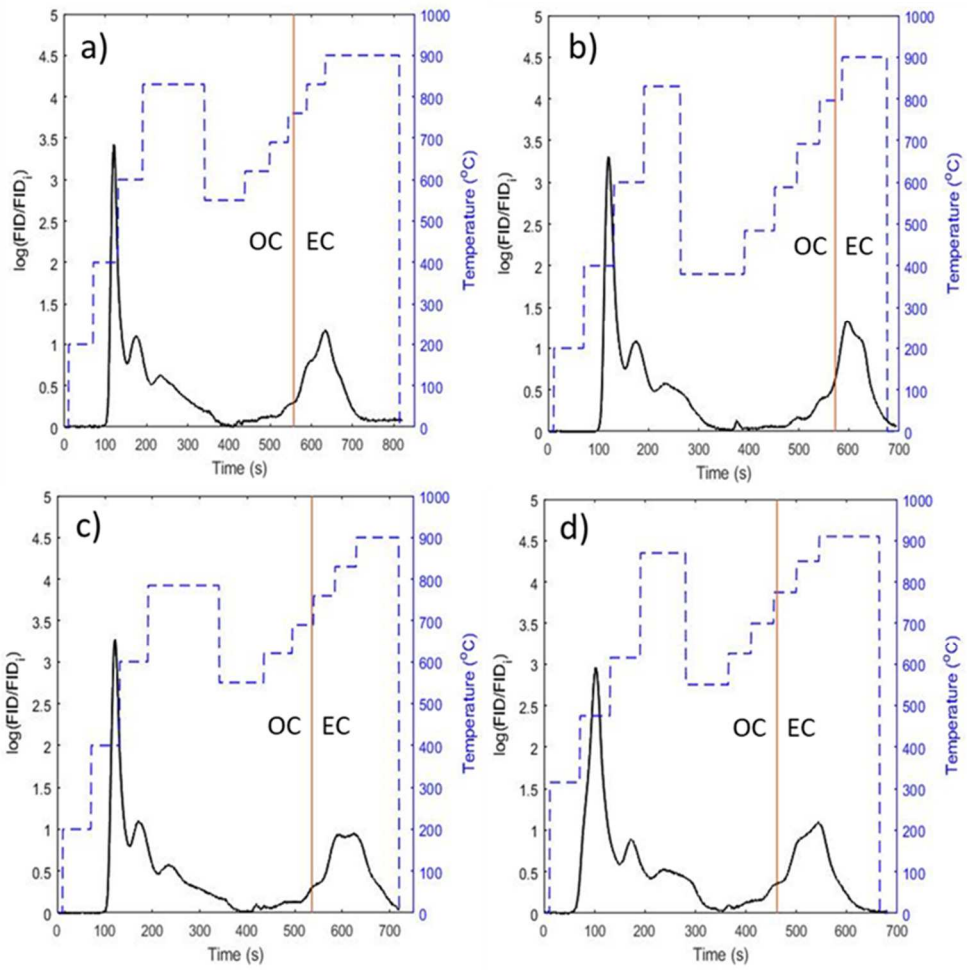

Figure 3.2 *Thermograms produced in response to the binary solution with a reference TC value of 15.03 µg/cm^2 and EC/TC ratio 0.213. The red solid line is the split point, the blue dashed lines are the temperature steps. The black solid line is the FID response. Thermograms using (a) NIST-EPA-A (reported values of TC=15.19 µg/cm^2 and EC/TC=0.215); (b) NIST-EPA-B (reported TC=14.89 µg/cm^2 and EC/TC=0.209); (c) NIST-EPA-C (reported values of TC=15.17 µg/cm^2 and EC/TC=0.222); (d) Quartz (reported values of TC=15.51 µg/cm^2 and EC/TC=0.218).*

Per 10 µL aliquot of the binary mixture, 11.86 ± 0.21 ($\bar{x} \pm s$) µg of OC and 3.18 ± 0.17 µg of EC were deposited onto the 1.00 cm^2 quartz filters, with a total

carbon of 15.04 ± 0.83 µg. The calculated EC/TC ratio was 0.211 ± 0.012. This ratio allows for simple numerical comparison amongst the different protocols, and it is important for the determination of optical properties of ambient aerosols. These are the calculated reference values with propagated error. The reference values consider the 96 % EC composition of the surrogate material determined with prior research [71]. Multiple runs and blanks of deionized water were performed for each temperature protocol. Averages and standard deviations of OC, EC, TC and EC/TC for the different temperature protocols and number of replicates are presented in Table 3. Reference values in Table 3 are amounts in the 10 µL aliquot from the binary mixture.

When compared to the reference values, the NIST-EPA-C protocol produced results for OC, EC, TC and EC/TC which had an error of less than 2 % for all measurements. However, the standard deviations are relatively high for EC but low for TC. NIST-EPA-C reported the highest coefficient of variation for the OC component while NIST-EPA-B reported the largest coefficient of variation for the EC component. All protocols reported average TC values within 0.5 µg (< 3 %) of the calculated reference TC value.

Table 3.3 *Averages and standard deviations of OC, EC, TC and EC/TC for different temperature protocols compared to the calculated reference values. Uncertainties of the reference values are propagated errors from glassware and the balance used for volume and mass measurements. The numbers of replicates are given by n.*

	NISTEPA-A (n = 6)	NISTEPA-B (n = 3)	NISTEPA-C (n = 6)	Quartz (n = 5)	Reference
OC ($\mu g/cm^2$)	11.51 ± 0.72	11.57 ± 0.52	11.85 ± 1.04	11.29 ± 0.74	11.86 ± 0.21
EC ($\mu g/cm^2$)	3.04 ± 0.36	3.36 ± 0.58	3.15 ± 0.23	3.24 ± 0.25	3.18 ± 0.17
TC ($\mu g/cm^2$)	14.55 ± 0.68	14.93 ± 1.02	15.00 ± 1.09	14.54 ± 0.70	15.04 ± 0.83
EC/TC	0.21± 0.03	0.22 ± 0.02	0.21 ± 0.02	0.22 ± 0.02	0.21 ± 0.01

3.4 Results and Discussion

This novel procedure characterizes the thermal-optical transmission instrument with a binary mixture consisting of elemental carbon and sucrose. The approach incorporates a colloidal suspension of carbon black that can easily be deposited onto quartz filters. As reported in Lack et al. 2014 [32], there is a need for an EC surrogate for TOA, which may be fulfilled with a well-characterized carbon black suspension with properties similar to Cab-O-Jet 200. All 4 methods provided adequate results of EC, OC, EC/TC ratios, and indicated components were within the combined uncertainty of measurements and reference values. The work presented here also proves the instrument's determination of the split point can be reasonably obtained for this binary mixture of OC and EC.

A one-way analysis of variance (ANOVA) performed among the four temperature protocols (treatments) showed no difference in the protocols for OC, EC, TC, or EC/TC at a significance level of 0.1. For example, the within-treatment mean squares for EC were larger than the between-treatment mean squares by a factor of

1.43. However, the ANOVA was based on data from only a single instrument. Other thermal-optical transmission instruments may have better measurement precision and thus lower within-treatment mean squares, which might reveal significant differences among the protocols. In addition, other formulations of the binary mixture or expanding the mixture to three or more components (e.g., EC, OC, and a metal oxide component) may result in significant differences among the protocols. Nevertheless, a water-based mixture, such as the one presented here, serves as a possible material to optimize the step temperatures and durations in TOA for correctly determining the split point, and thus to improve the quantification of BC. Additional TOA calibration mixtures with a water-soluble carbon black material should be investigated in the future.

Chapter 4: Ground and aircraft-based measurements of black carbon (BC) and carbon monoxide (CO) in the New York City (NYC) metropolitan area: Comparison to emissions inventories.

*This chapter is an advanced copy of a paper to be submitted to Environmental Science and Technology.

4.1 Introduction

Black carbon (BC), a component of particulate matter (PM) emitted from incomplete combustion, absorbs radiation from the near UV to the near infrared (IR). It consists of carbon in chain links and aggregates. BC is an important driver of global warming with climate forcing similar in magnitude to methane. Estimates have shown that BC aerosol has a global radiative forcing of approximately +0.9 Wm^{-2} (range of +0.4 to +1.2 Wm^{-2}).[5, 104] Using bottom up inventories, the total global emission of BC in the year 2000 was approximately 7500 Gg yr^{-1} with a relatively large uncertainty range of 2000 to 29000 Gg yr^{-1} BC.[5] This form of particulate matter is also known to play a role in cloud properties. BC is also associated with cancer, respiratory, and cardiovascular diseases (US EPA, https://www3.epa.gov/airquality/blackcarbon/). Proper and accurate quantification of its concentrations and emissions is necessary for curtailing the negative effects of BC on human health and climate.[9]

Several optical methods have been used to determine in real-time the absorption coefficient and mass concentration of BC. Filter-based instruments draw an air stream onto a filter for transmittance measurements. The attenuation (ATN) coefficient is determined and then converted to an absorption coefficient. Instruments such as the Aethalometer (Magee Scientific, Berkeley, CA) convert absorption

coefficient to mass concentration by using a predetermined factor called the mass absorption cross section (MAC).[15, 16, 105] This instrument measures at seven wavelengths: 370, 470, 520, 590, 660, 880, and 950 nm with 880 nm as the default.[46] Robust and relatively inexpensive, filter-based instruments unfortunately exhibit an inherent error known as the loading effect.[19, 76] BC loading and ATN are linear for low loadings, but as the ATN values become saturated, the relationship between BC loading and ATN becomes non-linear. [106-109] This artifact leads to the underestimation of BC mass concentration and needs to be corrected for. There have been multiple studies on this correction to compensate for the underestimation of BC mass concentration for various filter-based instruments. The Magee AE33 model of the Aethalometer compensates for this artifact in real time by measuring the ATN on two sample spots with different loadings. Two measurements are taken simultaneously with differing accumulation rates to account for the non-linearity of the aerosol of the same physical characteristics. Unlike previous Aethalometers with a pre-determined mass absorption cross section of 16.6 $m^2 g^{-1}$ at λ=880 nm, this new model (with a different filter medium) converts ATN to BC mass concentration using a MAC factor of 7.77 $m^2 g^{-1}$. More information about the measurement principle of the AE33 model can be found in Drinovec et al. 2015.[16]

In an urban environment, the New York City (NYC) area, BC is primarily emitted by diesel engines while gasoline on-road and off-road vehicles and other internal combustion engines such as generators, and VOC oxidation dominate carbon monoxide (CO) emissions.[110] According to the EPA inventory, biomass burning is another large source of BC on a national scale, but probably not in NYC in summer.

In urban areas with heavy vehicular traffic, combustion is a dominant source for both BC and CO. CO has a lifetime of a few weeks to a few months[110, 111] which makes it a good candidate to trace anthropogenic sources.[112] The correlation of BC and CO is a useful way to understand combustion efficiency and to distinguish the different types of combustion sources; emission ratios tend to vary greatly from source to source. Previous studies have shown that the higher the $\Delta BC/\Delta CO$ ratio, the greater the probability of diesel engine emission sources.[113] Recent studies have shown the importance of considering BC emissions from off-road sources because on-road engine sources are becoming better controlled over time.[114] The positive correlation of CO with BC allows for the usage of CO as a reference to calculate the total emissions of BC (E_{BC}) in urban areas like NYC.[115]

The primary source of carbonaceous PM in major cities such as NYC is vehicular emissions and diesel exhaust.[116] NYC is the largest city in the United States (U.S.) with a population of nearly 8.5 million inhabitants in 2014[117] and encompasses five boroughs (Queens, Kings, Richmond, Manhattan and Bronx counties). The NYC metropolitan area also includes Long Island, and northern New Jersey. Previous field work has shown that BC at a NYC site in the South Bronx had an annual mean within the range of 1.4 to 2.0 μg m^{-3}.[92] Approximately 15-20% of the particulate matter with the mobility diameter less than 2.5 μm (PM2.5) was reported as BC in NYC. Average BC mass concentrations were reported statistically higher during the weekdays (Monday-Friday) than the weekends (Saturday-Sunday).[92] A short winter study (25 days) conducted in 2004 found that the hourly averaged BC mass concentrations at a Queens site ranged from 0.23 to 5.87 μg m^{-3} and the mean was

1.03 μg m^{-3} and at the Bronx site the range was 0.47 to 7.67 μg m^{-3} with a mean of 1.38 μg m^{-3}.[116] In a one-year (June 2009-July 2010) study of major air pollutants in Queens and Long Island, carbonaceous particles, commonly referred to as elemental carbon (EC), were quantified using a different measurement technique; thermal optical analysis (TOA). Results from this campaign indicated the EC originates from road traffic, and that weekdays exhibited higher concentrations.[117] BC measurements at the Queens near road site also showed a slight negative correlation with temperature during the summer months, but were weakly positively correlated with temperature for all other months.[92]

In this study, an AE33 Aethalometer was characterized with a BC surrogate and then used for BC measurements during the Long Island Sound Tropospheric Ozone Study (LISTOS). Data shown here is from the summers of 2018 and 2019. In conjunction with CO total emissions from multiple emissions models, the observed ratio of ΔBC/ΔCO in the planetary boundary layer (PBL) was used to estimate total E_{BC} in the NYC metropolitan area. These models include National Emissions Inventory (NEI), the Emissions Database for Global Atmospheric Research (EDGAR) and Fuel-based Inventory of motor-Vehicle Emissions (FIVE). Information on these models is provided in the methods section. The ΔBC/ΔCO ratios taken from an aircraft were compared to the ratios at a near road site in the borough of Queens, NYC for the summer seasons of 2018 and 2019. The difference between aircraft and ground measurements of ΔBC/ΔCO during the weekday and weekend provides insight into the relative contribution of compression ignited (diesel) and spark ignited (gasoline) engines.

4.2 Materials & Methods

4.2.1 Laboratory Evaluations of the Aethalometer using a BC surrogate

For all experiments, BC aerosols were generated from aqueous solutions containing the well suspended, dispersible material Cab-O-Jet 200, or CB, (Cabot Corp., 20.03 wt % solids) using a liquid jet cross-flow atomizer (TSI, Model 3076) and dried by passing through a heated copper coil and diffusion dryer (TSI Diffusion Dryer 3062). This material has been characterized as BC previously in Grimes et al. 2020 (under review), You et al. 2016[72] and Zangmeister et al. 2019.[107] The heated copper coil was maintained at 100°C to evaporate water, and then the diffusion dryer removes excess water in the air stream. BC aerosol concentrations were controlled by varying the solution concentration and via dilution with ultra-purified water.

An Aerodynamic Aerosol Classifier (AAC, Cambustion, Cambridge, UK), Differential Mobility Analyzer (DMA, TSI, Shoreview, Minnesota), and condensation particle counter (CPC) were used in tandem to determine the mass of a BC particle with an aerodynamic diameter (D_{ae}) of 200 nm and 300 nm (Figure 1). The AAC was set to the selected D_{ae} while the Scanning Mobility Particle Sizer (SMPS) was used downstream for monitoring aerosol mobility size distribution. The air flow through the system was maintained at 0.30 standard liters per minute (slpm) by the CPC; the DMA sheath flow was set at 3 slpm. The resolution of the AAC was set to 10 throughout the entire experiment. Each experiment has three replicates. The geometric mean mobility diameter from the mobility size distribution was used to calculate the particle mass in the series of equations given in Tavakoli et al. 2014.[59]

An aerosol flow was sent through the AAC to produce a steady air flow containing particles of specific aerodynamic diameter. The sheath flows were approximately 6.17 slpm and 6.72 slpm with the speeds set to 338 rad/sec and 236 rad/sec for 200 nm and 300 nm particles, respectively. After passing through the AAC, the particles then entered the Aethalometer (flow ~2 slpm) and a CPC (~1.5 slpm) in parallel for mass concentration testing of 200 nm and 300 nm BC D_{ae}-selected particles. The manufacturer of the CPC quotes an uncertainty of ±10%. All flows were monitored with a Defender 220 series calibrator (DryCal, Mesa Laboratories, Butler, NJ) with an accuracy of ±1%. Background on the theory of the AAC and calculations regarding particle mass and results for the 300 nm particles are given in the Appendix B and Yao et al. 2020.[58]

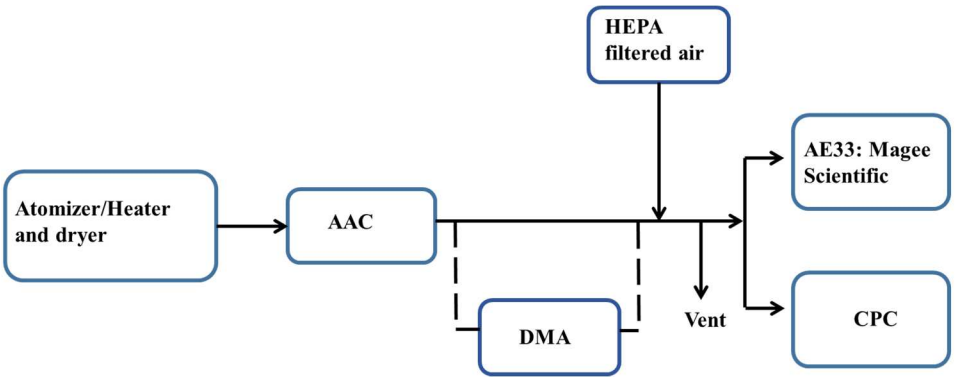

Figure 4.1 *Schematic diagram of the experimental setup for comparisons between the AE33 and the CPC. Aerosols were generated through liquid atomization and conditioned by a heater (100 °C) and diffusion dryer. The AAC generated monodisperse aerosol with aerodynamic diameters of 200 nm and 300 nm. The condensation particle counter (CPC) measured aerosol number density, while the AE33 measured BC equivalent mass concentration at multiple wavelengths. The*

DMA (component of SMPS) was used in tandem with the AAC for particle mass determination.

4.2.2 Ambient Measurements in the NYC Area

Aircraft observations were performed to understand emission and the complex chemistry of air pollutants in the NYC metropolitan area and greater Long Island Sound region. The LISTOS field campaign is a multi-agency investigation to understand the sources, photochemistry, and meteorology that impact trace gases and harmful PM. Flights were conducted on forecasted ozone events during July and August 2018, and July 2019. This paper will focus on the nine days of flights in the NYC metropolitan and Long Island area. Multiple horizontal transects and vertical profiles were flown upwind and downwind of NYC. Altitude profiles were performed above water and land to understand boundary layer behavior. The surface temperatures for all flights were over 26ºC with very little precipitation.

Well characterized instruments were used on these research flights. Concentrations of CO, as well as CH_4, CO_2, and H_2O were measured with a Picarro cavity ring down (CRD) analyzer (Model G2401-m, Picarro Inc., Santa Clara, CA). Other trace gas analyzers were also installed on the aircraft; see Wu et al. (in press) and Ren et al. (2019) for details. BC mass concentrations were measured using the filter-based instrument Aethalometer (Model AE33, Magee Scientific), the same Aethalometer model characterized in the lab, but with a flow rate of ~7 slpm.

Simultaneous, continuous measurements of BC and CO were carried out at the Queens near road site with the coordinates of 40.739264° (latitude), -73.817694° (longitude). This roadside site is located 30 m from the Long Island Expressway

(LIE, I-495). Data presented in this manuscript are from 1 June 2018 thru 31 August 2018 and 1 June 2019 thru 31 August 2019. At different periods, a TAPI model T300EU analyzer or a Thermo 48i-TLE analyzer was used to measure CO concentrations. These instruments operate on the method of non-dispersive infrared (NDIR) detection. A beam of IR radiation passes through a spinning wheel that has two chambers. One of these chambers has non-absorbing N_2 gas, while the other has a high concentration of CO e.g., Dickerson and Delany (1988).[126] The signal ratios of the two chambers are taken and ambient temperature and pressure are compensated for in order to determine the amount of CO.[92] BC is also measured at the ground site through optical absorption with an AE33 model Aethalometer. $PM_{2.5}$ particles were selected using a BGI model SCC1.829 sharp cut cyclone at 5 LPM.[127]

4.2.3 Model Inventories

The NEI is a detailed estimate of air emissions of criteria pollutants in the U.S..[118, 119] Annual emissions of EC and CO are reported publicly at a county-level basis and by sector (https://www.epa.gov/air-emissions-inventories/2017-national-emissions-inventory-nei-data). Sectors within the categories of mobile, fuel combustion, and commercial cooking were used in this calculation. The listed sectors are provided in Appendix B. The counties include Bergen, Hudson, Union, Middlesex, Monmouth, and Essex counties in New Jersey. The NY counties included in these calculations are Manhattan, Bronx, Queens, Kings, Richmond, Nassau, and Suffolk. EDGAR provides past and present "bottom up" global emissions of different air pollutants and greenhouse gases on a spatial grid (0.1° x 0.1°).[120, 121] Data used in this manuscript can be found at the EDGARv5.0 air pollutant website:

https://edgar.jrc.ec.europa.eu/overview.php?v=50_AP.[128] FIVE is a gridded mobile source inventory (4 km x 4 km) that estimates on-road and off-road activity using reported state-level fuel sales, and downscales on-road emissions using traffic count datasets. Off-road emissions are spatially and temporally allocated using surrogates from the NEI. On-road emission factors of BC and CO (in g/kg fuel) have been characterized previously,[114, 123] and updated here to more recent years based on more recent roadside measurements of vehicular exhaust.[125] More recent measurements account for the increased utilization of diesel particle filters (DPFs) on heavy-duty trucks. Off-road diesel emission factors are taken from the EPA MOVES model (https://19january2017snapshot.epa.gov/moves/moves2014a-latest-version-motor-vehicle-emission-simulator-moves_.html.). Here, we present total BC and CO emissions for an entire day, and emissions during the daytime (7:00 am to 7:00 pm EDT). The FIVE mobile source inventory is publicly available from the NOAA Chemical Sciences Laboratory, including for 2019 and 2020 at: https://csl.noaa.gov/groups/csl7/measurements/2020covid-aqs/emissions.php. All other point and area source emissions are taken from the NEI 2017 and combined with the FIVE mobile source inventory. The BC/CO ratios are compared to ambient ratios, and other inventories.

4.3 Results and Discussion

4.3.1 Calibration and characterization with 200 nm BC particles

The BC surrogate evaluated the response of the dual spot Aethalometer, AE33 model. The BC mass concentrations (M_{BC}) measured by the Aethalometer were

compared to the mass concentration determined by the AAC and a CPC ($M_{AAC-CPC}$). The data presented here for the Aethalometer is at λ=880 nm, using the default parameters for the mass absorption cross section. The mass concentration range tested in this study is 0 μg m^{-3} to approximately 12 μg m^{-3}. Data presented in Figure 4.2 is the average mass concentration of the entire run, and the error bars represent ±1σ. Within this range, the linear regression of M_{BC} versus $M_{AAC-CPC}$ at λ= 880 nm exhibited a slope of 0.997± 0.056 showing that the commercially available, filter-based instrument agrees linearly with the in situ reference method. The root mean squared error (RMSE) was approximately 8%. The total M_{BC} uncertainty is 13% when taking into account the additional uncertainty of the CPC (10%) and adding the RMSE in quadrature. Included in this regression is the zero value from the blank run of HEPA-filtered air measured with the CPC and the AE33. The characterization of 300 nm sized particles is similar and given in Appendix B.

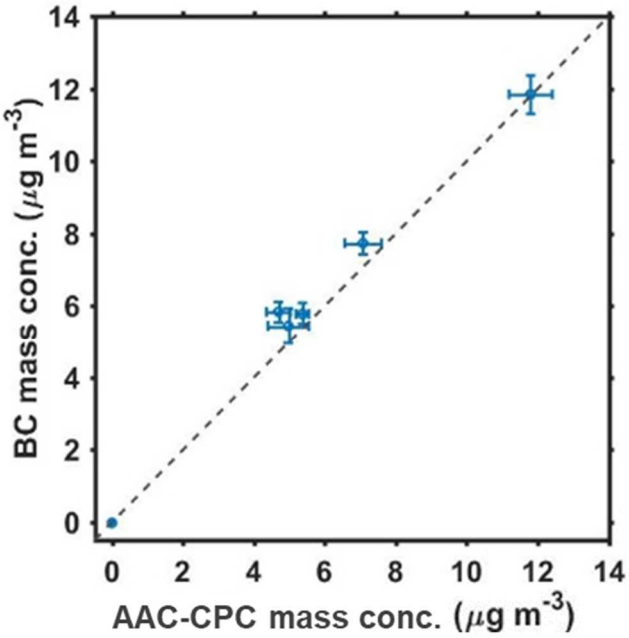

Figure 4.2 *Correlation of AAC-CPC mass concentration with the Aethalometer BC mass concentration (λ=880 nm). Particles had an aerodynamic diameter of 200 nm. Data points are averages of the entire run, and the error bars are 1σ. The dashed line shows 1:1. The root mean squared error is 0.48 μg* m^{-3}*, or approximately 8%.*

4.3.2 Wavelength dependence of the Aethalometer

The wavelength response of the filter-based instrument was evaluated for particles possessing aerodynamic diameters of 200 nm and 300 nm. Results of wavelength dependence for the 300 nm particles are given in Appendix B. The AE33 model operates at seven wavelengths, from 370 nm to 950 nm, to gather information about the presence of BC, brown carbon (BrC), and other light absorbing aerosols in the atmosphere. BC is widely believed to have an Absorption Ångström Exponent (AAE) near unity, but there are uncertainties associated with that value. It is expected that the mass concentrations are the same across all the wavelengths for BC particles in the absence of other light absorbing particles. We observe a small wavelength dependence that varies with particle size.

Figure 4.3 shows the multi-wavelength response of the Aethalometer to 200 nm particles with an average BC mass concentration (as indicated by the Aethalometer at λ=880 nm) of 5.79 μg m^{-3}. Mass concentrations reported at the seven different wavelengths are derived from different MAC values. During this 45 min run, the average BC equivalent mass concentration for this BC surrogate was lowest at 370 nm (9% lower than the value at 880 nm and slightly outside the combined standard deviations). We observed a similar phenomenon for 300 nm sized particles,

but to a different magnitude at the lower wavelengths (see Appendix B). The equivalent BC mass concentration value at λ=370 nm reads 31% less than the BC mass concentration value at λ=880 nm. However, the mass concentration remained constant within uncertainty between 470 and 950 nm. The reported mass concentration at λ=950 nm is slightly higher (2%) than the value at λ = 880 nm.

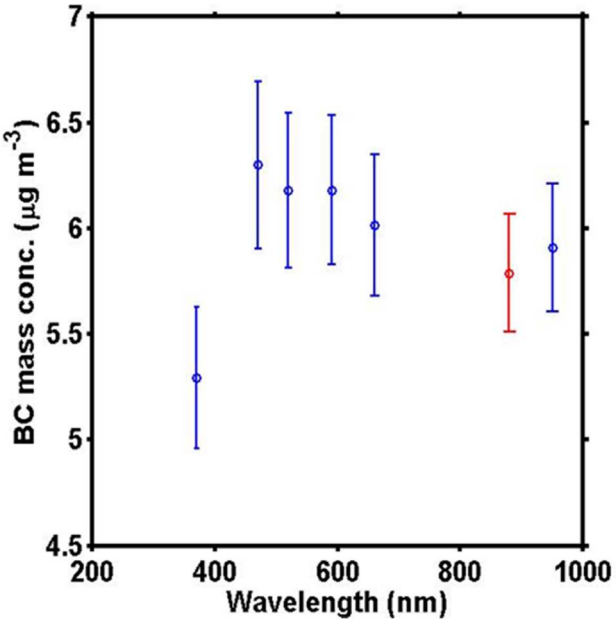

Figure 4.3 *Wavelength response to 200 nm particles during one 45-minute run at 7 different wavelengths. All error bars are 1σ. The red data point is representative of BC measured at 880 nm.*

The wavelength response profiles vary with particle size and this could aid in ambient particulate matter size determination. For these 200 nm sized particles, the BC equivalent mass concentrations at λ=370 nm was 9% lower than the mass concentration values at λ=880 nm. BrC and most mineral dust particles show greater absorption at shorter wavelengths. A similar Aethalometer (Model AE31) indicated an Attenuation Angstrom Exponent, A_tAE, value reasonably near unity (0.71) for the

pure BC surrogate, but much larger (3.7) for a BrC surrogate (Grimes et al., 2020, in press). Retrieving spectral data from the AE33 BC measurements may help approximate aerosol composition and size. Deviations significantly greater than 10% suggest the presence of particles other than BC such as BrC.

4.3.3 BC and CO concentrations in the NYC metropolitan region during LISTOS Flights

The LISTOS airborne campaign was conducted during the summers of 2018 and 2019. During the days of the flight campaign, the Cessna research aircraft flew spirals and east-west transects across the NYC metropolitan area. All nine days of flights are presented here for analysis, and the flight paths are shown below in Figures 4.4a and 4.4b for summer flights in 2018 and 2019, respectively. BC measurements were acquired with the calibrated AE33, as mentioned above.

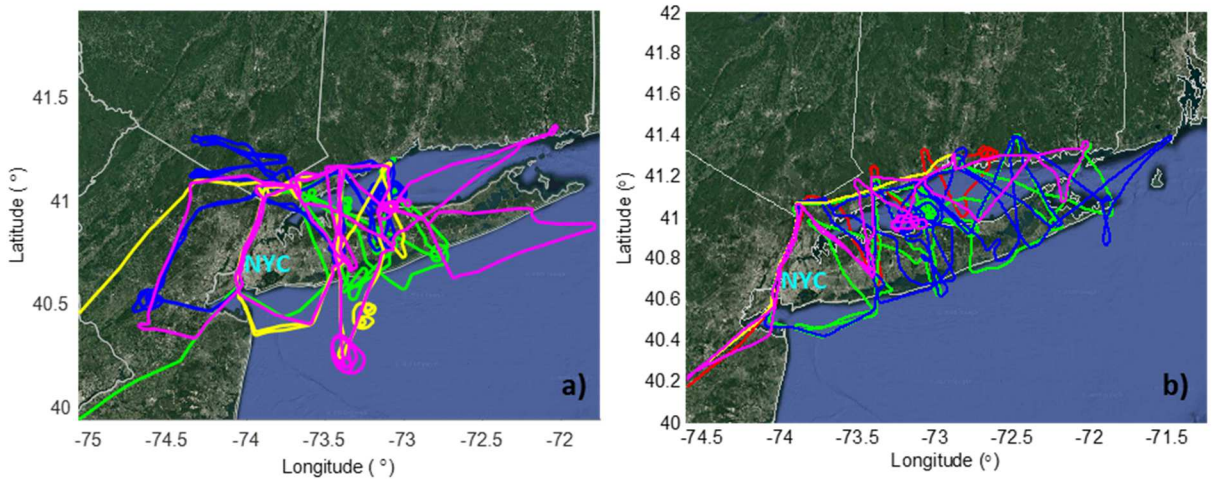

Figure 4.3 *a) Flight tracks for the LISTOS flight campaign in 2018. Green is 1 July 2018, blue is 2 July 2018, yellow is 15 August 2018 and magenta is 16 August 2018*

(b) Flight tracks for the LISTOS flight campaign in 2019. Red is 19 June 2019, green is 20 June 2019, blue is 21 June 2019, yellow is 22 June 2019 and magenta is 29 June 2019.

During the LISTOS flight campaign, the aircraft did multiple spirals down to approximately 200 m above the Earth's surface to obtain profiles of trace gases and aerosols. Transects were also performed to understand the evolution of polluted air masses downwind of the NYC metropolitan area. Within the PBL at altitudes between 0.1 km and 1 km (the approximate top of the PBL) BC and CO were well correlated (Table 4.1) with an average r^2 of 0.65. BC mass concentrations were highest above Manhattan, the I-95 corridor, and downwind of NYC onto Long Island. The minimum flight-averaged BC mass concentration was 0.391 ± 0.141 μg m^{-3} (21 July 2019) and the maximum average value was 1.30 ± 0.46 μg m^{-3} (19 July 2019). All data was averaged to 1 minute.

Table 4.1 Measured BC and CO data from the LISTOS flights. The linear least-squares regression fits are from the BC/CO correlations. The CO concentrations are plotted as the independent variable and the BC mass concentrations are the dependent variable (see Figure 4.5)

Day of Flight	Mean [CO] ±1σ (ppbv)	Mean [BC] ±1σ (μg m^{-3})	Linear regression fit (slope: ng m^{-3} ppb^{-1})	R^2
1 July 2018 (Sunday)	191.5 ±44.2	0.59 ±0.21	[BC]=4.04[CO] -0.197	0.72
2 July 2018 (Monday)	251.6 ±60.1	1.025 ± 0.488	[BC]=7.34[CO] -0.847	0.77
15 August 2018 (Wednesday)	190.5 ±12.6	0.702 ±0.118	[BC]=6.00[CO] -0.432	0.37
16 August 2018 (Thursday)	206.9 ±22.3	0.947 ±0.274	[BC]=7.76[CO] -0.656	0.41
19 July 2019 (Friday)	254.8 ±48.6	1.300 ±0.456	[BC]=8.76[CO] -0.938	0.86

20 July 2019 (Saturday)	151.6 ±31.6	0.459±0.176	[BC]=4.21[CO] -0.205	0.57
21 July 2019 (Sunday)	150.1 ± 24.8	0.391 ±0.141	[BC]=4.31[CO] -0.257	0.57
22 July 2019 (Monday)	141.5 ±35.2	0.549± 0.254	[BC]=6.73[CO] -0.440	0.79
29 July 2019 (Monday)	220.6 ±26.1	0.810±0.270	[BC]=9.36[CO] -1.256	0.82

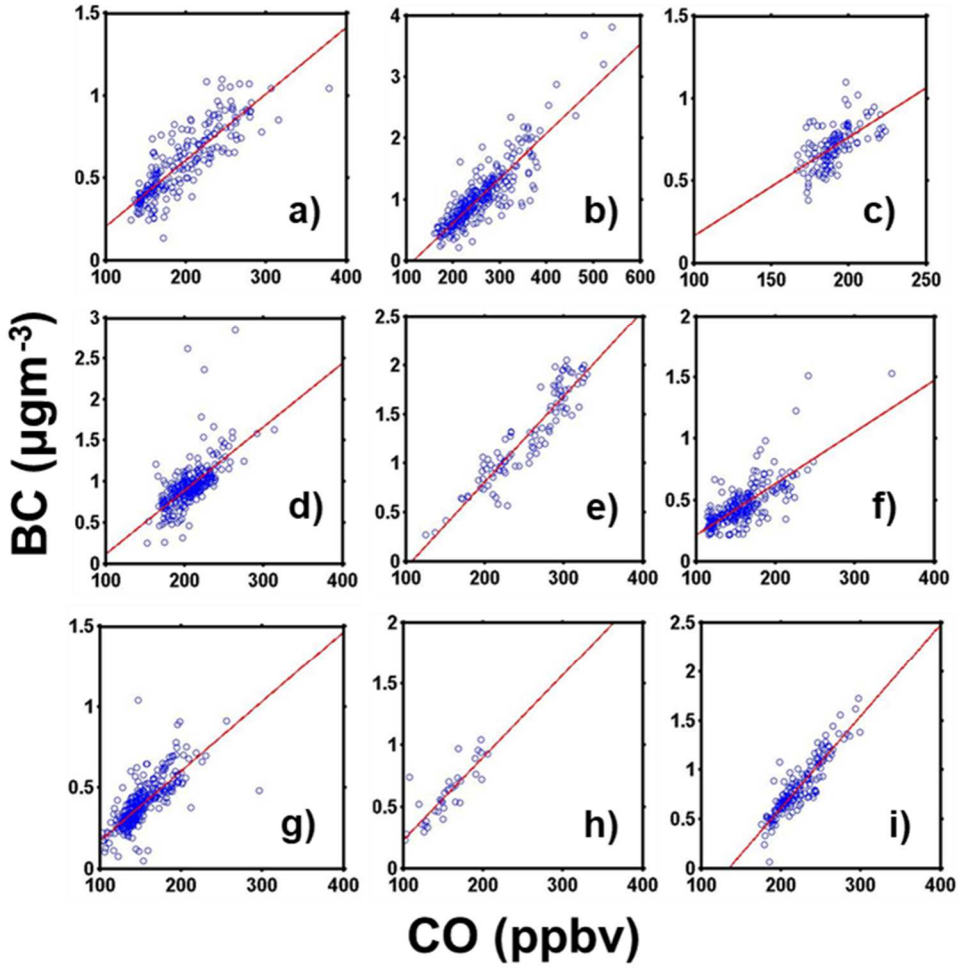

Figure 4.1 *Correlations of BC mass concentration (y-axis) and CO mixing ratio (x-axis) for each flight during the LISTOS campaign. Circles are 1-minute averaged data below 1000 m. (a) 1 July 2018 (Sunday); (b) 2 July 2018 (Monday); (c) 15 August 2018 (Wednesday); (d) 16 August 2018 (Thursday); (e) 19 July 2019 (Friday); (f) 20 July 2019 (Saturday); (g) 21 July 2019 (Sunday); (h) 22 July 2019*

(Monday); and (i) 29 July 2019 (Monday). The average weekend ΔBC/ΔCO ratio is 4.19 ± 0.14 and the average weekday ratio is 7.66 ± 1.25 ng m^{-3} ppb^{-1}.

The Model AE33 measures BC at multiple wavelengths; from the UV (370 nm) to the near-IR (950 nm) wavelengths. The portion that is measured in the UV portion of the spectrum is designated as BC_{UV} and BC refers to the portion measured at 880 nm. BC_{UV} provides qualitative measurements of carbon species that absorb at this wavelength.[129, 130] An enhancement at this lower wavelength can be used to assess the impact of sources of brown carbon, and polycyclic aromatic hydrocarbons (PAHs). Some of these sources include biomass burning, tobacco smoke and fresh diesel exhaust.[131, 132] To determine the impact from UV absorbing carbon species, we plotted BC_{UV} versus BC for all nine flights within the PBL. The linear regression coefficients are provided in Table 4.2. The average slope or $\Delta BC_{UV}/\Delta BC$ is 0.92 ±0.12, and this indicates little influence from biomass burning within the NYC region. The average value falls within the range of fossil fuel emissions presented in previous studies of source apportionment.[129] In this work, we report BC from the 880 nm channel.

Table 4.4 *Linear regression fits for BC equivalent mass concentrations at 370nm (BC_{UV}, dependent variable) vs. BC mass concentrations at 880 nm (independent variable).*

Day of Flight	Linear Regression Coefficients	R^2
1 July 2018 (Sunday)	$[BC_{UV}]=0.90[BC]+74$	0.87
2 July 2018 (Monday)	$[BC_{UV}]=0.84[BC]+126$	0.95
15 August 2018 (Wednesday)	$[BC_{UV}]=0.84[BC]+104$	0.63
16 August 2018 (Thursday)	$[BC_{UV}]=0.73[BC]+266$	0.66
19 July 2019 (Friday)	$[BC_{UV}]=0.94[BC]+48$	0.98

20 July 2019 (Saturday)	$[BC_{UV}]=1.05[BC]+22$	0.93
21 July 2019 (Sunday)	$[BC_{UV}]=1.08[BC]+13$	0.90
22 July 2019 (Monday)	$[BC_{UV}]=1.04[BC]+52$	0.98
29 July 2019 (Monday)	$[BC_{UV}]=0.87[BC]+101$	0.89

BC and CO are strongly correlated because they share common or co-located sources.[110, 112, 115, 133, 134] Both are products of incomplete combustion[104, 135] and the emission ratios of ΔBC/ΔCO vary according to combustion sources, fraction of source mix, age, and condition of the vehicle fleet. Typically, the higher the ΔBC/ΔCO ratio, the more likely diesel engines are the prominent source. CO is primarily emitted from both on-road and off-road gasoline-fueled engines[124] while BC is primarily emitted from on-road and off-road diesel engines.[114, 136] As shown in Dickerson et al. (2002)[18], BC emissions can be estimated based on CO inventories and ΔBC/ΔCO ratios[17]. In this study, data acquired between altitudes 100 m and ~1000 m were selected because the air was recently impacted by emissions. As depicted in Figures 4.6a and 4.6b below, the BC mass concentrations measured with the well characterized AE33, were strongly correlated with CO during all days except 15 and 16 of August 2018. The relatively high correlations indicate a common source or collocated source. All regression coefficients and R^2 values are provided in Table 4.1 and were shown in Figure 4.5. The ΔBC/ΔCO ratios calculated on multiple Saturdays and Sundays are representative of the weekend, and the ΔBC/ΔCO ratios calculated on Monday through Friday are representative of weekdays.

A prominent weekday and weekend pattern was observed. The average ΔBC/ΔCO ratio for the weekdays was 0.00761 μg m^{-3} ppb^{-1} (6.65 gBC/kgCO at standard temperature of 25°C and pressure of 1 atm, or STP) while the average for the

weekend was 0.00419 μg m^{-3} ppb^{-1} (3.66 gBC/kgCO at STP). Based on the summer flight data, the weighted average of a typical week was 0.00663 μg m^{-3} ppb^{-1} ΔBC/ΔCO (5.79 gBC/kgCO). These values are comparable to measurements taken by roadside and urban sites in Mexico,[135, 137] Beijing, China [136] and Fort Meade, Maryland.[110]

4.3.4 Measured BC and CO at the Near Road (NR) site in Queens, Summers 2018 and 2019

Continuous measurements of BC and CO were taken at a near-road site in Queens, NY. Data was recorded every hour, and the correlations of BC and CO for each summer were determined. Average concentrations, the standard deviations, standard deviations of the mean, maximum and minimum values of 1 hr averages of BC and CO for summers 2018 and 2019 are tabulated in Table 4.3. Appendix B provides a similar table for 24-hour (1 day) averages of BC and CO. Average BC mass concentrations were consistently higher on weekdays than during the weekends. This was not observed for CO. BC and CO maximum hourly concentrations consistently show higher values during the weekdays versus the weekend. The weekend and weekday relationships of ΔBC/ΔCO ratios were also compared. The weekday correlations for both years showed a higher ΔBC/ΔCO ratio in comparison to the weekend correlations and is consistent with findings from the 2010 CalNex (California Research at the Nexus of Air Quality and Climate Change) field study.[138] This is further supported by the traffic count data presented below. Figure 4.7 presents these differences in correlations of BC and CO for summers 2018 and 2019

in Queens, NYC. During the summer of 2018, weekday ratio is approximately 63% higher than observed on the weekend. The weekday ratios for the summer of 2019 were approximately double that of the weekend ratio. The weighted average ΔBC/ΔCO ratios for summers 2018 and 2019 were 0.00606 μg m^{-3} ppb^{-1} (5.29 gBC/kgCO) and 0.00483 μg m^{-3} ppb^{-1} (4.22 gBC/kgCO), respectively.

Table 4.5 *The average, standard deviation (STD, 1σ), standard deviation of the mean, maximum and minimum values for 1-hour averages of BC and CO concentrations. All values are from the Queens NR site during the summers of 2018 and 2019.*

		2018					2019				
		AVG	STD	STD of mean	MAX	MIN	AVG	STD	STD of mean	MAX	MIN
BC (μgm^{-3})	weekday	1.14	0.91	0.16	7.08	0.07	1.19	0.82	0.14	5.032	0.04
	weekend	0.84	0.63	0.12	5.01	0.09	0.60	0.37	0.07	3.559	0.08
CO (ppb)	weekday	262.8	109.1	19.02	879.4	84.7	308.2	103.8	18.1	815.9	126.7
	weekend	290.8	112.1	21.86	736.7	90.6	275.5	80.8	15.8	732.3	143.8

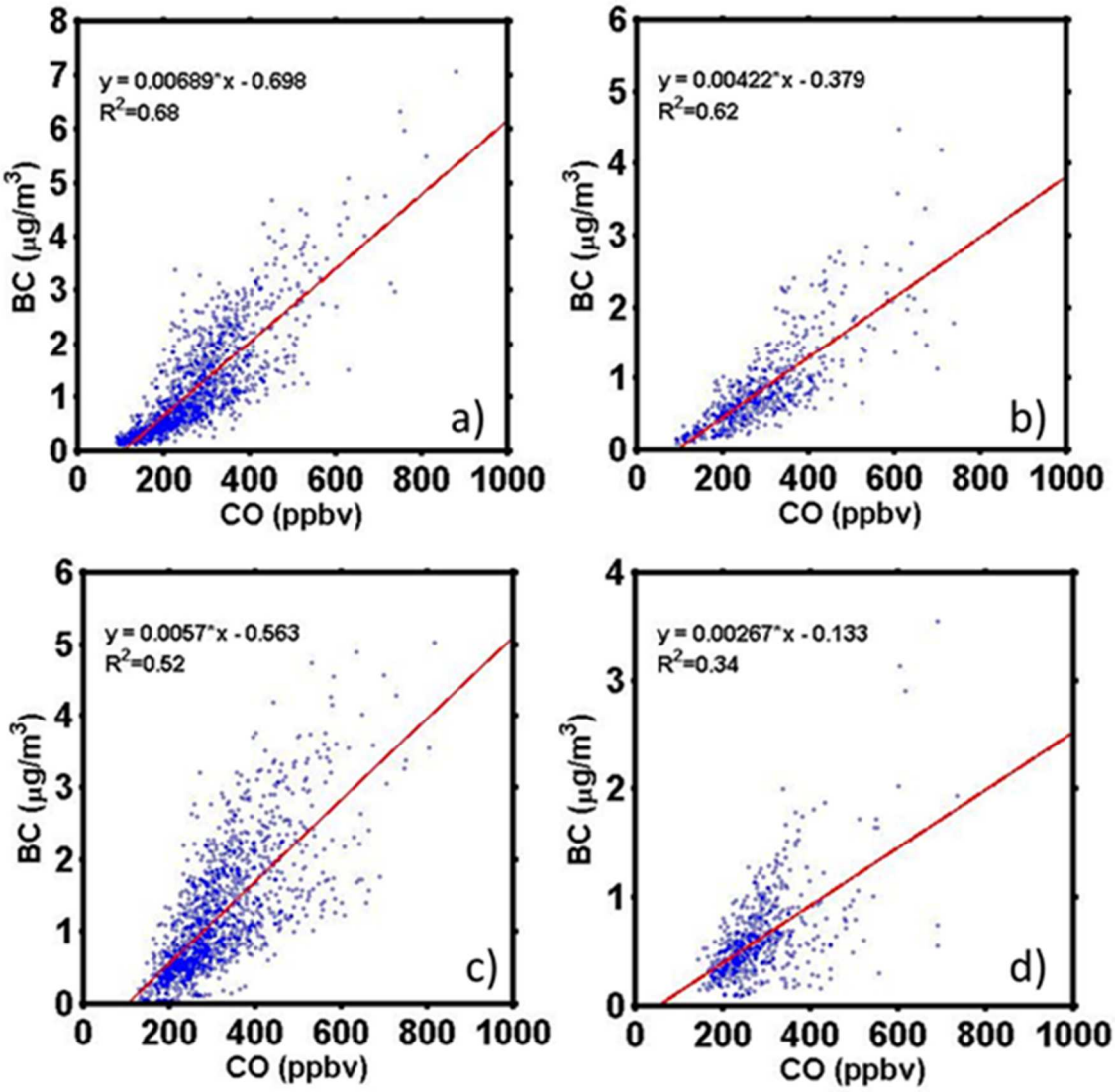

Figure 4.1 *Relationships between BC and CO for summers 2018 and 2019. Blue circles are 1-hour averaged data. (a) Weekday data for summer 2018 (b) Weekend data for summer 2018 (c) Weekday data for summer 2019 (d) Weekend data for summer 2019. The weighted average slope was 0.00606 µg m-3 ppb-1 (5.29 gBC/kgCO) for 2018 and 0.00483 µg m-3 ppb-1 (4.22 gBC/kgCO) for 2019. The average of both years is 4.76 gBC/kgCO.*

The ΔBC/ΔCO ratio is used to indicate the fraction of diesel vehicles compared to spark ignited engines. A higher ΔBC/ΔCO ratio is the result of a higher

fraction of heavy-duty diesel vehicles (HDDVs) on the road. The higher ΔBC/ΔCO slopes measured on the weekdays indicates a larger contribution of diesel vehicles within that particular region of the NYC metropolitan area. Truck traffic is substantially higher during the weekdays than on the weekend (Figure 4.7). The New York State Department of Transportation Highway Data Services* (NYSDOT HDS) recorded the number of vehicles on the road per hour on the Long Island Expressway (LIE), and sorted them by car traffic and truck traffic (see caveat in acknowledgments). The LIE (I-495) stretches approximately 110 km (70 miles) from the Queens-midtown tunnel to Riverhead in Suffolk County. Traffic counts show the LIE has nearly three times the truck traffic on average during the weekday versus the weekend; daily total car traffic is indistinguishable from the weekday to weekend. For the summer 2018, the average total weekday counts for cars were 75,199 while the weekend was approximately 8% higher at 81,141 cars. Weekdays had an average of 4,885 trucks on the expressway, while the weekend number dropped to an average of 1,752 trucks per day. These traffic statistics from NYSDOT further confirm the reasoning behind the higher ΔBC/ΔCO ratios observed on the weekdays than on the weekends. The higher number of trucks on the road generates higher ΔBC/ΔCO ratios. Figure 4.7 below shows the difference in number of trucks and cars for both the weekdays and weekend.

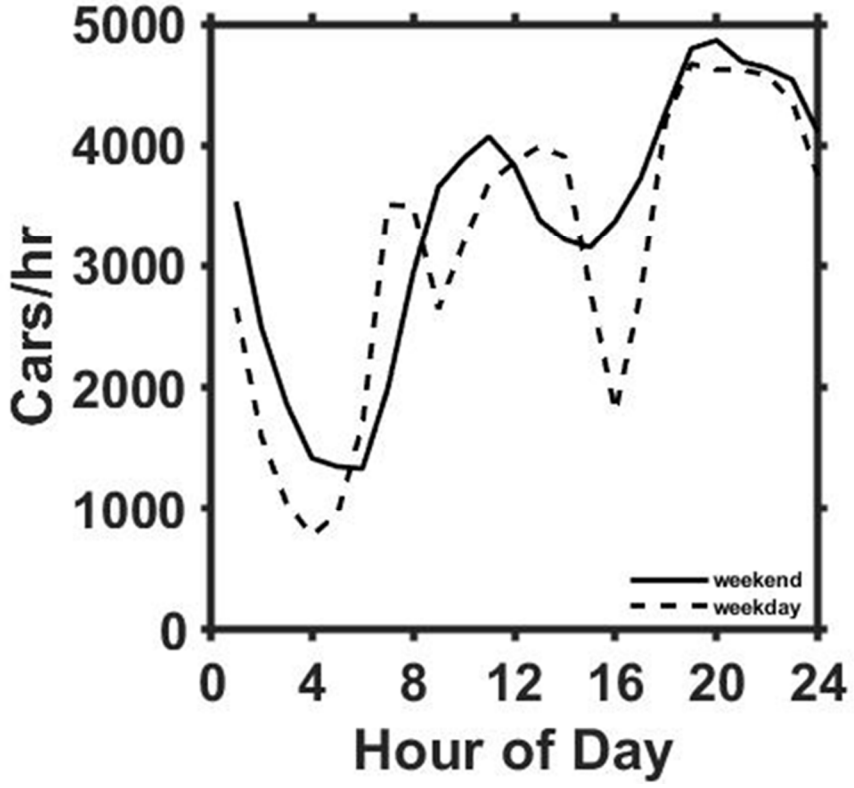
5000
4000
3000
2000
1000
0
Cars/hr
0
4
8
12
16
20
24
Hour of Day
weekend
weekday

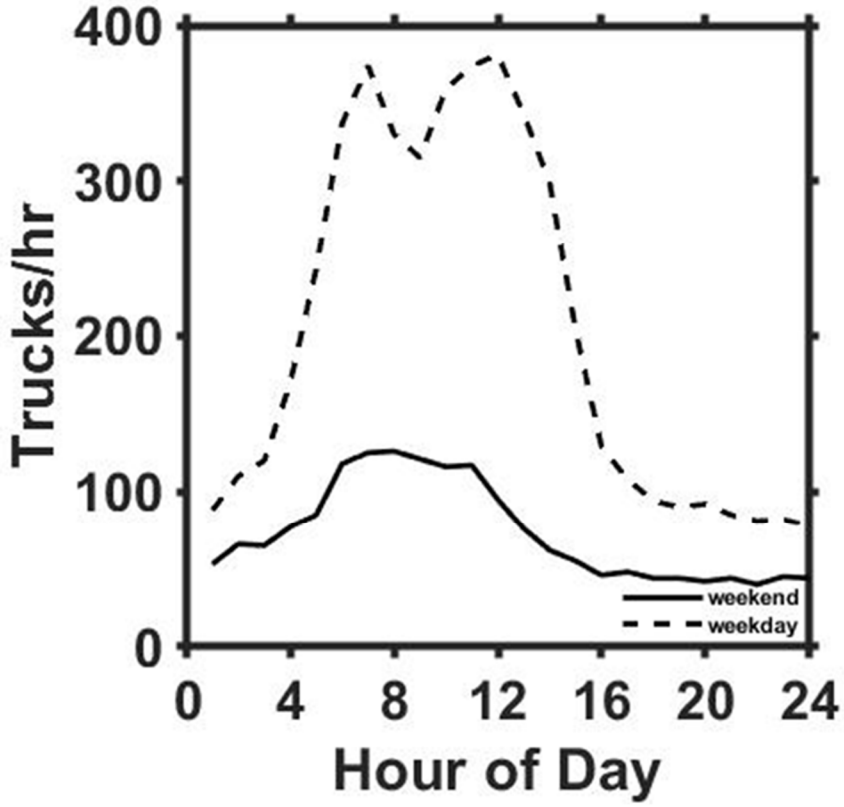
400
300
200
100
0
Trucks/hr
0
4
8
12
16
20
24
Hour of Day
weekend
weekday

Figure 4.2 *(a) Counts of cars on the Long Island Expressway (LIE) during weekdays and the weekend. (b) Counts of trucks on the LIE during the weekdays and weekends (NYSDOT).*

4.3.5 Emission values for BC and CO in the NYC metropolitan area

The E_{CO} from the 2017 NEI data for the NYC metropolitan area encompassing counties in New York, and New Jersey is approximately 0.713 Tg (713 Gg) of CO per year. E_{CO} of mobile, commercial cooking and fuel combustion sectors were provided for each of the listed counties in their respective state. The value presented here represents the total E_{CO} for the listed counties. Therefore, the average E_{BC} in the NYC metropolitan area is estimated at 0.713 x (0.00582) = 0.00415 Tg yr^{-1} (4.15 Gg yr^{-1}) of BC (or $4.56x10^3$ tons per year) based upon measured aircraft ratios, and the NEI E_{CO}. This total emission value of BC is approximately 9% and 28% lower when using the Queens near road $\Delta BC/\Delta CO$ ratios for summers 2018 and 2019, respectively. NEI also reports emission values for elemental carbon (EC), per county and per sector. In this work, 2017 NEI EC emission (E_{EC}) values are used interchangeably as BC. We calculated E_{EC} the same way as CO by using the exact same sectors. For the NYC metropolitan area, estimated E_{EC} totaled $3.03x10^3$ short tons per year or 0.00275 Tg per year (2.75 Gg yr^{-1}). This value is approximately 38% lower than the E_{BC} value utilizing NEI E_{CO} and flight $\Delta BC/\Delta CO$ ratios.

In this work we used FIVE 2019 to model the emissions of BC and CO within the metropolitan region of NYC. Mobile source emissions are taken from FIVE and all other point and area-wide sectors are from NEI 2017. Values of CO emissions from FIVE 2019 are lower than the NEI 2017 by ~30%, as seen in Table 4. The $\Delta BC/\Delta CO$

ratio from the summer flights was ~11% higher than the FIVE BC/CO ratio for the entire day, and ~30% higher than the ratio from the FIVE daytime hours. However, the ΔBC/ΔCO ratio from the summer 2019 Queens near-road site was nearly 19% lower than the ratio for the entire day of FIVE. The total E_{BC} value from FIVE is ~10% lower than the total emissions calculated from the 2018-2019 summer research flights conducted over the NYC region, and ~10% higher than the calculated average E_{BC} from the Queens near road site for years 2018 and 2019. Maps of the total emissions within the region studied can be found in Appendix B (Figure B3).

EDGAR emission rates were calculated for both BC and CO for the NYC metropolitan area latitudes and longitudes were adjusted to include each county mentioned previously. For the year 2015, E_{BC} was 3.82×10^3 short tons per year (0.00346 Tg yr^{-1} or 3.46 Gg yr^{-1}) while E_{CO} was 5.02×10^5 short tons per year (0.455 Tg yr^{-1} or 455 Gg yr^{-1}). Thus, the mass ratio of BC to CO for 2015 was 0.00760 and is ~31% higher to the weighted weekly emission ratio average calculated in NYC from aircraft measurements in both 2018 and 2019. The total E_{BC} value from EDGAR is ~ 31% higher than the total BC emissions calculated from the 2018-2019 summer research flights conducted over the NYC region. Seasonal variability may be a factor in the difference. Due to the coarseness of the grid of this global model, EDGAR's E_{CO} value was excluded from the average E_{CO}, and from the calculation of E_{BC} in the NYC region.

The uncertainty of BC measurements from the Aethalometer is ~±13% (1σ) and for CO from CRD measurements ~±2%[139] and ±10% for NDIR.[126] Weekday ΔBC/ΔCO ratios from the Cessna have an uncertainty of ~±16% and ~±3% for the weekend.

When added in quadrature, the total weighted uncertainty in the ΔBC/ΔCO ratio of a typical week is ~±11%. Using the standard errors of the slopes for the weekday and weekend and adding them in quadrature, the weighted uncertainty of the 2018 summer ΔBC/ΔCO ratio at the Queens NR site is ~±3%. This number is slightly lower at ±2% for summer 2019. The average E_{CO} from the two inventories (full day) is ~646 Gg yr^{-1} with a ±1σ CI of 169 Gg yr^{-1}. Thus, the 1σ uncertainty in E_{CO} (ignoring the CO from VOC oxidation) is ±26%. If CO from oxidation of isoprene or other VOC's creates a substantial amount of CO then the ΔBC/ΔCO ratio detected from the Cessna will be lower than the emissions ratio, and ΔBC/ΔCO*E_{CO} will be lower than the actual E_{BC}. In this sense, the E_{BC} calculated from the aircraft is a lower limit. The composition of the air sampled by the near road monitors is dominated by highway emissions – VOC oxidation will have minimal impact. Other sources, such as off-road diesel and shipping will not be sensed directly. This may contribute to the lower average near road ΔBC/ΔCO value compared to the aircraft value (5.82 vs 4.76 gBC/kgCO). When considering the uncertainties of the ΔBC/ΔCO ratios from the Cessna and the Queens near-road site, the uncertainties from the BC and CO instrumentation, and the uncertainties from the CO inventories, the total uncertainty of E_{BC} for the NYC region is ±39%.

Table 4.6 *Total emission values of CO and BC (or EC for NEI) in the NYC metropolitan area. BC emission values from the Cessna aircraft and Queens NR site were calculated using the CO emissions from the bottom-up inventories (NEI and FIVE) and the ambient ΔBC/ΔCO ratios.*

Inventory	E_{CO} (Gg yr^{-1})	E_{BC} (Gg yr^{-1})	Inventory BC/CO (g/kg)	E_{BC} Cessna (Gg yr^{-1})	E_{BC} 2018 Queens (Gg yr^{-1})	E_{BC} 2019 Queens (Gg yr^{-1})
NEI (2017)	766	2.75	3.59	4.46	4.05	3.23
FIVE (2019)	526	2.74	5.21	3.06	2.78	2.22
FIVE (2019 daytime)	415	1.85	4.46	2.42	2.20	1.75

4.4 Conclusions

A Model AE33 Aethalometer was evaluated and calibrated using a well-characterized BC surrogate. For nearly pure BC, the Aethalometer responded linearly and with good accuracy (when using default settings at 880 nm), within ~13% when compared to an in-situ reference method. BC mass concentration readings were consistent within the wavelength range of 470-950 nm for aerodynamic diameters of 200 and 300 nm. This filter-based method can properly measure ambient mass concentration of BC particles and is suitable for field deployment where BC dominates aerosol absorption.

Ambient BC and CO are well correlated at the Queens near-road site and from the Cessna with a mean weighted average ΔBC/ΔCO ratio of 5.3 ± 1.1 gBC/kgCO. Observed ΔBC/ΔCO ratios were higher from the aircraft than the roadside monitor because of more sources being sampled. The E_{BC}/E_{CO} ratio of the FIVE inventory for all hours is 2% lower and the NEI inventory is 32% lower than the ambient weighted average ratio. Using the average of the observed ΔBC/ΔCO ratios from the flights and near-road site and the average E_{CO} inventory value from the two bottom-up inventories (646 ±169 Gg yr^{-1}CO), we calculate the E_{BC} to be 3.42 ± 1.33 Gg yr^{-1}, ~25% higher than both FIVE's all hours inventory and NEI's inventory. If ambient

CO concentrations are inflated by substantial VOC oxidation, then the E_{BC} inferred from the BC/CO ratio would be even higher. The weekday weekend difference in E_{BC} supports the contention that diesel vehicles are the dominant source. Higher emissions of BC lead to greater ailments, especially in neighborhoods near heavy diesel sources, and this leads to concerns of environmental justice.

From this study, we were able to characterize the total BC emissions, and the uncertainty, within the NYC geographical area. This method may prove useful to other urban regions struggling with high concentrations of BC. Emission estimates of BC in Beijing were 11.9 Gg in 2012,[140] and 4.86 Gg in 2006 over New Delhi, India,[141] although these cities experience much greater PM loads than does NYC. Direct in situ measurements, as shown in this work, are greatly needed to identify sources and to reduce the uncertainty of global BC emission estimates. Future work should include ambient mass balance experiments to evaluate CO emission inventories, and seasonal variability studies of BC and CO measurements.

Chapter 5: Strong light absorption by atmospheric particles in the planetary boundary layer over Hebei, China derived from aircraft observations

5.1 Introduction

Black carbon (BC) is a light absorbing aerosol created by the incomplete combustion of carbonaceous aerosol. It is believed to be a leading cause of global warming and is known to reduce cloud albedo.[142] High BC concentrations are known to impact human health by contributing to an increased level of cardiovascular and respiratory ailments.[143] BC particles are usually mixed with small amounts of non-refractory materials when freshly emitted[144] and usually accumulate more layers of coating during their atmospheric lifetimes. BC can also adhere to the outside of minerals enhancing the absorptive properties of the aerosol.

Among the many different techniques used to measure ambient light absorbing aerosols is the measurement of optical attenuation of light through a filter where particles are continuously collected. This is commonly called the integrating plate technique and is prone to artifacts. One of the filter-based instruments used to measure light absorption is the particle soot absorption photometer (PSAP, Radiance Research). The single particle soot photometer (SP2, Droplet Measurement) is based on the principle of laser incandescence, another technique used to measure BC (mass concentration) based on refractory properties. This is a more direct measurement and quantifies the mass of individual BC particles.

The mass absorption cross section (MAC, m^2g^{-1}) is defined by the ratio of the absorption coefficient (m^{-1}) to the mass concentration ($g\ m^{-3}$) of light absorbing

aerosols. Bond and Bergstrom (2007) reported a MAC value of 7.5 ±1.2 $m^2 g^{-1}$ for fresh, light-absorbing carbon. MAC value may decrease as particles aggregate, coagulate, bleach, or collapse. However, as particles age and accumulate a coating, the MAC may increase and cause an absorption enhancement. Cui et al. (2016) reported an enhancement of the MAC value by a factor of 2, when mixing BC with sulfate,[145] and Jacobson et al. (2000) used climate models to predict an enhancement by a factor of 2 when BC is coated with non-absorbing materials.[31] Liousse et al. (1993) reported a MAC range of 5-20 $m^2 g^{-1}$ and attributed the variability to aerosol mixing and particle age.[146] Urban aerosol from Atlanta, Georgia, MAC values ranged from 5.3-18.2 $m^2 g^{-1}$, and this variability was attributed to differences in aerosol properties, differences in the mass concentration techniques and uncertainties in the measurement of light absorption.[147] Table 5.1 presents the MAC values from a variety of previous studies and their respective measurement techniques.[148]

Table 5.1 *Experimental studies determining the MAC of BC. Taken from Nordmann et al. (2013).*

Site	Type	Author	Absorption Measurement	Carbon Measurement	Mass Absorption Cross Sections ($m^2\ g^{-1}$)
Jungfraujoch, Switzerland	mountain	*Cozic et al.* [2008]	MAAP (637 nm)	EC/OC[a]	7.4–11.1
Manora Peak, India	mountain	*Ram et al.* [2010]	optical attenuation (687 nm)	EC/OC[a]	11.6–14.5
Maledives (aircraft)		*Mayol-Bracero et al.* [2002]	PSAP (550 nm)	EC/OC[b]	8.1
Manaus, Brazil	regional	*Gilardoni et al.* [2011]	MAAP (637 nm)	EC/OC[c]	4.7
Guangzhou, China	regional	*Kondo et al.* [2009]	PSAP, COSMOS (565)[g]	EC/OC[a]	9.9–12.0
Yufa, China	regional	*Kondo et al.* [2009]	PSAP, COSMOS (565 nm)[g]	EC/OC[a]	11.6–15.7
Mexico City, Mexico	regional	*Doran et al.* [2007]	Photoacoustic (870 nm)	EC/OC[a]	8.5
Brighton, Colorado	regional	*Moosmüller et al.* [1998]	Photoacoustic (685 nm) (685 nm)	EC/OC[d]	3.6
Gosan, South Korea	regional	*Chuang et al.* [2003]	PSAP (550 nm)	EC/OC[a]	12.6–14.8
Finokalia, Greece	regional	*Sciare et al.* [2003]	PSAP	EC/OC[a]	7.5
kleiner Feldberg, Germany	regional	*Petzold and Schönlinner* [2004]	MAAP (637 nm)	EC/OC[e]	4.8
Tsukuba, Japan	regional	*Naoe et al.* [2009]	PSAP (565 nm)	EC/OC[d]	10–13
Berlin, Germany	urban	*Petzold and Schönlinner* [2004]	MAAP (637 nm)	EC/OC[e]	6.3
Vienna, Austria	urban	*Hitzenberger et al.* [2006]	MAAP (637 nm)	EC/OC[e]	3.9–8.4
Atlanta, USA	urban	*Carrico et al.* [2003]	PSAP (550 nm)	EC/OC[a, f]	5.3–18.3
Toronto, Canada	urban	*Knox et al.* [2009]	Photoacoustic (760 nm) (760 nm)	EC/OC[a]	6.9–9.9
Tokyo, Japan	urban	*Kondo et al.* [2009]	PSAP, COSMOS (565 nm)[g]	EC/OC[a]	6.7–15.0
Laboratory	coated flame soot	*Khalizov et al.* [2009]	extinction-scattering (532 nm)[h]	DMA/ APM	8.7–12.6
Laboratory	coated graphite	*Shiraiwa et al.* [2010]	Photoacoustic (532 nm)	SP2[i]	5.1 – 10

[a]EC/OC analyzer Sunset Laboratory, as described in *Birch and Cary* [1996].
[b]EC/OC by Evolved Gas Analysis, EGA [*Novakov et al.*, 1997].
[c]EC/OC dual optical carbonaceous analyzer (Sunset Laboratory), EUSAAR2-protocol [*Cavalli et al.*, 2010].
[d]EC/OC by thermal/optical reflectance from Desert Research Institute (DRI) [*Chow et al.*, 1993].
[e]EC/OC by a thermal method following *VDI* [1996].
[f]EC/OC by a Rupprecht and Patashnick Series 5440 ambient carbon particulate monitor.
[g]σ_{ap} at 565 nm by a Continuous Soot Monitoring System (COSMOS, Kanomax, Osaka, Japan) *Miyazaki et al.* [2008].
[h]σ_{ap} at 532 nm by nephelometer and cavity ring-down spectrometer.
[i]BC by laser-induced incandescence as described in *Gao et al.* [2007].

5.2 Materials & Methods

During the months of May and June 2016, a ground and air-based experiment was conducted in the North China Plain (NCP). This experiment was conducted to compare surface-based measurements with airborne measurements and to examine the transport of pollutants vertically and horizontally. Trace gas and aerosols were measured from a Y12 twin-engine turboprop airplane.[131, 149] Measurements were

taken in the lower atmosphere, along with ground-based in situ measurements at a supersite in Xingtai. Vertical profiles of trace gases, BC, and aerosol optical properties were obtained through ascents and descents of the airplane in the boundary layer. Airborne (0 to ~3 km altitude) measurements of BC mass concentration (measured by the SP2), and absorption coefficient (σ_{abs}; measured by the PSAP) are discussed in this manuscript. I calculate and compare MAC values for RF4 (20160517), RF5 (20160519), RF7 (20160528) and RF11 (20160611).

The Aerosol Atmosphere Boundary Layer Cloud campaign (A^2BC) took place from May to December 2016 in the Hebei Province of the NCP. This manuscript will focus on four days in the months of May and June 2016, where airborne measurements were taken. The National Science Foundation supported the Air chemistry Research In Asia (ARIAs) project. This project's goal was to integrate *in situ* measurements, satellite remote sensing and transport models for the quantification of tropospheric chemistry and composition.

An instrumented turboprop airplane (Y12) was used to measure the aerosol properties and was flown to four different locations for spirals. The locations are Luangcheng Airport (LC; 114.59° E, 37.91° N), Xingtai (XT;114.36ºE, 37.18ºN), Julu (JL; 115.02ºE, 37.22ºN) and Quzhou (QZ; 114.96ºE, 36.76ºN). All sites are located east of the Taihang Mountains. The aircraft speed was between 60 and 70 m s^{-1} and ascent/descent speeds of 2-5 ms^{-1}. Multiple instruments for gas and aerosol analysis were onboard the plane, and they were routinely calibrated for optimal performance (Wang et al. 2018, Benish et al 2020; [150]).

The particle soot absorption photometer (PSAP, Radiance Research, 565 nm) is a filter-based instrument used for measurements of absorption coefficients. Particles are collected on a glass fiber filter (Pallflex E70-2075W, Pall, USA). This instrument operates at a flow rate of 2 L min^{-1} and data was averaged to 1 minute. The raw data was corrected for flow rate, spot area and adjusted to 550 nm. More information on the PSAP is given in the instrumentation section of this dissertation.

The single particle soot photometer (SP2) (Droplet Measurement Technologies, SP2-D) was deployed (by Yafang Cheng, MPI) onboard the plane for measurements of BC mass concentration (M_{BC}). Particulate matter (PM) containing BC passes through a continuous laser beam within a cavity. When the BC particles pass through the laser beam, laser energy is absorbed until the particle incandesces. The incandescence signal is proportional to the mass concentration of refractory BC. The instrument was operated at 0.12 L min^{-1} and was calibrated before and after the campaign.

5.3 Results

Simultaneous measurements of M_{BC} by the SP2 together with the absorption measurements from the PSAP were made to evaluate the MAC during flights over the Hebei Province. Due to the high temperature and the incandescent nature of the SP2 instrument, it is believed that the M_{BC} has little interference from volatile compounds or mineral dust. However, absorption measurements from the PSAP are heavily influenced by the mixing state and coatings of BC particles.[17, 20] Determining the MAC would allow insight into the mixing state of particulate matter (PM) and

presence of mineral dust. All measurements used to determine MAC were taken below an altitude of 2.0 km during different flight days. According to Wang et al., the range of the planetary boundary layer (PBL) heights was 0.9 to 2.0 km. The NOAA Hybrid Single Particle Lagrangian Integrated Trajectory (HYSPLIT) model[151, 152] was also used to help understand the transport and sources of the light absorbing aerosols measured during the flights. All days of the flight experiments presented below had high pressure conditions; winds did not exceed 12 m s^{-1}.

A flight experiment was conducted on 20160517 at 01:21-03:13 UTC at altitudes of was 58-2924 m asl. The profile regions for this flight were JL and QZ. The average M_{BC} for this flight (all altitude < 2.0 km) was 1.34 ± 0. 95 μg m^{-3}. The average absorption coefficient was 21 ± 15 Mm^{-1}. M_{BC} measurements were averaged to 1 minute for compatibility with the PSAP. The MAC of BC was determined as the slope from a linear fit of the absorption coefficient as a function of M_{BC}. The slope (MAC) of the linear regression is 14.80 ± 0.44 m^2 g^{-1} and the y-intercept is 0.45 ± 0.74 Mm^{-1} (R^2=0.93). Table 5.2 and Figure 5.1 below provides the averages of BC and CO, the correlation of the absorption coefficient from the PSAP (y-axis) and the BC mass concentration from the SP2 (x-axis). Back trajectory analysis (Figure 5.2) shows that the air mass during the flight on 20160517 was coming from the southwest, bypassing industrial cities.

Table 5.7 *Average values of BC mass concentration from the SP2 and Absorption coefficients from the PSAP. The MAC values for each flight are also provided. Uncertainty is standard error of the slope of the linear regression.*

DAY	M_{BC} (μg m^{-3})	B_{ap} (Mm^{-1})	Slope (MAC, m^2 g^{-1})	R^2
20160517	1.34 ± 0.95	20.7 ±14.9	14.8 ± 0.4	0.93
20160519	1.09 ± 0.65	19.3 ±12.0	14.6 ± 1.9	0.64
20160528	0.80 ± 0.36	9.7 ±4.5	10.4 ± 0.5	0.72
20160611	0.15 ± 0.06	5.3 ±1.8	22.1 ± 2.0	0.52

A second research flight took place on 20160519 during the times between 7:42-9:09 UTC. The profiling region for this flight was at Luancheng airport where spirals were conducted within 0.058-3.7 km. The average BC mass concentration reported by the SP2 was 1.085 ± 0.65 μg m^{-3}, and the average absorption coefficient was 19.27 ± 11.99 Mm^{-1} below 2.0 km a.s.l. The slope of the linear regression, or MAC, is 14.64 ± 1.90, and the y-intercept is 3.388 ±2.395 Mm^{-1} (R^2=0.64). Back trajectory analysis shows that the air mass originated from the southeastern coastal region and passed over densely populated regions.

Another flight was conducted on 20160528 between the times of 2:16-5:26 UTC, and spirals were performed at JL and XT. The vertical height ranged from 0.058 to 3.1 km (a.s.l.). Within 2.0 km a.s.l., the average BC mass concentration was 0.803 ±0.362 μg m^{-3}, whereas the average absorption coefficient was 9.71 ± 4.50 Mm^{-1}. As was determined for the flight on 20160517, the MAC value was calculated by plotting the relationship of the absorption coefficient at 550 nm from the PSAP to the BC mass concentration as measured by the SP2 (Figure 1C). The MAC for this flight was 10.393 ± 0.548 m^2 g^{-1} and the y-intercept was 1.17 ± 0.49 Mm^{-1}

(R^2=0.723). 24-hour back trajectory analysis showed that the air mass originated locally from the south east.

Absorption and BC mass concentrations were collected from a flight conducted on 20160611 between the times of 2:52-5:45 UTC. Spirals were performed over LC and XT with a vertical height range of 0.058 – 3.2 km a.s.l. The average BC mass concentration below 2k m is 0.15 ± 0.06 μg m^{-3}, and the average absorption coefficient for this flight was 5.29 ± 1.83 Mm^{-1}. From these aircraft observations, the MAC was 22.11 ± 2.040 m^2 g^{-1}. Back trajectory analysis showed the air mass was coming from the northwestern region of China. There was specific influence from the Gobi Desert.

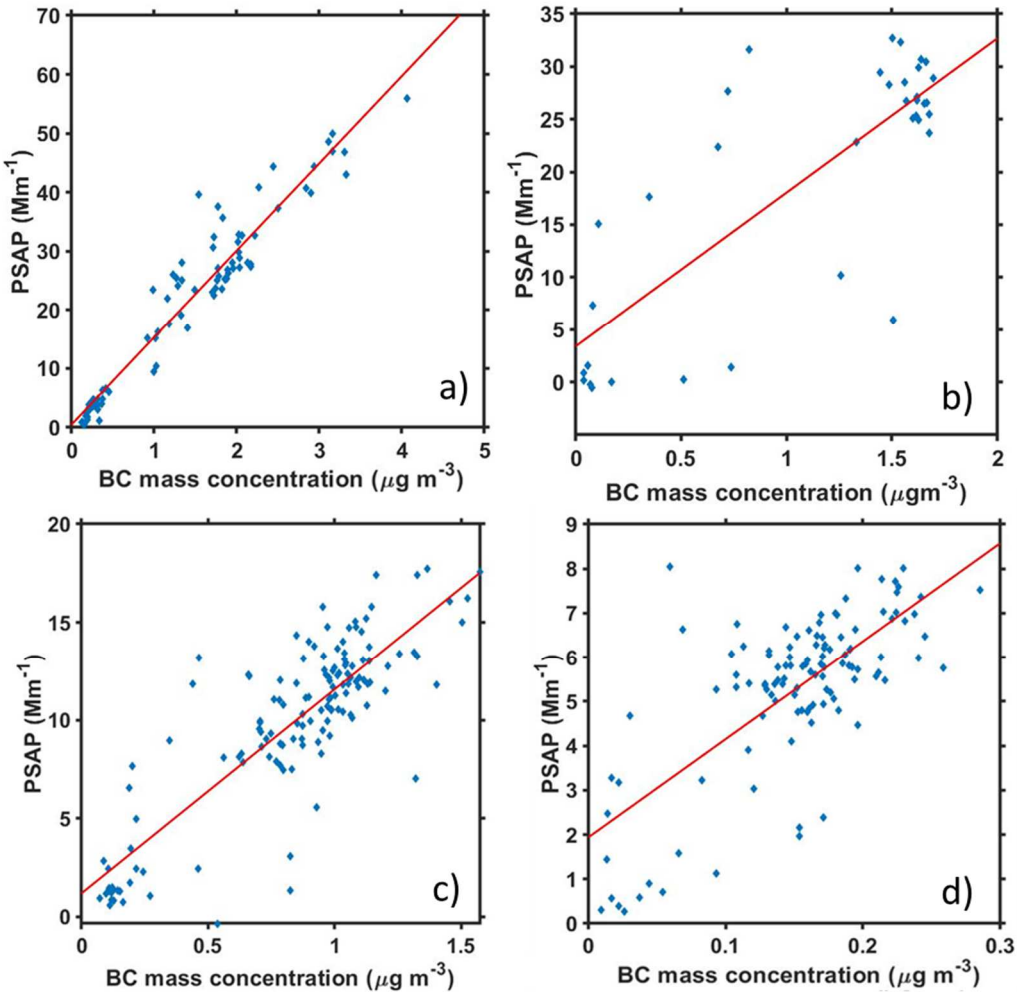

Figure 5.2 *Scatterplots of the absorption coefficient from the PSAP on the y-axis, and BC mass concentration from the SP2 on the x-axis for the research flights conducted on (a) 20160517 (b) 20160519 (c) 20160528 (d) 20160611. Slopes determined by linear regression analysis are equivalent to the MAC.*

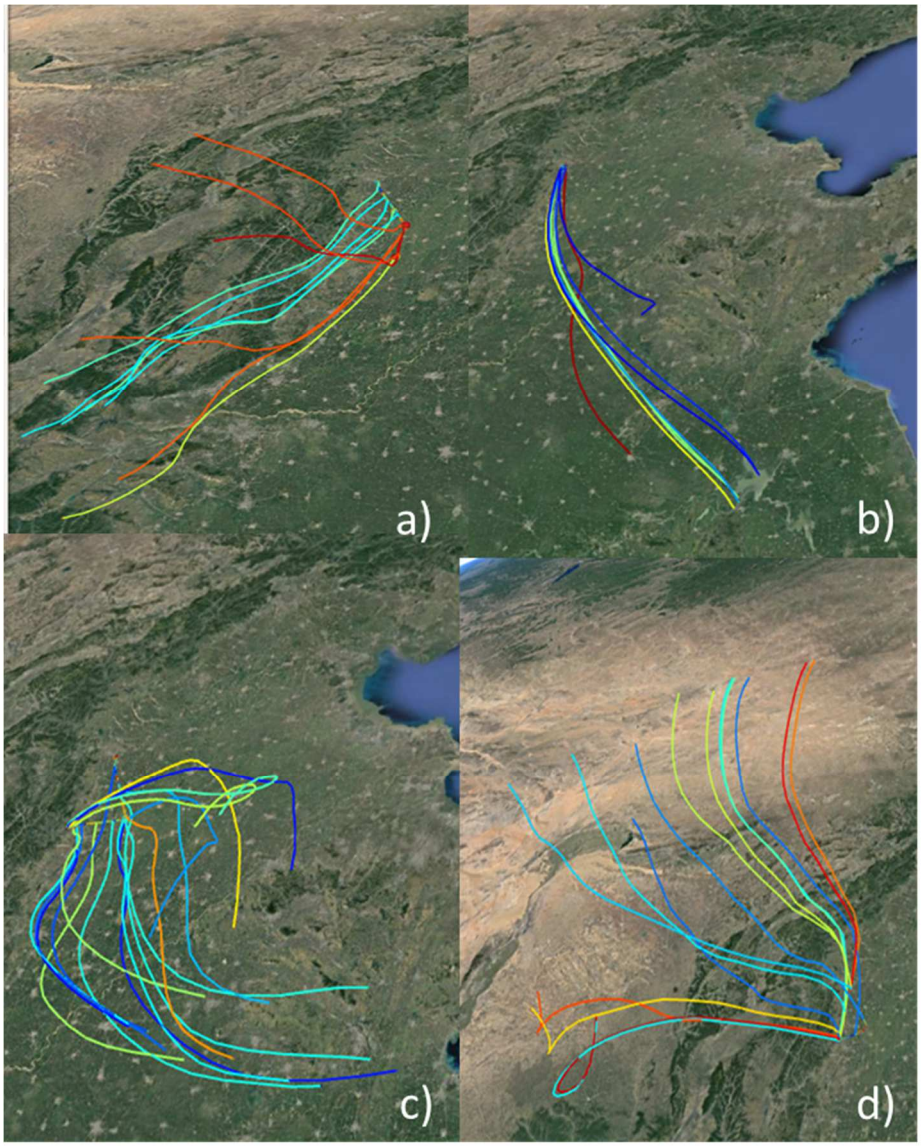

Figure 5.3 *Back trajectories during the flights on (a) 20160517 (b) 20160519 (c) 20160528 (d) 20160611. These back trajectories were provided courtesy of Sarah Benish, Ph.D.*

5.4 Discussion

There was much variability in the MAC value amongst the four flights over the Hebei region China as determined from the SP2 and PSAP (λ = 550 nm). The highest MAC value was observed during the flight on 20160611 (22.1 $m^2 g^{-1}$), although this had the weakest correlation, and the lowest was observed on 20160528 (10.39 $m^2 g^{-1}$). As mentioned previously, Bond and Bergstrom define fresh BC as having a MAC of 7.5 ± 1.2 $m^2 g^{-1}$ at 550 nm. The MAC values observed from the aircraft are significantly higher (~1.4-2.9 x higher) than the widely accepted value for BC MAC. This is likely attributed to collocated mineral dust or coatings of BC by organic aerosol during the aging process, and to differences in particle size distribution.[153] Lee et al. (2020) studied the carbonaceous aerosol from a fire plume in Arizona and determined that the aerosol MAC was enhanced by a factor of 1.2-2.2 greater than bare BC at λ=870nm.[154] This absorption enhancement of BC was likely attributed to the lensing effect involving a BC core and non-absorbing coating. The OC/EC ratio ranged from ~4 to 9 for particles collected at the surface, (see next Chapter 6). However, larger MAC enhancement factors (1.9-5.1) at λ=450 nm were likely attributed to BrC. Sun et al. (2020) studied the enhancement in light absorption for urban aerosols from Guangzhou, China and found that the elevated MAC during the dry season was attributed to altered aerosol optical properties from biomass burning.[155] Radiative transfer models and the Aerosol Robotic Network (AERONET) were also used to confirm an absorption enhancement for a mixture of mineral dust aerosols and anthropogenic aerosols (black carbon absorbing) over East Asia.[156]

The lowest MAC value observed on 20160528 is comparable to previous studies done in Asia. Kondo et al. 2009 used the PSAP (λ=550 nm) and COSMOS for absorption measurements in Guangzhou, China, and EC/OC for carbon measurements. Regional MAC measurements using this technique produced values of 9.9-12 m^2 g^{-1}. Naoe et al. (2009) also determined the regional MAC values in Tsukuba, Japan to be within the range of 10-13 m^2 g^{-1}. In comparison to other experimental flights in this present study over Hebei, China, the SP2/PSAP MAC value on 20160528 is the closest to the values of BC MAC from other ambient measurements in eastern Asia. Back trajectories show that the BC was likely fresh, and had little coating/aging due to the stagnant nature of the air mass. The BC produced did not experience long range transport, and was thus locally sourced.[157, 158]

The experimental flight conducted on 20160611 measured the highest BC MAC value, but the lowest BC mass concentration. A short biomass burning plume occurred on this day, and 24 hour back trajectory analysis shows that the air mass originated from the Gobi desert. The long range transport of these particles caused particles to age and become more coated. The presence of BrC along with organic carbon coatings from biomass burning, and light absorbing mineral desert dust, all contribute to the enhanced MAC value observed during this flight. Coatings and light absorbing dust would bias the MAC high because it enhanced the filter-based absorption measurements, but not the incandescence BC mass concentration measurements from the SP2.

Flights conducted on 20160517 and 20160519 had intermediate MAC values of 14.8 and 14.6 m^2 g^{-1}, respectively. Both days were nearly twice in magnitude to the

literature reference value of MAC for BC. Measurements of BC mass concentration and absorption coefficient were highest during the 20160517 flight experiment. Small plumes from biomass burning were seen on this day[149] and the BrC produced may have contributed to the enhanced value for MAC. Back trajectory analysis shows a stagnant air mass. Thus, light absorbing particles measured during this flight were locally emitted from the densely populated cities and were primarily fresh. Although, the MAC from the 20160517 flight is similar in magnitude to the one observed on 20160519, the conditions are quite different. Unlike the stagnant air mass observed on 20160517, the 24-hour back trajectory for the 20160519 flight showed a long-range air mass coming from the southeast region with no biomass burning plumes. A 48 hour back trajectory shows the air mass originated from the Yellow Sea coastal region. The long-range transport of particles may have contributed to the enhanced MAC value due to particle aging during transport, and the possibility of BC particles being coated with volatile organic compounds (VOCs), sulfates, organic carbon or sea salt. Kahnert et al. (2020) modelled the optical properties of atmospheric BC aerosols and found that sea salt coatings enhance the MAC by up to a factor of 2.[159] Further characterization of water-soluble ion species using ion chromatography needs to be performed for particle component identification. The cluster of data points near the origin in Figure 5.1b for the 20160519 flight also indicates that the boundary layer can be pristine with respect to BC.

5.5 Conclusions

NCP flight-based measurements of BC particles and light absorption were made in May-June 2016 using the SP2 for BC mass concentration, and the PSAP for

absorption coefficient values. The MAC (m^2 g^{-1}) was calculated for the four flights in the PBL below an altitude of 2.0 km. All values for MAC were above the literature value of 7.5 m^2 g^{-1} for fresh BC and tended to be highest when back trajectories showed long-range transport of the air from desert regions. As the particles are being transported over longer distances, they also experience aging and accumulate coatings that enhance light absorption. Some of these coatings may include BrC, sea salt, organic carbon, and sulfates from coal combustion. Light absorbing desert dust may enhance light absorption, as observed during the flight on 20160611. Also, days that had biomass burning plumes (see Benish et al. 2020) tended to have enhanced MAC values. Back trajectory analysis, coupled with MAC values provided insight into the mixing state of BC particles and other light absorbing particles in one of the most polluted regions in the world. The MAC for aerosols collected over the Northern China Plain show much greater MAC values than fresh BC because of aging, added mineral dust and coatings. Thermal optical analysis (TOA) and scanning electron microscopy (SEM) characterization of particles in Hebei were performed for source apportionment and will be discussed further in this dissertation.

Chapter 6: Characterization of Particulate Matter in Xingtai, China using Scanning Electron Microscopy (SEM) and Thermal Optical Analysis (TOA) for Source Identification

6.1 Introduction

Aerosols have a large impact on Earth's climate system, human health and the overall environment. Particulate matter (PM) consists of airborne particles that are known to increase respiratory, cardiovascular and mutagenic diseases.[160] PM is comprised, in part, of carbonaceous species, which are divided into two major classes, organic carbon (OC) and elemental carbon (EC). OC is directly released into the atmosphere or produced by gas-to-particle transformation. EC is produced directly by the incomplete combustion of carbon-based materials and has the ability to absorb solar radiation strongly and contribute to global warming.[161]

Pollution is a global concern which transcends countries borders. Therefore, it is imperative to properly characterize the complex mixture of particulate matter on the basis of physical, chemical, morphological, and dimensional properties for possible source determination. Scanning electron microscopy (SEM) coupled with energy dispersive X-ray (EDX) analysis was used to provide information on the composition and morphology of atmospheric particles. Thermal optical transmittance (TOT) is used for determining the amount of total carbon (TC), EC and OC. [23, 97, 162, 163]

The aim of this work is to evaluate the chemical composition of particulate matter in one of the most polluted cities in the world, Xingtai, China. Understanding the chemical makeup of particles, along with OC/EC ratios from TOT, will allow for

the determination of possible emission sources. Backward trajectory analysis was also conducted to investigate the regional origins and pathways of the airborne particulate matter.

6.2 Materials and Methods

6.2.1 Site description

In this work, the sampling site took place on a rooftop in Xingtai, China (37º10'53.08''N, 114º21'33.75''E) with a high volume (12.48 m^3 hr^{-1}) sampler (Staplex, Brooklyn, NY). The Atmosphere-Aerosol-Boundary-Cloud Interactions (A2BC) campaign took place in the Hebei province from 25 April to 15 June 2016. The purpose of this campaign was to investigate how clouds, aerosol, and trace gases interact with each other based on the utilization of ground and aircraft measurements. Within 25 km of the sampling site, there were over 100 companies that consumed coal and emitted large amounts of pollutants. Some of these industries include glass, cement, chemical, steel, and power plants. Xingtai is considered to be one of the most polluted places in the world and is home to approximately seven million people. The Taihang Mountains are approximately 30 km from Xingtai, and previous studies have shown that these mountains play a role in aerosol dispersion .[164] Although multiple days of sampling took place, this study will focus on four days of particulate sampling during May. Figure 6.1 below shows the location of Xingtai in respect to other major cities in China.

Samples were collected on 16 May 2016, 17 May 2016, 18 May 2016, and 21 May 2016. All days had a maximum temperature greater than 30ºC, and a minimum temperature greater than 25ºC. Each of the previously mentioned days were sunny

except for 18 May 2019 (partly cloudy). There were no forms of precipitation during those days. Forty eight hour back trajectory analyses (500 m AGL) were also performed for each sample day.

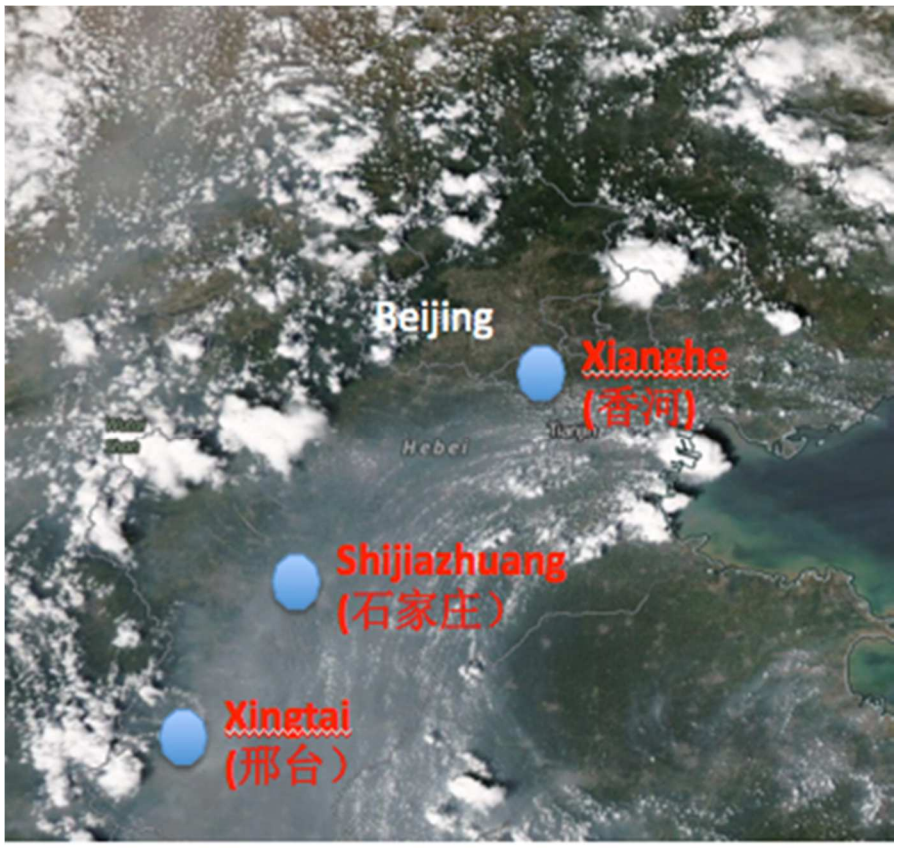

Figure 6.4 *Xingtai's location with respect to other major cities in China (Source Z. Li). Xingtai is approximately 400 km south of Beijing.*

6.2.2 Sample Description

Particles were collected on pre-fired quartz fiber (Pallflex) filters for approximately 8 hours per day (9 am to 5 pm local time). Filters were heavily coated with PM and were later analyzed with the Sunset Lab Carbon Analyzer Thermal Optical Transmittance (TOT) to determine the OC/EC ratio. Before analyzing with SEM-EDX, particles were transferred from the quartz fiber filter to a clean 5 mm x 5 mm

germanium wafer. This was accomplished by using a technique that involved electrostatic charging and high-speed centrifugation as explained thoroughly in Conny et al. 2014.[165]

6.2.3 Computer Controlled SEM

SEM is an imaging method that utilizes a focused beam of high energy electrons to reveal information on the composition and morphology of a sample. The SEM-EDX analyses were carried out with a Tescan MIRA3 scanning electron microscope (Tescan USA Inc., Cranberry Township, PA, USA) equipped with a PulseTor EDX detector at the Environmental Protection Agency (EPA) in Raleigh, NC (Conny et al. 2019). The current and electron beam energy were 0.55 nA and 20 kV, respectively. For this study, the SEM was configured to analyze particles between average physical diameters of 0.4-10 μm. The analysis time per sample was about 1–2 hr. The analysis areas for samples 16, 17, 18, and 21 May 2016 were 4.625, 0.583, 0.706 and 1.036 mm^2, respectively. EDX spectra was used to determine the abundance of 23 elements: carbon (C), fluorine (F), sodium (Na), magnesium (Mg), aluminum (Al), silicon (Si), phosphorus (P), sulfur (S), chlorine (Cl), potassium (K), calcium (Ca), titanium (Ti), vanadium (V), chromium (Cr), manganese (Mn), iron (Fe), nickel (Ni), copper (Cu), zinc (Zn), arsenic (As), lead (Pb), barium (Ba) and tin (Sn).

Table 6.1 below provides the classification rules for the particles. Initially the particles were placed into 26 classes. Similar classes and classes that had very few particles were combined to form 10 condensed classes.

Table 6.8 *Classification rules for ambient particles collected in Xingtai using hierarchical analysis involving elements.*

CLASS	RULE	Rule order
Metals	Al/Si>=6 and counts>900	3
	(Mn+Cu+Ni+Cr+Ba)>=10 and (Mn>=3 or Cu=>3 or Ni>=3 or Cr>=3 or Zn>=3) and (Al+Si)<50 and counts>500	2
Carbon	C>=75	7
	P>0 and counts<2000 and (P+Si+S+Cl+Ca+K+C)>=90 and Al=0	6
	C>=30	24
Quartz	Si>=95	8
	Si>=75 and Al>0 and Si/Al>10 and C<12	9
Fe Oxide	Fe+F>=95	10
	(Al+Si+S+Ca)>0 and (Fe+F)/(Al+Si+S+Ca)>=8	11
Calcium	Ca+C>=70 and Ca>C and Ca>S and S<8 and Si<12	12
Calcium Sulfate	Ca+S>=95 and Ca/S<1.7 and S/Ca<1.7;	13
	(Ca+S)>=70 and Ca/S<1.7 and S/Ca<1.7 and (Ca+S)/(C+Al+Si+K+Fe)>=2.5	14
Ca-Si	(Ca+Si)>85 and Ca>=20 and Si>=11 and Al<=4 and Ca>S and C<15	16
AlSi	(Fe+Al+Si)>=70 and Fe>=10 and Al>=4 and Si>=4 and Fe>K and Fe>Ca;	17
	(Al+Si)>=60 and Al>=4 and Si>=4 and Si>K and Si>Ca and Si>Fe and K<15 and Ca<15 and Fe<15 and C<16	18
	(K+Al+Si)>=60 and K>=8 and Al>=4 and Si>=4 and K>Ca and K>Fe and C<15;	19
	(Ca+Al+Si)>=70 and Ca>=16 and Al>=4 and Si>=4 and Ca>Fe and Ca>K and C<15	21
Mixed AlSi	Si>=5 and Ca>=4 and (Al+Si+K+Ca+Fe+S+P)>=60 and (Ca+S)/(Al+Si+K+Fe+S)<3.4 and C<15;	20
	Si>=5 and Ca>=5 and (Al+Si+K+Ca+Fe+S+P)>=60 and C<30;	22
	(Al+Si+Ca+S)>60 and (Al+Si)/(Ca+S)<3.2	15

	and (Ca+S)/(Al+Si)<3.2 and Al>4 and Si>4 and Ca>4 and S>4 and (Ca+S)>Fe and (Al+Si)>Fe and C<17	
Misc.	(Al+Si+Ca+S)>=70 and Al>=4 and Si>=4 and Ca>=4 and S>=4 and C>=20	23
	Ca>=10 and P>=8 and (Al+Si)<12 and Ca>S and P>S	5
	Ba>2 and Ti=0 and S>5 and (Ba+S)/(Al+Si+Ca+K+Fe)>1.5	4
	S>=80	1
	true	25

6.2.4 Thermal-Optical Transmission (TOT) Analysis

TOT, used to analyze bulk samples of aerosol particles collected on quartz fiber filters, involves the thermal evolution of OC during a He phase, and of EC during the He-Ox phase using a specific temperature protocol. The formation and evolution of char is monitored with the transmittance of a laser through the filter. The signal decreases as charred material is formed, and the signal increases as the char and EC evolve; carbohydrates such as sucrose char extensively on heating. The OC/EC split point is determined when the laser increases to the point where the laser returns to the initial transmittance signal. More information of this method can be found in Chapter 1 of this dissertation.

A square shaped section of a quartz filter of 1.00 cm^2 was used to determine the EC and OC concentrations of each sample with TOT. All the TOT experiments were carried out on a single optical carbon analyzer (Sunset Laboratory Carbon Analyzer, Tigard, OR) at NIST, Gaithersburg. Two different temperature protocols were used, and multiple replicates were completed. The Quartz temperature protocol

was developed by the manufacturer of the instrument and is based on the previous work done by Birch and Cary et al. (1996).[100] The NIST-EPA-C protocol was developed in collaboration between National Institute of Standards and Technology (NIST) and the EPA.[23] This protocol is considered suitable protocol for a diverse number of sample types that include high-charring and low-charring particulates. Replicate samples were analyzed to reduce the effects of non-uniformity of the deposited aerosols on the filters. The temperature steps for each protocol are given below in Table 6.2.

Table 6.9 *Temperature steps and residence times for the Quartz and NIST-EPA-C protocols.*

Carrier Gas	Temperature (ºC)		Residence Time (s)	
	Quartz	NIST-EPA-C	Quartz	NIST-EPA-C
He	315	200	60	60
He	475	400	60	60
He	615	600	60	60
He	870	785	90	150
He+O_2	550	550	45	60
He+O_2	625	620	45	60
He+O_2	700	690	45	45
He+O_2	775	760	45	45
He+O_2	850	830	45	45
He+O_2	910	900	120	90

6.2.5 Back Trajectory Analysis

Backward trajectory analysis was used in this study to identify the pathways of transport for the air masses for different days. Trajectories were calculated using the Hybrid Single Particle Lagrangian Integrated Trajectory model (HYSPLIT)[151] developed by National Oceanic and Atmospheric Administration (NOAA) and

Australian Bureau of Meteorology. Backward trajectories (Figure 2a-d) shows that the air parcel came from the Gobi Desert and northern Mongolia on 16 May 2016, and southeast of Xingtai near the coast of the Yellow Sea on 21 May 2016. Both air parcels for 17 and 18 May 2016 depict an immediate influence from southern industrial cities such as Handan. However, the backward trajectory shows the air parcel also coming from the northern region of Mongolia and as far as Russia (after dipping from the south of Xingtai) on 17 May 2016. HYSPLIT shows the plume for 18 May 2016 originating from the southern province of Hubei and Dabie Mountains region. Particles from the north generally undergo more settling while particles originating from the south travel through the PBL. Particles of southern origin undergo turbulent mixing on subgrid scales and are not represented accurately by the trajectories.

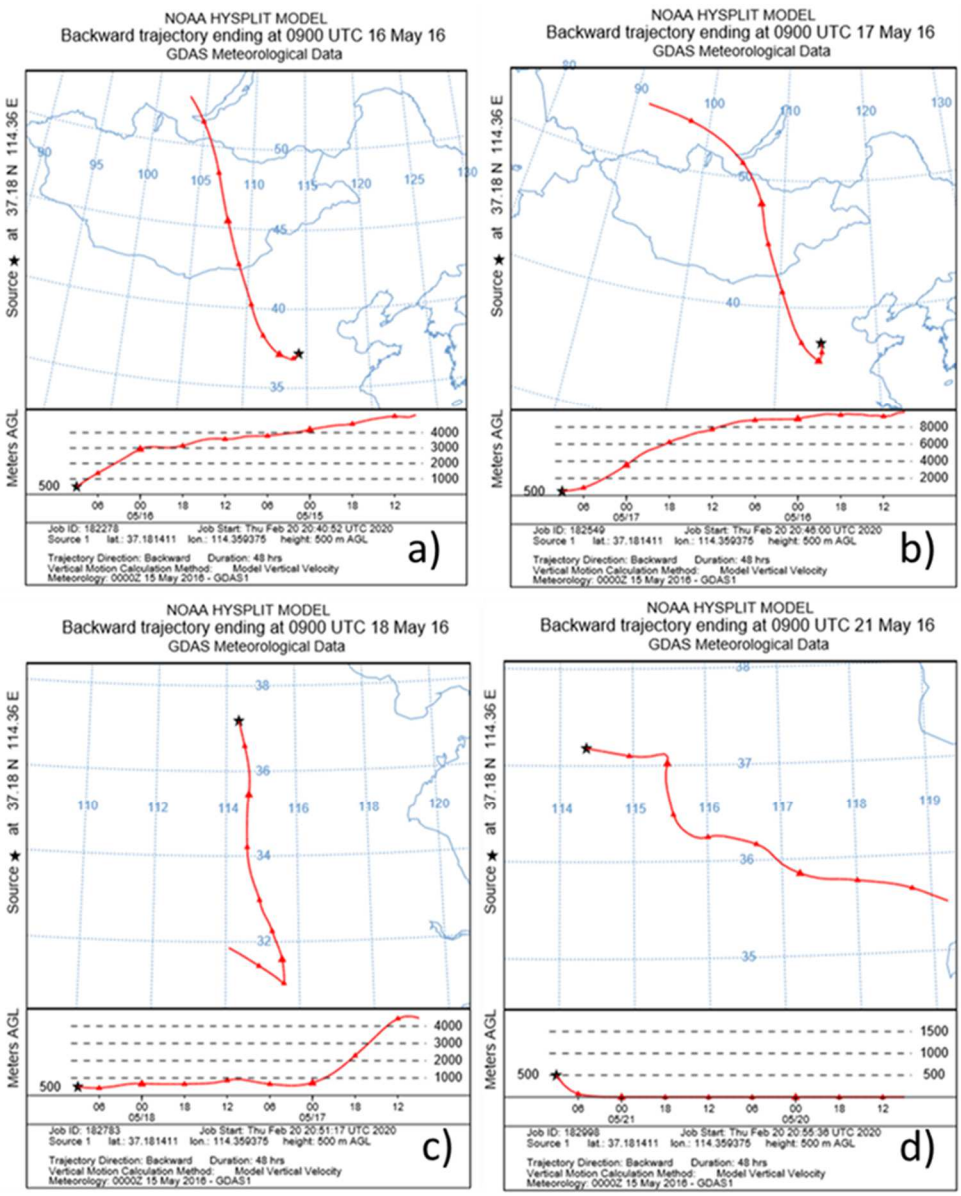

Figure 6.4 *HYSPLIT 24 hour back trajectories initiated at 500 m altitude (mid-PBL) for (a) 16 May 2016 (b) 17 May 2016 (c) 18 May 2016 and (d) 21 May 2016.*

6.3 Results and Discussion

6.3.1 Data Reduction

A total of 9000 particles were analyzed with SEM from the 4 different samples. Approximately 2000 particles were analyzed for 20160516, 20160517, 20160518

collection days and 3000 particles were analyzed for particles collected on 21 May 2016. Due to the large amount of data, hierarchical cluster analysis was used to retain the most important information about particle association. Here, we describe nine particle clusters according to their chemical composition. Table 6.3 below provides the percent number of particles for the different classes on each day.

Aluminum Silicate: Soil particles or Asian dust particles with ambient origin have compositions dominated by Al and Si. This class of particles forms the largest cluster of particles for all days classified. These particles were mainly crustal in origin. There were no forms of precipitation during the sampling days, thus soil particles were suspended in the air by wind or traffic.[166] Some of these particles may originate from the Gobi desert in Mongolia, as supported by backward trajectories. Fly ash particles have similar composition, but the shape factor may help distinguish between the two. Generally, a shape factor near unity indicates a spherical particle. Particles of a spherical morphology tend to indicate that the source is from high temperature combustion of fluid melts. [166-168]

Mixed Aluminum Silicate: This class of particles incorporates Aluminum silicates with calcium (Ca), potassium (K) and sulfur (S). These particles are very similar to the Aluminum Silicate particles described previously. Their source may be crustal, or road dust. This class showed higher percentages during days when backward trajectories showed immediate transport from the southern industrial region of Hebei province (20160517 and 20160518).

Quartz: Particles identified as quartz (SiO_2) are comprised mainly of silicon (Si) and oxygen (O). As with Aluminum silicate, quartz particles may originate from soil suspension. Quartz is known to be a constituent of many different rock types. However, another well-known source of quartz particles is coal combustion. Si is also found in coal ash where SiO_2 is created by reducing silicon-based compounds at high temperatures, followed by evaporation, oxidation and nucleation.[166]

Calcium rich: This class of particles probably includes calcium oxide (CaO), limestone ($CaCO_3$) and dolomite ($CaMg(CO_3)_2$. These particles are primarily dominated by Ca with some impurities of S and Si. Calcium oxide, or commonly known as quick lime, is used for the industrial production of cement. Limestone particles are produced for building materials and the metallurgy industry.[167] An additional source of dolomite is raw coal ash.[166]

Calcium Sulfate (Gypsum): Particles in this class originate from building surfaces and from cement.[167] These particles generally have an irregular shape. Raw coal ash is also comprised of calcium sulfate ($CaSO_4$).

Carbon rich: This class of particles contains biological particles and soot. Soot, also known as black carbon, is generated from fires, traffic (mainly diesel engines) and combustion of paraffin and fuel oil. Biological particles may consist of bacteria, fungi, pollen and other materials of plant or animal origin.[167] It is difficult to distinguish between the anthropogenic and biological carbon particles based upon

only elemental analysis. Manually reviewing the particle images improves the confidence of distinguishing the two.

Iron Oxide: Particles of this class have both a natural and anthropogenic source. including soil, metallurgy, steelwork, and mining.[169] The oxidation of pyrite found in coal combustion is another source of iron particles. These particles are uniquely spherical due to the smelting of iron.[167]

Metals: These particles consist largely of individual metals such as Cu, Ni, Zn, Mn, Cr and Ba. Each of these metals originate from different anthropogenic sources such as traffic and industrial processes.

Miscellaneous: Particles classified as miscellaneous represent less than 6% of the total particles. These are the remaining particles after the classes have been occupied. The particles in this class also contained minor subclasses of calcium phosphate, barium sulfate and sulfate particles. Particles classified under calcium phosphate may originate from bone mineral used in agricultural fertilizer.[170] Barium Sulfate particles contain barium which is usually associated with brake or tire wear.[165] Particles under the sulfate class are comprised primarily of sulfur alone. Sulfate particles likely represent secondary aerosols where there is a gas-to-particle conversion of sulfur-containing compounds. Coal combustion is the main source of sulfur dioxide, which is a precursor to sulfate particles.[166]

Table 6.10 *The percentages of particles assigned to each class.*

Classes	20160516 (%)	20160517 (%)	20160518 (%)	20160521 (%)
AlSi	40.61	34.03	32.07	40.89
Mixed AlSi	16.81	25.15	29.78	10.68
Quartz	11.34	5.83	5.83	7.23
Calcium rich	13.82	7.50	1.88	0.69
Calcium Sulfate	2.28	10.04	15.88	12.23
Carbon rich	8.61	9.38	9.39	20.19
Iron Oxide	2.18	3.4	2.18	1.41
Metals	1.16	0.76	0.15	0.27
Misc.	3.19	3.91	2.84	6.41

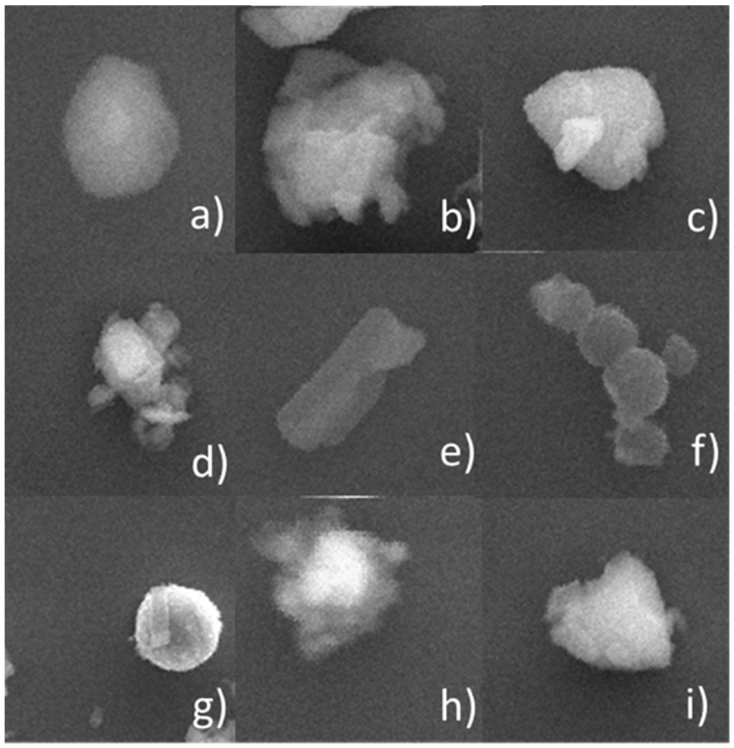

Figure 6.5 *SEM images of particles that represent each class and their respective average diameter: a) aluminum silicate (coal fly ash particle, 1.58 μm) b) Mixed aluminum silicate (1.71 μm) c) Quartz (4.88 μm) d) calcium rich particle (3.87 μm) e) calcium sulfate (gypsum, 2.28 μm) f) carbon rich (soot aggregate, 2.29 μm) g) iron oxide (3.96 μm) h) metals (Cu, 1.40 μm) i) miscellaneous (calcium phosphate, 3.10 μm)*

6.3.2 Carbonaceous Species of Particulate Matter

The OC and EC concentrations and OC/EC ratios are valuable when assessing the sources of ambient carbonaceous particles. Table 6.4 provided below gives the mean concentrations (masses per unit area) of OC, EC and TC for the four different days in May 2016 using the Quartz and the NIST-EPA-C temperature protocols. The range in average OC and EC for the Quartz protocol is 28.3 to 36.7 μg cm^{-2} and 3.5 to 7.3 μg cm^{-2} respectively. For the NIST-EPA-C protocol, the OC and EC concentrations ranged from 31.9 to 41. 5 μg cm^{-2} and 4.1 to 10.1 μg cm^{-2}, respectively. Results show that both 17 and 18 May 2016 had the highest values for TC with over 40 μg cm^{-2} for both protocols. The amount of EC for these two days was nearly double the EC concentration for 16 and 21 May 2016.

The relationship between OC and EC aids in the characterization the emission and transformation of bulk aerosols. Diesel and vehicular exhaust possess an OC/EC ratio range of 1.0-4.2 [161, 171] while wood burning ratio is 16.8-40.0.[172] Chen et al. 2006 reported coal smoke having an OC/EC ratio within the range of 2.5-10.5. Biomass burning was reported having an OC/EC ratio of 7.7. All of these OC/EC ratio ranges are from previous TOT measurements from the literature.

As shown in Table 6.4 below, the OC/EC was 4.6-8.5. These values are comparable to studies conducted in Beijing,[173] Guangzhou,[174] Nanjing, [175] Ghent, Belgium[176] and Milan, Italy[177] with the TOT method. The average OC/EC ratio for all 4 days was 6.54 ±2.14 when using the Quartz protocol and 6.17 ±2.27 for the NIST-EPA-C protocol. 20160516 and 20160521 experienced higher values for OC/EC, while 20160517 and 20160518 experienced lower ratios. Days that experienced a

higher TC also had a lower OC/EC ratio. All TC values reported by the two protocols were within measurement uncertainty (1σ) from one another. However, 18 May 2016 TC values show a greater disparity amongst the protocols. This might be attributed to uneven sampling on the filter because the OC/EC ratios are within 1σ from each other.

The main emission sources of EC and OC in China include vehicular exhaust, coal combustion and biomass burning.[178, 179] According to back trajectory analysis from HYSPLIT (as shown earlier in Figure 6.2a-d), the lowest OC/EC ratios occurred during the days when the air mass was immediately coming from the south and passing through Handan, China and other heavily populated cities. Thus, the particles collected at the Xingtai sampling site were primarily affected by diesel and vehicular emissions during 17 and 18 May 2016. Hence, the lower OC/EC ratio observed those two days. Samples collected on 16 and 21 May 2016 experienced higher ratios but lower TC concentrations. Backward trajectory analysis shows that particle samples collected on 16 May 2016 were affected by an air mass coming from the northwest and east from the Yellow sea on 21 May 2016. Higher ratios on these two days suggest a lesser influence on vehicular emissions but a larger impact from coal combustion and biomass burning in the region.

Table 6.11 *Average and standard deviation values (1σ) for the concentrations of OC, EC, TC and EC/OC per square area.*

	16 May 2016		17 May 2016		18 May 2016		21 May 2016	
	Quartz	NIST-EPA-C	Quartz	NIST-EPA-C	Quartz	NIST-EPA-C	Quartz	NIST-EPA-C
OC ($\mu g/cm^2$)	28.26 ±6.35	31.92 ±5.96	36.68 ±2.95	36.27 ±7.13	34.38 ±1.86	41.45 ±1.67	30.03 ±0.31	29.03 ±1.04
EC ($\mu g/cm^2$)	3.47 ±0.76	4.08 ±0.54	7.96 ±0.98	8.75 ±2.63	7.32 ±0.61	10.05 ±1.73	3.95 ±1.52	3.57 ±0.91
TC ($\mu g/cm^2$)	32.47 ±6.69	36.00 ±6.46	44.62 ±3.84	45.01 ±3.73	41.69 ±1.35	51.5 ±3.37	33.97 ±1.21	32.61 ±1.89
OC/EC	8.53 ±1.60	7.80 ±0.61	4.63 ±0.25	4.25 ±0.49	4.74 ±0.66	4.19 ±0.59	8.24 ±3.26	8.45 ±1.67

6.4 Conclusions

SEM-EDX is a useful technique for characterizing particulate matter collected in Xingtai, China. The chemical composition provides information about the origin of these particles and their formation processes. The diversity of particle types shows the complex nature of ambient particles. Hierarchical cluster analysis of SEM-EDX data revealed different particle groups and reflects the multiple sources. Aluminum silicates and mixed-aluminum silicates are the major classes of particles where both are either crustal or anthropogenic (coal fly ash) in origins. Other cluster groups are representative of natural, vehicular emissions and coal combustion sources. TOA is another well-known method used to quantify the abundance of carbonaceous species and to give further information about sources. Both 20160517 and 20160518 exhibited lower OC/EC ratios which suggest diesel or vehicular traffic from the southern region of Hebei province may be an influential immediate source, as supported by backward trajectory analysis. These days also showed a higher TC concentration. Higher OC/EC ratios measured on 20160516 and 20160521 are

indicative of coal combustion being the major source. The combination of results from SEM-EDX particle characterization and TOT analysis supports that the major sources of the particles in Xingtai, China are crustal and coal combustion. More analysis on ion composition and particle shape should be done to provide a complete picture of source evaluation.

Chapter 7: Conclusion and Future Work

In summary, the work in this dissertation describes the measurement of light absorbing aerosols in the atmosphere, as well as in the laboratory. A BC surrogate and atmospherically relevant light absorbing aerosols were generated under laboratory conditions to provide information to help improve the understanding of health effects, radiative forcing, and climate change. Atmospherically relevant particles were generated under laboratory conditions to evaluate the absorption response of two Aethalometer models, and a thermal optical instrument. Ambient light absorbing aerosols were also quantified from research campaigns in the NYC region and in China. The work presented in here involves two parts: calibrating instrumentation for BC (and EC) in the laboratory, and measuring light absorbing, ambient aerosols to evaluate distributions and emissions inventories.

With various proposed strategies to measure BC, it is essential that a technique used must have fundamentally sound calibration procedures as variable conditions could skew results. The Aethalometer is a filter-based instrument that measures the mass concentration of BC but has no standard calibration procedure associated with it. In Chapter 2 of this dissertation, I developed a potential calibration procedure and correction scheme for the Model AE31 multi-wavelength Aethalometer of Magee Scientific. The potential candidate reference material Cab-O-Jet 200 can mimic the properties of BC found in the atmosphere. This BC surrogate was first dried, conditioned, and size selected by a DMA. The mobility selected BC surrogate of a known mass was measured by a CPC and Aethalometer that operated in parallel. The AE31 underestimated the BC mass concentration at multiple

wavelengths but could be corrected. In this chapter, I also examined the response of the Aethalometer to atmospherically relevant particles, such as BrC and coated BC. When the BC surrogate was coated with either ammonium sulfate or BrC, an absorption enhancement was observed, and this artefact needs to be accounted for in future ambient studies involving the AE31 model.

In Chapter 3, I characterized the TOA instrument with the same BC surrogate used in Chapter 2 of this dissertation, and with sucrose. Again, I selected a reference material and established a calibration procedure, as no reference material or calibration procedure existed for the EC measurement. I evaluated aqueous binary mixtures of sucrose and the BC surrogate for calibration purposes. Different temperature protocols were examined for this reference binary mixture. The results of OC and EC were closest to the reference values when using the NIST EPA C temperature protocol. With known amounts of EC and OC deposited on the filter, the NIST EPA C protocol properly determined the split point for good separation of OC and EC. Measurements of OC and EC shown in this chapter will help calibrate and interpret data from the thermal optical technique widely used for emission studies and model evaluations.

With the extensively characterized BC surrogate, I also developed a technique to evaluate Magee Scientific's model AE33 Aethalometer. For pure BC particles selected by aerodynamic size, the Aethalometer responds linearly and with a total 1σ uncertainty of 13%. Based on this information from lab studies, the Aethalometer was used in the field for measurements of NYC summer BC mass concentrations. The relationship of BC and CO was evaluated on the ground and from an aircraft. Data

presented here show a positive correlation of BC and CO, and higher BC/CO ratios were observed on the weekdays, than on the weekends due to increased diesel use on the weekdays. Using emission inventories of CO from three models, I was able to calculate the BC emissions from the NYC region, and evaluate existing inventories. It is imperative to accurately quantify and understand BC emissions in our communities because higher BC concentrations near major diesel sources lead to greater health impacts and implications of environmental justice.

In Chapter 5, I investigated the light absorbing properties of aerosols in the Xingtai region of the North China Plain. The campaigns Aerosol Atmosphere Boundary Layer Cloud campaign (A^2BC) and ARIAs were conducted to integrate *in situ* measurements, satellite remote sensing and transport models for the understanding of tropospheric chemistry and composition. Onboard the research aircraft were the SP2 and the PSAP instruments. The SP2 measured the mass concentration of refractory BC and the PSAP measured aerosol absorption coefficients. The slope of the linear regression is equivalent to the MAC when the BC mass concentration is plotted on the x-axis and the absorption coefficient is plotted on the y-axis. For all four days presented, the BC MAC values were 14.80 ± 0.44, 14.64 ± 1.90, 10.39 ± 0.55, 22.11 ± 2.04 $m^2\ g^{-1}$ - substantially greater than the literature value of 7.5 $m^2\ g^{-1}$. These relatively high values from light absorbing particles in China are likely enhanced by coatings and may include additional absorbance from mineral dust. Back trajectory analysis was also conducted for source analysis. Particles from stagnant air masses experienced lower MAC values while

particles from long range transport generally had higher MAC values due to aging and coating over time.

Particles collected on quartz filters from the city of Xingtai, China were characterized using SEM-EDX and TOT. The particles were first transferred from the quartz filters to wafers to prevent charging interference with SEM imaging. SEM-EDX analysis revealed the diversity of particle types through hierarchical cluster analysis. The two major classes of particles from the four days analyzed include the aluminum silicate class and the mixed-aluminum silicates class. The sources of particles from these classes are crustal or anthropogenic in origin. TOT analysis was also conducted on these particles to determine the OC/EC ratio. This ratio helps to identify the origins of these particles. The combination of particle characterization from SEM-EDX and TOT OC/EC ratios further supports the major sources of particles in this area of include coal combustion and dust (crustal).

There are many possible future extensions of work presented in this dissertation. One would be to determine the response of the Aethalometers to the BC surrogate at multiple particle sizes. Depending on the source, BC monomers are known to have radii between 10-25 nm, and the fractal dimension will change according to aging and coatings.[159] The atmosphere is full of particles of varying diameters, and it would be preferable to understand the loading effects based on particle size and fractal dimension. Also, more work needs to be done to reduce the uncertainty of these filter-based instruments when other absorbing species are present. Researchers should look into the wavelength dependence determined by filter-based instruments of ambient aerosols and compare it to more direct, *in situ*

methods, such as the photoacoustic spectrophotometer (PAS) during field experiments. More binary, aqueous mixtures of varying OC and EC components should be analyzed to evaluate the split point determination of TOT. Incorporating other components such as iron would prove useful because ambient PM has a complex composition. Further work would also include ion chromatography of the PM collected from Xingtai for compositional information and source apportionment. The ambient MAC values from the research campaign in China are critical to understanding the calculation of radiative forcing from global models. Having a library of MAC inventory from different global sources would be beneficial to climate model input. In this dissertation, I focused on quantifying the total emissions of BC from the NYC region during the summer season. Future work should include BC emissions from other major cities (such as Baltimore, MD, Washington, DC etc.) and the seasonal cycle of the BC/CO ratio. Lastly, the Aethalometer is a relatively low-cost device that can be used to estimate concentrations of BC on a small spatial scale. Thus, communities of vulnerable populations who are exposed to a large number of BC sources can utilize the data from this instrument to address problems of environmental justice.

Appendices

A. Supplemental Information for Chapter 2

A.1 Determining the Contribution of Particles Possessing a charge (q) > +1

Fullerene Tandem DMA coupled with a condensation particle counter was used to investigate the contribution of multiple charges on our BC surrogate measurements. The first DMA was set to an electrical mobility diameter of 300 nm while the second DMA was employed to determine the mobility diameter of particles possessing a q > +1. Different dilutions of the BC surrogate were created by varying the amount of deionized water added. The dilutions created were 1:1000, 1:500, 1:300, 1:200 and 1:100 (BC:water). The dilutions were used to generate a range of total number concentrations. Size distributions were scanned where multiple peaks indicate the presence of particles with multiple charges. The peaks were integrated and the percent contribution of the +2 particle was calculated at different dilutions. Figure S1 shows a distribution of BC aerosols for the 1:1000 dilution. Tandem-DMA was used where the first DMA was set to an electrical mobility diameter of 300 nm. Particles exhibiting a +2 charge were approximately 2.2 times more in mass than a particle with a single charge. Tandem DMA was also performed for the BrC surrogate and for BC coated with AS and BrC. The percentage contributions of particles possessing a +2 charge were accounted for the value of m_p for all materials.

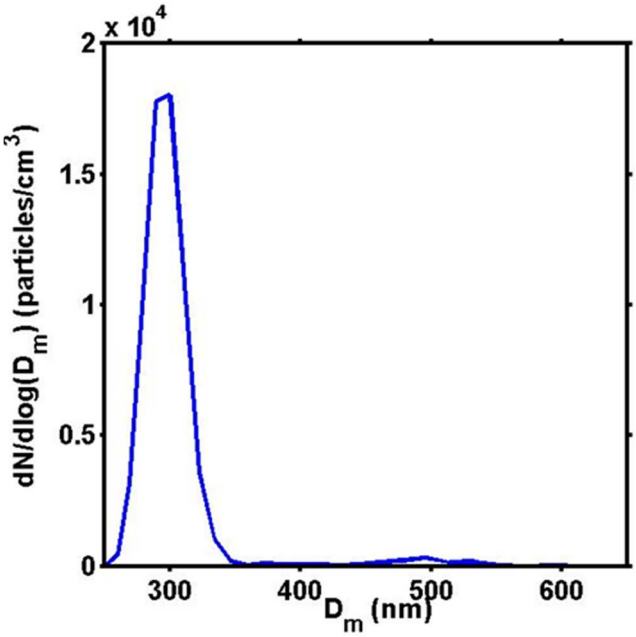

Figure A3 *An example of the distribution of the 1:1000 dilution of the BC surrogate with Tandem-DMA within a range of 250 nm to 650 nm. The first DMA set to an electrical mobility diameter of 300 nm. The prominent peak at ~300 nm represents particles with a +1 charge and the smaller peak at ~500 nm are particles possessing a charge of +2.*

A.2 Correcting Data Using the Jimenez Correction

The nonlinear attenuation response was corrected for by using the loading correction technique described in Jimenez et al. 2007. Briefly, the reported M_{BC} was corrected for loading effects as a function of the attenuation, *K(ATN)*

$$M_{BC} = \frac{b_{ATN}}{SG} * \frac{1}{K(ATN)} \quad \text{(A1)}$$

Where

$$K(ATN) = \frac{\Delta \mathrm{ATN(t)}}{\Delta \mathrm{ATN(0)}} \quad \text{(A2)}$$

Followed by equation 8 to retrieve a linear regression

$$K(ATN) = a + b * \left(e^{-\frac{ATN}{100}}\right) = a + b * T \quad \text{(A3)}$$

Where *a* and *b* are linear regression coefficients and *T* is shorthand notation for $e^{-\frac{ATN}{100}}$. Loading correction coefficients for data at 880 nm in Fig. S3 were a = 0.17 and b = 0.90.

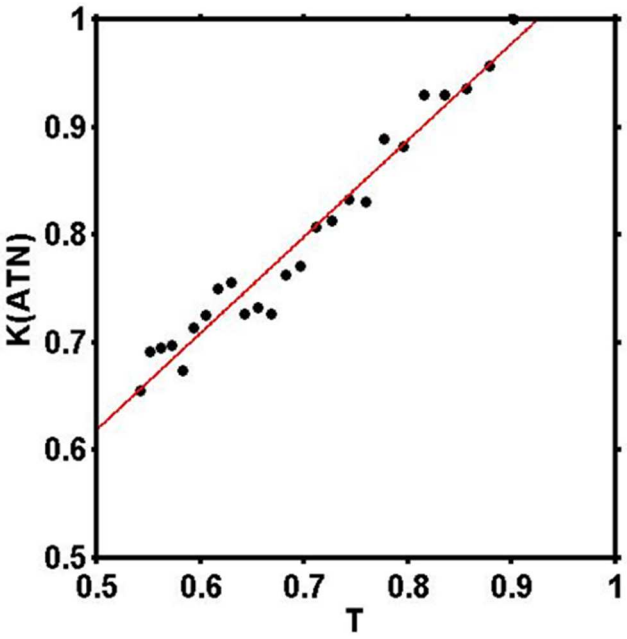

Figure A4 *Mass Shown above is an example of how the linear regression coefficients are calculated during one run. Loading correction linear regression coefficients are defined where T is on the x-axis while K(ATN) is on the y-axis: a=0.17 (y-intercept) b=0.90 (slope).*

Applying this correction to the raw M_{BC} results in the data shown as red triangles in Figure A4; these closely track with M_{CPC}. For the high mass concentration data shown in Figure 2.3b, regression coefficients were calculated for each run experiencing the shadowing effect and applied separately. Differences among loading

correction coefficients may depend on the BC mass concentrations, *ATN*, and length of run.

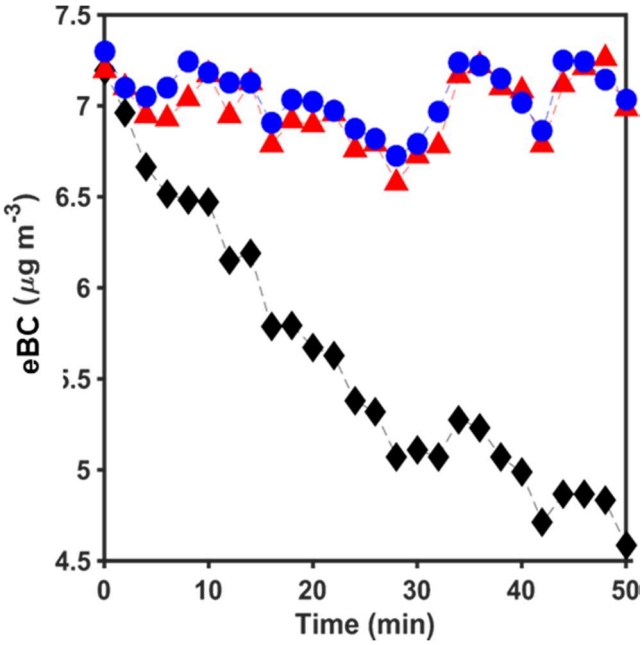

Figure A5 *Time series BC data where the shadowing effect is observed. The uncompensated data is depicted with black diamonds while the corrected data is depicted by red triangles. The in-situ CPC data is shown by the blue circles.*

After this loading correction the Aethalometer more successfully captures the small variability in M_{BC}. The temporal resolution of the filter-based instrument also greatly improves with this loading correction as shown in Figure S4 where corrected M_{BC} now mirror M_{CPC}. The Aethalometer now also reports an average concentration comparable to that of the CPC.

Table A1 *Mass concentration ranges measured by the Aethalometer are provided along with ATN ranges at λ= 880 nm. The linear regression coefficients are shown above for the varying mass concentrations that exhibited a non-linear response due to the shadowing effect.*

Mass concentration range (μg m^{-3}) at λ=880 nm	ATN range at λ=880 nm	Linear regression coefficients λ=370 nm	Linear regression coefficients λ=660 nm	Linear regression coefficients λ=880 nm
18.6-11.8	10.1-79.1	a=0.19 b=0.94	a=0.22 b=0.92	a=0.21 b=0.94
7.2-4.8	7.5-61.4	a=0.19 b=0.89	a=0.21 b=0.87	a=0.17 b=0.90
6.1-4.2	1.0-46.8	a=0.13 b=0.91	a=0.14 b=0.90	a=0.10 b=0.92
12.9-9.2	17.0-76.5	a=0.23 b=0.91	a=0.26 b=0.90	a=0.24 b=0.89
12.1-7.9	7.2-78.6	a=0.33 b=0.78	a=0.31 b=0.76	a=0.30 b=0.78

A.3 BC Coated with Ammonium Sulfate

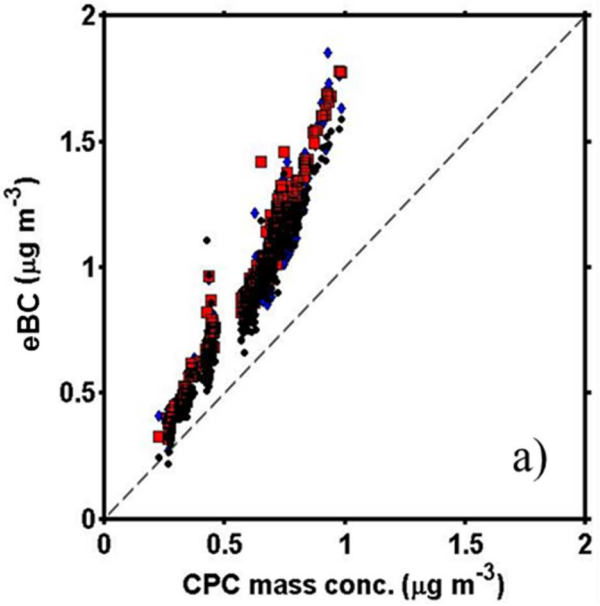

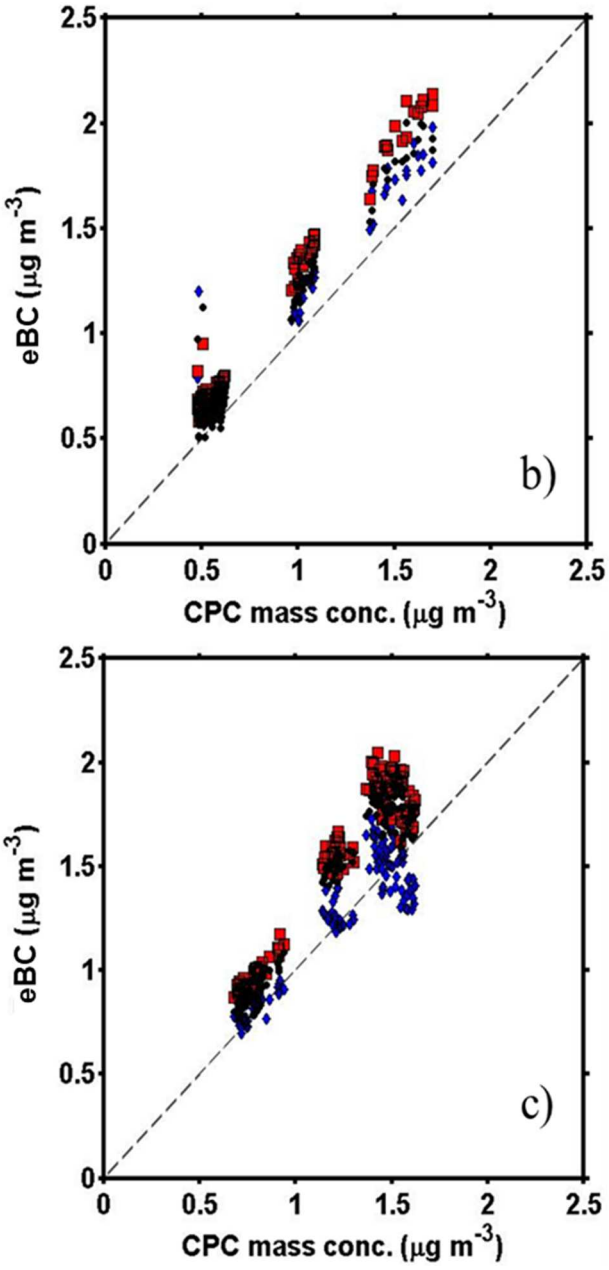

Figure A6 *(a) Correlation of CPC mass concentration with eBC with a 7% BC mass fraction solution with ammonium sulfate. Three different instrumental wavelengths are represented: 370 (blue diamonds), 660 (red squares) and 880 nm (black circles). (b) Correlation of CPC mass concentration with eBC at 880 nm using a 14% BC mass fraction solution with ammonium sulfate. (c) Correlation of CPC mass*

concentration with eBC at 880 nm using a 20.5% BC mass fraction solution with ammonium sulfate.

B. Supplemental Information for Chapter 4

B.1 Theory and Calculations: Tandem DMA and AAC to determine Particle Mass

To determine the mass of a particle with a specific size, tandem AAC and DMA analysis was performed. When set to aerodynamic diameters of 20 and 300 nm using the AAC, the DMA coupled with a CPC measured aerosol size distribution. The geometric mean was determined and used to calculate particle mass. An example of this distribution is given below for when the AAC was set to an aerodynamic diameter of 200 nm. The geometric mean mobility diameter of three trials was 202 ± 9.0 nm. When set to an aerodynamic diameter of 300 nm, the geometric mean mobility diameter was 293 ± 9.8 nm. As described in Tavakoli et al. 2014, particle relaxation time, τ, is defined by the mass, m, multiplied by the mobility of the particle, B.[59]

$$\tau = Bm \qquad \text{(B1)}$$

Particle's mobility is expressed as

$$B = \frac{C_c(d_{mo})}{3\pi\mu d_{mo}} \qquad \text{(B2)}$$

d_{mo} is the mobility diameter and μ is viscosity of the carrier gas? In this case, the viscosity value at 23°C is 1.827 x 10^{-14} nm^2 ns^{-1} and C_c is the Cunningham slip factor.

The aerodynamic diameter is related to particle relaxation time as shown below. Density and shape of the particle do not impact relaxation time.

$$\tau = \frac{C_c(d_{ae})\rho_0 d_{ae}^2}{18\mu} \qquad \text{(B3)}$$

The value for ρ_0 is 1000 kg m^{-3} and d_{ae} is the aerodynamic diameter of the particle. The mass of the particle can be determined when the relaxation time and mobility are known. Thus, the 200 nm and 300 nm particles possessed an average mass of 4.2 ± 0.3 and 13.7 ± 0.6 fg, respectively. The particle masses were used to convert number concentration values from the CPC to mass concentrations of black carbon.

B.2 Intercomparison of the filter-based and the CPC mass concentration for 300 nm particles

The AAC was configured to also size select CB particles with an aerodynamic diameter of 300 nm. Again, the BC mass concentrations determined by the Aethalometer and CPC were compared to one another, and the mass concentration range tested in this study is 0 μg m^{-3} to approximately 10 μg m^{-3}. For the larger particle, the linear regression of M_{BC} versus M_{CPC} at λ= 880 nm exhibited a slope of 0.997 ± 0.030. As with the 200 nm particle, the linear regression includes the value for a blank HEPA filtered air run. A slope near unity indicates that the Aethalometer accurately quantifies the concentration of black carbon under these laboratory conditions. The intercomparison results from the 200 nm particle and the 300 nm particle are very similar when measuring at the Aethalometer's 880 nm wavelength. Thus, this proves that the aerodynamic size of this particular BC particle does not impact the mass concentration determination of this filter-based instrument in the near-IR range.

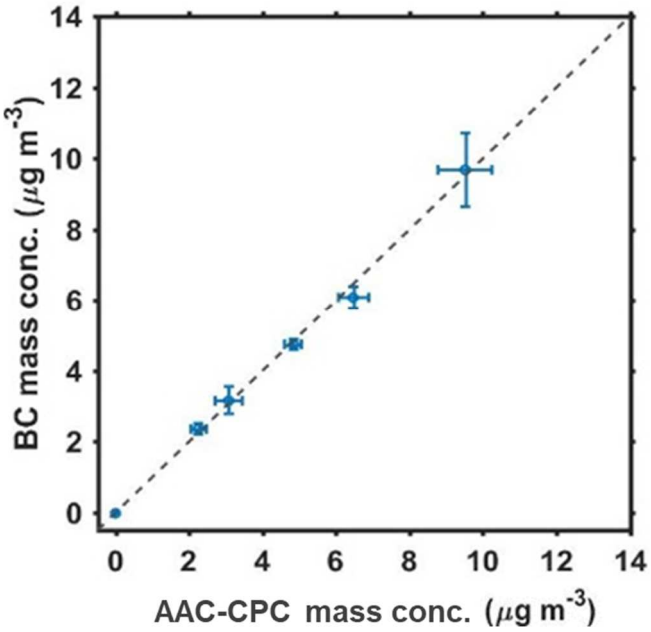

Figure B1 *Correlation of CPC mass concentration with the Aethalometer BC mass concentration (λ=880 nm). Particles had an aerodynamic diameter of 300 nm. Data points are averages of the entire run, and the error bars are 1σ.*

B.3 Wavelength dependence of the AE 33 model for 300 nm particles

The wavelength response was determined for particles with a larger aerodynamic diameter of 300 nm, as shown below in Figure S2. This run exhibited an average BC mass concentration of 6.08 μg m^{-3} (λ = 880 nm). The equivalent mass concentration value at λ = 370 nm reads 31% less than the value at λ=880 nm.

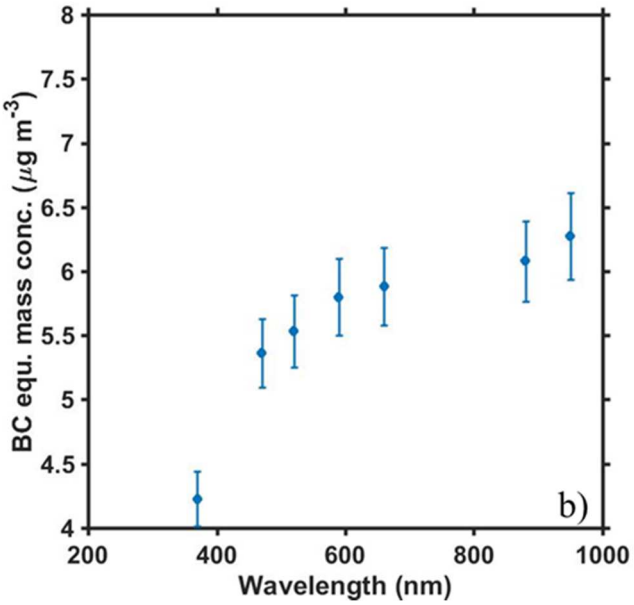

Figure B2 *Wavelength dependence for a 300 nm particle during one 45 minute run at 7 different wavelengths. All error bars are 1σ.*

B.4 Determining the 24-hour average of BC and CO at the Queens NR site during Summers 2018 and 2019

Table B2 *The average, standard deviation (STD, 1σ), standard deviation of the mean, maximum and minimum values for 24-hour averages of BC and CO concentrations. All values are from the Queens NR site during the summers of 2018 and 2019.*

		2018					2019				
BC (μg m^{-3})		AVG	STD	STD of mean	MAX	MIN	AVG	STD	STD of mean	MAX	MIN
	weekday	1.14	0.50	0.09	2.17	0.21	1.20	0.47	0.08	3.01	0. 14
	weekend	0.84	0.34	0.09	1.51	0.19	0.60	0. 21	0.06	1.07	0. 16
CO (ppb)	weekday	265.5	71.1	12.4	410.4	101.9	312.9	71.4	12.4	698.6	201.3
	weekend	289.7	67.3	18.6	392.5	131.3	275.5	40.7	11.2	378.6	203.2

.

B5. Emissions of BC and CO from FIVE 2019

Figure B5 FIVE (a) BC emissions and (b) CO emissions for the NYC region. Color bar denotes the tons per day of emissions. The outlined area is the region of study.

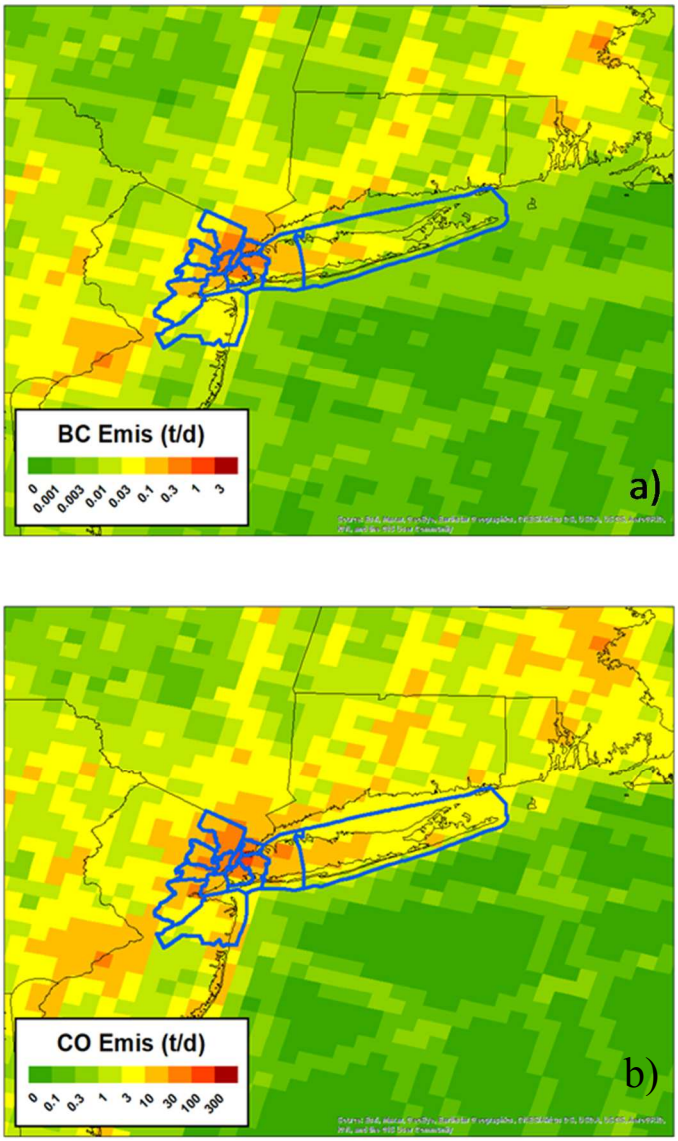

B6. NEI Sectors

Fuel Combustion: Comm/Institutional-Biomass, Comm/Institutional-Coal, Comm/Institutional-Natural Gas, Comm/Institutional-Oil, Comm/Institutional-Other,

Electric Generation-Biomass, Electric Generation-Coal, Electric Generation-Natural Gas, Electric Generation-Oil, Electric Generation-Other, Industrial Boilers, ICEs-Biomass, Industrial Boilers, ICEs-Coal, Industrial Boilers, ICEs-Natural Gas, Industrial Boilers, ICEs-Oil, Industrial Boilers, ICEs-Other**,** Residential-Natural Gas, Residential-Oil, Residential-Other, Residential-Wood.

Mobile: Aircraft, Commercial Marine Vessels, Locomotives, Non-Road Equipment-Diesel, Non-Road Equipment-Gasoline, Non-Road Equipment-Other, On-Road Diesel Heavy Duty Vehicles, On-Road Light Duty Vehicles, On-Road Gasoline Heavy Duty Vehicles, On-Road Diesel Heavy Duty Vehicles, On-Road Diesel Light Duty Vehicles, On-Road Gasoline Heavy Duty Vehicles, On-Road Gasoline Light Duty Vehicles

Other: Commercial Cooking

Bibliography

1. Seinfeld, J. H.; Pandis, S. N., *Atmospheric chemistry and physics: from air pollution to climate change*. John Wiley & Sons: 2016.
2. McNaughton, C. S.; Clarke, A. D.; Howell, S. G.; Moore, K. G.; Brekhovskikh, V.; Weber, R. J.; Orsini, D. A.; Covert, D. S.; Buzorius, G.; Brechtel, F. J.; Carmichael, G. R.; Tang, Y. H.; Eisele, F. L.; Mauldin, R. L.; Bandy, A. R.; Thornton, D. C.; Blomquist, B., Spatial distribution and size evolution of particles in Asian outflow: Significance of primary and secondary aerosols during ACE-Asia and TRACE-P. *Journal of Geophysical Research-Atmospheres* **2004,** *109* (D19), 19.
3. Poschl, U., Atmospheric aerosols: Composition, transformation, climate and health effects. *Angewandte Chemie-International Edition* **2005,** *44* (46), 7520-7540.
4. Boucher, O.; Randall, D.; Artaxo, P.; Bretherton, C.; Feingold, G.; Forster, P.; Kerminen, V. M.; Kondo, Y.; Liao, H.; Lohmann, U.; Rasch, P.; Satheesh, S. K.; Sherwood, S.; Stevens, B.; Zhang, X. Y.; Bala, G.; Bellouin, N.; Benedetti, A.; Bony, S.; Caldeira, K.; Del Genio, A.; Facchini, M. C.; Flanner, M.; Ghan, S.; Granier, C.; Hoose, C.; Jones, A.; Koike, M.; Kravitz, B.; Laken, B.; Lebsock, M.; Mahowald, N.; Myhre, G.; O'Dowd, C.; Robock, A.; Samset, B.; Schmidt, H.; Schulz, M.; Stephens, G.; Stier, P.; Storelvmo, T.; Winker, D.; Wyant, M., Clouds and Aerosols. *Climate Change 2013: the Physical Science Basis* **2014**, 571-657.
5. Bond, T. C.; Doherty, S. J.; Fahey, D. W.; Forster, P. M.; Berntsen, T.; DeAngelo, B. J.; Flanner, M. G.; Ghan, S.; Karcher, B.; Koch, D.; Kinne, S.; Kondo, Y.; Quinn, P. K.; Sarofim, M. C.; Schultz, M. G.; Schulz, M.; Venkataraman, C.; Zhang, H.; Zhang, S.; Bellouin, N.; Guttikunda, S. K.; Hopke, P. K.; Jacobson, M. Z.; Kaiser, J. W.; Klimont, Z.; Lohmann, U.; Schwarz, J. P.; Shindell, D.; Storelvmo, T.; Warren, S. G.; Zender, C. S., Bounding the role of black carbon in the climate system: A scientific assessment. *Journal of Geophysical Research-Atmospheres* **2013,** *118* (11), 5380-5552.
6. Redmond, H. E.; Dial, K. D.; Thompson, J. E., Light scattering and absorption by wind blown dust: Theory, measurement, and recent data. *Aeolian Research* **2010,** *2* (1), 5-26.
7. Bellouin, N.; Quaas, J.; Gryspeerdt, E.; Kinne, S.; Stier, P.; Watson-Parris, D.; Boucher, O.; Carslaw, K. S.; Christensen, M.; Daniau, A. L.; Dufresne, J. L.; Feingold, G.; Fiedler, S.; Forster, P.; Gettelman, A.; Haywood, J. M.; Lohmann, U.; Malavelle, F.; Mauritsen, T.; McCoy, D. T.; Myhre, G.; Mulmenstadt, J.; Neubauer, D.; Possner, A.; Rugenstein, M.; Sato, Y.; Schulz, M.; Schwartz, S. E.; Sourdeval, O.; Storelvmo, T.; Toll, V.; Winker, D.; Stevens, B., Bounding Global Aerosol Radiative Forcing of Climate Change. *Reviews of Geophysics* **2020,** *58* (1), 45.
8. Morgan, M. G.; Adams, P. J.; Keith, D. W., Elicitation of expert judgments of aerosol forcing. *Climatic Change* **2006,** *75* (1-2), 195-214.
9. Andreae, M. O.; Gelencser, A., Black carbon or brown carbon? The nature of light-absorbing carbonaceous aerosols. *Atmospheric Chemistry and Physics* **2006,** *6*, 3131-3148.

10. Jacobson, M. Z., Climate response of fossil fuel and biofuel soot, accounting for soot's feedback to snow and sea ice albedo and emissivity. *Journal of Geophysical Research-Atmospheres* **2004,** *109* (D21), 15.
11. Chung, S. H.; Seinfeld, J. H., Global distribution and climate forcing of carbonaceous aerosols. *Journal of Geophysical Research-Atmospheres* **2002,** *107* (D19), 33.
12. Feng, Y.; Ramanathan, V.; Kotamarthi, V. R., Brown carbon: a significant atmospheric absorber of solar radiation? *Atmospheric Chemistry and Physics* **2013,** *13* (17), 8607-8621.
13. Pedersen, C. A.; Gallet, J. C.; Strom, J.; Gerland, S.; Hudson, S. R.; Forsstrom, S.; Isaksson, E.; Berntsen, T. K., In situ observations of black carbon in snow and the corresponding spectral surface albedo reduction. *Journal of Geophysical Research-Atmospheres* **2015,** *120* (4), 1476-1489.
14. Zhang, Y. L.; Kang, S. C.; Sprenger, M.; Cong, Z. Y.; Gao, T. G.; Li, C. L.; Tao, S.; Li, X. F.; Zhong, X. Y.; Xu, M.; Meng, W. J.; Neupane, B.; Qin, X.; Sillanpaa, M., Black carbon and mineral dust in snow cover on the Tibetan Plateau. *Cryosphere* **2018,** *12* (2), 413-431.
15. Hansen, A. D. A.; Rosen, H.; Novakov, T., THE AETHALOMETER - AN INSTRUMENT FOR THE REAL-TIME MEASUREMENT OF OPTICAL-ABSORPTION BY AEROSOL-PARTICLES. *Science of the Total Environment* **1984,** *36* (JUN), 191-196.
16. Drinovec, L.; Mocnik, G.; Zotter, P.; Prevot, A. S. H.; Ruckstuhl, C.; Coz, E.; Rupakheti, M.; Sciare, J.; Muller, T.; Wiedensohler, A.; Hansen, A. D. A., The "dual-spot" Aethalometer: an improved measurement of aerosol black carbon with real-time loading compensation. *Atmospheric Measurement Techniques* **2015,** *8* (5), 1965-1979.
17. Bond, T. C.; Anderson, T. L.; Campbell, D., Calibration and intercomparison of filter-based measurements of visible light absorption by aerosols. *Aerosol Science and Technology* **1999,** *30* (6), 582-600.
18. Petzold, A.; Schloesser, H.; Sheridan, P. J.; Arnott, W. P.; Ogren, J. A.; Virkkula, A., Evaluation of multiangle absorption photometry for measuring aerosol light absorption. *Aerosol Science and Technology* **2005,** *39* (1), 40-51.
19. Coen, M. C.; Weingartner, E.; Apituley, A.; Ceburnis, D.; Fierz-Schmidhauser, R.; Flentje, H.; Henzing, J. S.; Jennings, S. G.; Moerman, M.; Petzold, A.; Schmid, O.; Baltensperger, U., Minimizing light absorption measurement artifacts of the Aethalometer: evaluation of five correction algorithms. *Atmospheric Measurement Techniques* **2010,** *3* (2), 457-474.
20. Virkkula, A.; Makela, T.; Hillamo, R.; Yli-Tuomi, T.; Hirsikko, A.; Hameri, K.; Koponen, I. K., A simple procedure for correcting loading effects of aethalometer data. *Journal of the Air & Waste Management Association* **2007,** *57* (10), 1214-1222.
21. Weingartner, E.; Saathoff, H.; Schnaiter, M.; Streit, N.; Bitnar, B.; Baltensperger, U., Absorption of light by soot particles: determination of the absorption coefficient by means of aethalometers. *Journal of Aerosol Science* **2003,** *34* (10), 1445-1463.

22. Conny, J. M.; Slater, J. F., Black carbon and organic carbon in aerosol particles from crown fires in the Canadian boreal forest. *Journal of Geophysical Research-Atmospheres* **2002,** *107* (D11).
23. Conny, J. M., The Optimization of Thermal Optical Analysis for the Measurement of Black Carbon in Regional PM2. 5: A Chemometric Approach. *US Environmental Protection Agency, Office of Research and Development, Washington, DC, Report EPA* **2007,** *600*.
24. Conny, J. M.; Norris, G. A.; Gould, T. R., Factorial-based response-surface modeling with confidence intervals for optimizing thermal-optical transmission analysis of atmospheric black carbon. *Analytica Chimica Acta* **2009,** *635* (2), 144-156.
25. Bond, T. C.; Bergstrom, R. W., Light absorption by carbonaceous particles: An investigative review. *Aerosol Science and Technology* **2006,** *40* (1), 27-67.
26. Cross, E. S.; Onasch, T. B.; Ahern, A.; Wrobel, W.; Slowik, J. G.; Olfert, J.; Lack, D. A.; Massoli, P.; Cappa, C. D.; Schwarz, J. P.; Spackman, J. R.; Fahey, D. W.; Sedlacek, A.; Trimborn, A.; Jayne, J. T.; Freedman, A.; Williams, L. R.; Ng, N. L.; Mazzoleni, C.; Dubey, M.; Brem, B.; Kok, G.; Subramanian, R.; Freitag, S.; Clarke, A.; Thornhill, D.; Marr, L. C.; Kolb, C. E.; Worsnop, D. R.; Davidovits, P., Soot Particle StudiesInstrument Inter-ComparisonProject Overview. *Aerosol Science and Technology* **2010,** *44* (8), 592-611.
27. Khalizov, A. F.; Xue, H. X.; Wang, L.; Zheng, J.; Zhang, R. Y., Enhanced Light Absorption and Scattering by Carbon Soot Aerosol Internally Mixed with Sulfuric Acid. *Journal of Physical Chemistry A* **2009,** *113* (6), 1066-1074.
28. Liu, L.; Mishchenko, M. I., Effects of aggregation on scattering and radiative properties of soot aerosols. *Journal of Geophysical Research-Atmospheres* **2005,** *110* (D11), 10.
29. Liu, S. D.; Xia, X. H.; Zhai, Y. W.; Wang, R.; Liu, T.; Zhang, S. W., Black carbon (BC) in urban and surrounding rural soils of Beijing, China: Spatial distribution and relationship with polycyclic aromatic hydrocarbons (PAHs). *Chemosphere* **2011,** *82* (2), 223-228.
30. Sasser, E., US EPA Report to Congress on Black Carbon: Department of the Interior, Environment, and Related Agencies Appropriations Act, 2010. US EPA. 2012.
31. Jacobson, M. Z., A physically-based treatment of elemental carbon optics: Implications for global direct forcing of aerosols. *Geophysical Research Letters* **2000,** *27* (2), 217-220.
32. Lack, D. A.; Moosmuller, H.; McMeeking, G. R.; Chakrabarty, R. K.; Baumgardner, D., Characterizing elemental, equivalent black, and refractory black carbon aerosol particles: a review of techniques, their limitations and uncertainties. *Analytical and Bioanalytical Chemistry* **2014,** *406* (1), 99-122.
33. Baumgardner, D.; Popovicheva, O.; Allan, J.; Bernardoni, V.; Cao, J.; Cavalli, F.; Cozic, J.; Diapouli, E.; Eleftheriadis, K.; Genberg, P. J.; Gonzalez, C.; Gysel, M.; John, A.; Kirchstetter, T. W.; Kuhlbusch, T. A. J.; Laborde, M.; Lack, D.; Muller, T.; Niessner, R.; Petzold, A.; Piazzalunga, A.; Putaud, J. P.; Schwarz, J.; Sheridan, P.; Subramanian, R.; Swietlicki, E.; Valli, G.; Vecchi, R.; Viana, M., Soot reference materials for instrument calibration and intercomparisons: a workshop

summary with recommendations. *Atmospheric Measurement Techniques* **2012,** *5* (8), 1869-1887.
34. Liu, J. M.; Scheuer, E.; Dibb, J.; Ziemba, L. D.; Thornhill, K. L.; Anderson, B. E.; Wisthaler, A.; Mikoviny, T.; Devi, J. J.; Bergin, M.; Weber, R. J., Brown carbon in the continental troposphere. *Geophysical Research Letters* **2014,** *41* (6), 2191-2195.
35. Bueno, P. A.; Havey, D. K.; Mulholland, G. W.; Hodges, J. T.; Gillis, K. A.; Dickerson, R. R.; Zachariah, M. R., Photoacoustic Measurements of Amplification of the Absorption Cross Section for Coated Soot Aerosols. *Aerosol Science and Technology* **2011,** *45* (10), 1217-1230.
36. Havey, D. K.; Bueno, P. A.; Gillis, K. A.; Hodges, J. T.; Mulholland, G. W.; van Zee, R. D.; Zachariah, M. R., Photoacoustic Spectrometer with a Calculable Cell Constant for Measurements of Gases and Aerosols. *Analytical Chemistry* **2010,** *82* (19), 7935-7942.
37. Bond, T. C.; Streets, D. G.; Yarber, K. F.; Nelson, S. M.; Woo, J. H.; Klimont, Z., A technology-based global inventory of black and organic carbon emissions from combustion. *Journal of Geophysical Research-Atmospheres* **2004,** *109* (D14), 43.
38. Goldberg, E. D., Black carbon in the environment: properties and distribution. **1985**.
39. Hoffer, A.; Gelencser, A.; Guyon, P.; Kiss, G.; Schmid, O.; Frank, G. P.; Artaxo, P.; Andreae, M. O., Optical properties of humic-like substances (HULIS) in biomass-burning aerosols. *Atmospheric Chemistry and Physics* **2006,** *6*, 3563-3570.
40. Clarke, A. D.; Shinozuka, Y.; Kapustin, V. N.; Howell, S.; Huebert, B.; Doherty, S.; Anderson, T.; Covert, D.; Anderson, J.; Hua, X.; Moore, K. G.; McNaughton, C.; Carmichael, G.; Weber, R., Size distributions and mixtures of dust and black carbon aerosol in Asian outflow: Physiochemistry and optical properties. *Journal of Geophysical Research-Atmospheres* **2004,** *109* (D15), 20.
41. Lack, D. A.; Quinn, P. K.; Massoli, P.; Bates, T. S.; Coffman, D.; Covert, D. S.; Sierau, B.; Tucker, S.; Baynard, T.; Lovejoy, E.; Murphy, D. M.; Ravishankara, A. R., Relative humidity dependence of light absorption by mineral dust after long-range atmospheric transport from the Sahara. *Geophysical Research Letters* **2009,** *36*, 5.
42. Yang, M.; Howell, S. G.; Zhuang, J.; Huebert, B. J., Attribution of aerosol light absorption to black carbon, brown carbon, and dust in China - interpretations of atmospheric measurements during EAST-AIRE. *Atmospheric Chemistry and Physics* **2009,** *9* (6), 2035-2050.
43. Sokolik, I. N.; Toon, O. B., Incorporation of mineralogical composition into models of the radiative properties of mineral aerosol from UV to IR wavelengths. *Journal of Geophysical Research-Atmospheres* **1999,** *104* (D8), 9423-9444.
44. Alfaro, S. C.; Lafon, S.; Rajot, J. L.; Formenti, P.; Gaudichet, A.; Maille, M., Iron oxides and light absorption by pure desert dust: An experimental study. *Journal of Geophysical Research-Atmospheres* **2004,** *109* (D8), 9.
45. Colbeck, I., *Environmental chemistry of aerosols*. Blackwell Pub.: 2008.
46. Arnott, W. P.; Hamasha, K.; Moosmuller, H.; Sheridan, P. J.; Ogren, J. A., Towards aerosol light-absorption measurements with a 7-wavelength Aethalometer:

Evaluation with a photoacoustic instrument and 3-wavelength nephelometer. *Aerosol Science and Technology* **2005,** *39* (1), 17-29.
47. Schmid, O.; Artaxo, P.; Arnott, W. P.; Chand, D.; Gatti, L. V.; Frank, G. P.; Hoffer, A.; Schnaiter, M.; Andreae, M. O., Spectral light absorption by ambient aerosols influenced by biomass burning in the Amazon Basin. I: Comparison and field calibration of absorption measurement techniques. *Atmospheric Chemistry and Physics* **2006,** *6*, 3443-3462.
48. Scientific, M., Aethalometer® Model AE33 User Manual-Version 1.54. *Aerosol doo, Ljubljana, Slovenia* **2016**.
49. Bond, T. C.; Bussemer, M.; Wehner, B.; Keller, S.; Charlson, R. J.; Heintzenberg, J., Light absorption by primary particle emissions from a lignite burning plant. *Environmental Science & Technology* **1999,** *33* (21), 3887-3891.
50. Laborde, M.; Schnaiter, M.; Linke, C.; Saathoff, H.; Naumann, K. H.; Mohler, O.; Berlenz, S.; Wagner, U.; Taylor, J. W.; Liu, D.; Flynn, M.; Allan, J. D.; Coe, H.; Heimerl, K.; Dahlkotter, F.; Weinzierl, B.; Wollny, A. G.; Zanatta, M.; Cozic, J.; Laj, P.; Hitzenberger, R.; Schwarz, J. P.; Gysel, M., Single Particle Soot Photometer intercomparison at the AIDA chamber. *Atmospheric Measurement Techniques* **2012,** *5* (12), 3077-3097.
51. Laborde, M.; Mertes, P.; Zieger, P.; Dommen, J.; Baltensperger, U.; Gysel, M., Sensitivity of the Single Particle Soot Photometer to different black carbon types. *Atmospheric Measurement Techniques* **2012,** *5* (5), 1031-1043.
52. Sedlacek, A. *Single-Particle Soot Photometer (SP2) Instrument Handbook*; DOE Office of Science Atmospheric Radiation Measurement (ARM) Program …: 2017.
53. Schwarz, J. P.; Spackman, J. R.; Gao, R. S.; Perring, A. E.; Cross, E.; Onasch, T. B.; Ahern, A.; Wrobel, W.; Davidovits, P.; Olfert, J.; Dubey, M. K.; Mazzoleni, C.; Fahey, D. W., The Detection Efficiency of the Single Particle Soot Photometer. *Aerosol Science and Technology* **2010,** *44* (8), 612-628.
54. Gao, R. S.; Schwarz, J. P.; Kelly, K. K.; Fahey, D. W.; Watts, L. A.; Thompson, T. L.; Spackman, J. R.; Slowik, J. G.; Cross, E. S.; Han, J. H.; Davidovits, P.; Onasch, T. B.; Worsnop, D. R., A novel method for estimating light-scattering properties of soot aerosols using a modified single-particle soot photometer. *Aerosol Science and Technology* **2007,** *41* (2), 125-135.
55. Gysel, M.; Laborde, M.; Olfert, J. S.; Subramanian, R.; Grohn, A. J., Effective density of Aquadag and fullerene soot black carbon reference materials used for SP2 calibration. *Atmospheric Measurement Techniques* **2011,** *4* (12), 2851-2858.
56. Peterson, M. R.; Richards, M. H. In *Thermal-optical-transmittance analysis for organic, elemental, carbonate, total carbon, and OCX2 in PM2. 5 by the EPA/NIOSH method*, 2002; Citeseer: pp 83-1.
57. Radney, J. G.; Ma, X. F.; Gillis, K. A.; Zachariah, M. R.; Hodges, J. T.; Zangmeister, C. D., Direct Measurements of Mass-Specific Optical Cross Sections of Single-Component Aerosol Mixtures. *Analytical Chemistry* **2013,** *85* (17), 8319-8325.

58. Yao, Q.; Asa-Awuku, A.; Zangmeister, C. D.; Radney, J. G., Comparison of three essential sub-micrometer aerosol measurements: Mass, size and shape. *Aerosol Science and Technology* **2020,** *54* (10), 1197-1209.
59. Tavakoli, F.; Olfert, J. S., Determination of particle mass, effective density, mass-mobility exponent, and dynamic shape factor using an aerodynamic aerosol classifier and a differential mobility analyzer in tandem. *Journal of Aerosol Science* **2014,** *75*, 35-42.
60. Sato, M.; Hansen, J.; Koch, D.; Lacis, A.; Ruedy, R.; Dubovik, O.; Holben, B.; Chin, M.; Novakov, T., Global atmospheric black carbon inferred from AERONET. *Proceedings of the National Academy of Sciences of the United States of America* **2003,** *100* (11), 6319-6324.
61. Jiang, Y. Q.; Lu, Z.; Liu, X. H.; Qian, Y.; Zhang, K.; Wang, Y. H.; Yang, X. Q., Impacts of global open-fire aerosols on direct radiative, cloud and surface-albedo effects simulated with CAM5. *Atmospheric Chemistry and Physics* **2016,** *16* (22), 14805-14824.
62. Deng, W. J.; Zheng, H. L.; Tsui, A. K. Y.; Chen, X. W., Measurement and health risk assessment of PM2.5, flame retardants, carbonyls and black carbon in indoor and outdoor air in kindergartens in Hong Kong. *Environment International* **2016,** *96*, 65-74.
63. Schnaiter, M.; Gimmler, M.; Llamas, I.; Linke, C.; Jager, C.; Mutschke, H., Strong spectral dependence of light absorption by organic carbon particles formed by propane combustion. *Atmospheric Chemistry and Physics* **2006,** *6*, 2981-2990.
64. Mok, J.; Krotkov, N. A.; Arola, A.; Torres, O.; Jethva, H.; Andrade, M.; Labow, G.; Eck, T. F.; Li, Z. Q.; Dickerson, R. R.; Stenchikov, G. L.; Osipov, S.; Ren, X. R., Impacts of brown carbon from biomass burning on surface UV and ozone photochemistry in the Amazon Basin. *Scientific Reports* **2016,** *6*.
65. Schuster, G. L.; Dubovik, O.; Arola, A.; Eck, T. F.; Holben, B. N., Remote sensing of soot carbon - Part 2: Understanding the absorption Angstrom exponent. *Atmospheric Chemistry and Physics* **2016,** *16* (3), 1587-1602.
66. Carter, T. S.; Heald, C. L.; Jimenez, J. L.; Campuzano-Jost, P.; Kondo, Y.; Moteki, N.; Schwarz, J. P.; Wiedinmyer, C.; Darmenov, A. S.; da Silva, A. M.; Kaiser, J. W., How emissions uncertainty influences the distribution and radiative impacts of smoke from fires in North America. *Atmospheric Chemistry and Physics* **2020,** *20* (4), 2073-2097.
67. Bergstrom, R. W.; Pilewskie, P.; Russell, P. B.; Redemann, J.; Bond, T. C.; Quinn, P. K.; Sierau, B., Spectral absorption properties of atmospheric aerosols. *Atmospheric Chemistry and Physics* **2007,** *7* (23), 5937-5943.
68. Chung, C. E.; Kim, S. W.; Lee, M.; Yoon, S. C.; Lee, S., Carbonaceous aerosol AAE inferred from in-situ aerosol measurements at the Gosan ABC super site, and the implications for brown carbon aerosol. *Atmospheric Chemistry and Physics* **2012,** *12* (14), 6173-6184.
69. Zheng, H.; Kong, S. F.; Wu, F. Q.; Cheng, Y.; Niu, Z. Z.; Zheng, S. R.; Yang, G. W.; Yao, L. Q.; Yan, Q.; Wu, J.; Zheng, M. M.; Chen, N.; Xu, K.; Yan, Y. Y.; Liu, D. T.; Zhao, D. L.; Zhao, T. L.; Bai, Y. Q.; Li, S. L.; Qi, S. H., Intra-regional transport of black carbon between the south edge of the North China Plain

and central China during winter haze episodes. *Atmospheric Chemistry and Physics* **2019,** *19* (7), 4499-4516.
70. Lewis, K.; Arnott, W. P.; Moosmuller, H.; Wold, C. E., Strong spectral variation of biomass smoke light absorption and single scattering albedo observed with a novel dual-wavelength photoacoustic instrument. *Journal of Geophysical Research-Atmospheres* **2008,** *113* (D16), 14.
71. Zangmeister, C. D.; Grimes, C. D.; Dickerson, R. R.; Radney, J. G., Characterization and demonstration of a black carbon aerosol mimic for instrument evaluation. *Aerosol Science and Technology*, 12.
72. You, R.; Radney, J. G.; Zachariah, M. R.; Zangmeister, C. D., Measured Wavelength-Dependent Absorption Enhancement of Internally Mixed Black Carbon with Absorbing and Nonabsorbing Materials. *Environmental Science & Technology* **2016,** *50* (15), 7982-7990.
73. Petzold, A.; Kopp, C.; Niessner, R., The dependence of the specific attenuation cross-section on black carbon mass fraction and particle size. *Atmospheric Environment* **1997,** *31* (5), 661-672.
74. Olson, M. R.; Garcia, M. V.; Robinson, M. A.; Van Rooy, P.; Dietenberger, M. A.; Bergin, M.; Schauer, J. J., Investigation of black and brown carbon multiple-wavelength-dependent light absorption from biomass and fossil fuel combustion source emissions. *Journal of Geophysical Research-Atmospheres* **2015,** *120* (13), 6682-6697.
75. Park, S. S.; Hansen, A. D. A.; Cho, S. Y., Measurement of real time black carbon for investigating spot loading effects of Aethalometer data. *Atmospheric Environment* **2010,** *44* (11), 1449-1455.
76. Jimenez, J.; Cialborn, C.; Larson, T.; Gould, T.; Kirchstetter, T. W.; Gundel, L., Loading effect correction for real-time aethalometer measurements of fresh diesel soot. *Journal of the Air & Waste Management Association* **2007,** *57* (7), 868-873.
77. Kirchstetter, T. W.; Novakov, T., Controlled generation of black carbon particles from a diffusion flame and applications in evaluating black carbon measurement methods. *Atmospheric Environment* **2007,** *41* (9), 1874-1888.
78. Cappa, C. D.; Onasch, T. B.; Massoli, P.; Worsnop, D. R.; Bates, T. S.; Cross, E. S.; Davidovits, P.; Hakala, J.; Hayden, K. L.; Jobson, B. T.; Kolesar, K. R.; Lack, D. A.; Lerner, B. M.; Li, S. M.; Mellon, D.; Nuaaman, I.; Olfert, J. S.; Petaja, T.; Quinn, P. K.; Song, C.; Subramanian, R.; Williams, E. J.; Zaveri, R. A., Radiative Absorption Enhancements Due to the Mixing State of Atmospheric Black Carbon. *Science* **2012,** *337* (6098), 1078-1081.
79. Lack, D. A.; Richardson, M. S.; Law, D.; Langridge, J. M.; Cappa, C. D.; McLaughlin, R. J.; Murphy, D. M., Aircraft Instrument for Comprehensive Characterization of Aerosol Optical Properties, Part 2: Black and Brown Carbon Absorption and Absorption Enhancement Measured with Photo Acoustic Spectroscopy. *Aerosol Science and Technology* **2012,** *46* (5), 555-568.
80. Raju, M. P.; Safai, P. D.; Vijayakumar, K.; Devara, P. C. S.; Naidu, C. V.; Rao, P. S. P.; Pandithurai, G., Atmospheric abundances of black carbon aerosols and their radiative impact over an urban and a rural site in SW India. *Atmospheric Environment* **2016,** *125*, 429-436.

81. Martins, J. V.; Artaxo, P.; Liousse, C.; Reid, J. S.; Hobbs, P. V.; Kaufman, Y. J., Effects of black carbon content, particle size, and mixing on light absorption by aerosols from biomass burning in Brazil. *Journal of Geophysical Research-Atmospheres* **1998,** *103* (D24), 32041-32050.
82. Tumolva, L.; Park, J. Y.; Kim, J. S.; Miller, A. L.; Chow, J. C.; Watson, J. G.; Park, K., Morphological and Elemental Classification of Freshly Emitted Soot Particles and Atmospheric Ultrafine Particles using the TEM/EDS. *Aerosol Science and Technology* **2010,** *44* (3), 202-215.
83. Radney, J. G.; Zangmeister, C. D., Practical limitations of aerosol separation by a tandem differential mobility analyzer-aerosol particle mass analyzer. *Aerosol Science and Technology* **2016,** *50* (2), 160-172.
84. Lee, E. S.; Xu, B.; Zhu, Y. F., Measurements of ultrafine particles carrying different number of charges in on- and near-freeway environments. *Atmospheric Environment* **2012,** *60*, 564-572.
85. Babich, P.; Davey, M.; Allen, G.; Koutrakis, P., Method comparisons for particulate nitrate, elemental carbon, and PM2.5 mass in seven US cities. *Journal of the Air & Waste Management Association* **2000,** *50* (7), 1095-1105.
86. Saleh, R.; Hennigan, C. J.; McMeeking, G. R.; Chuang, W. K.; Robinson, E. S.; Coe, H.; Donahue, N. M.; Robinson, A. L., Absorptivity of brown carbon in fresh and photo-chemically aged biomass-burning emissions. *Atmospheric Chemistry and Physics* **2013,** *13* (15), 7683-7693.
87. Ran, L.; Deng, Z. Z.; Wang, P. C.; Xia, X. A., Black carbon and wavelength-dependent aerosol absorption in the North China Plain based on two-year aethalometer measurements. *Atmospheric Environment* **2016,** *142*, 132-144.
88. Zotter, P.; Herich, H.; Gysel, M.; El-Haddad, I.; Zhang, Y. L.; Mocnik, G.; Huglin, C.; Baltensperger, U.; Szidat, S.; Prevot, A. H., Evaluation of the absorption angstrom ngstrom exponents for traffic and wood burning in the Aethalometer-based source apportionment using radiocarbon measurements of ambient aerosol. *Atmospheric Chemistry and Physics* **2017,** *17* (6), 4229-4249.
89. Segura, S.; Estelles, V.; Titos, G.; Lyamani, H.; Utrillas, M. P.; Zotter, P.; Prevot, A. S. H.; Mocnik, G.; Alados-Arboledas, L.; Martinez-Lozano, J. A., Determination and analysis of in situ spectral aerosol optical properties by a multi-instrumental approach. *Atmospheric Measurement Techniques* **2014,** *7* (8), 2373-2387.
90. Cao, J. J.; Lee, S. C.; Ho, K. F.; Zou, S. C.; Fung, K.; Li, Y.; Watson, J. G.; Chow, J. C., Spatial and seasonal variations of atmospheric organic carbon and elemental carbon in Pearl River Delta Region, China. *Atmospheric Environment* **2004,** *38* (27), 4447-4456.
91. Shiraiwa, M.; Kondo, Y.; Iwamoto, T.; Kita, K., Amplification of Light Absorption of Black Carbon by Organic Coating. *Aerosol Science and Technology* **2010,** *44* (1), 46-54.
92. Rattigan, O. V.; Civerolo, K.; Doraiswamy, P.; Felton, H. D.; Hopke, P. K., Long Term Black Carbon Measurements at Two Urban Locations in New York. *Aerosol and Air Quality Research* **2013,** *13* (4), 1181-U305.
93. Ahmed, T.; Dutkiewicz, V. A.; Shareef, A.; Tuncel, G.; Tuncel, S.; Husain, L., Measurement of black carbon (BC) by an optical method and a thermal-optical

method: Intercomparison for four sites. *Atmospheric Environment* **2009,** *43* (40), 6305-6311.
94. Hadley, O. L.; Corrigan, C. E.; Kirchstetter, T. W., Modified Thermal-Optical Analysis Using Spectral Absorption Selectivity To Distinguish Black Carbon from Pyrolized Organic Carbon. *Environmental Science & Technology* **2008,** *42* (22), 8459-8464.
95. Khan, B.; Hays, M. D.; Geron, C.; Jetter, J., Differences in the OC/EC Ratios that Characterize Ambient and Source Aerosols due to Thermal-Optical Analysis. *Aerosol Science and Technology* **2012,** *46* (2), 127-137.
96. Conny, J. M.; Klinedinst, D. B.; Wight, S. A.; Paulsen, J. L., Optimizing thermal-optical methods for measuring atmospheric elemental (black) carbon: A response surface study. *Aerosol Science and Technology* **2003,** *37* (9), 703-723.
97. Lappi, M. K.; Ristimaki, J. M., Comparison of filter smoke number and elemental carbon from thermal optical analysis of marine diesel engine exhaust. *Proceedings of the Institution of Mechanical Engineers Part M-Journal of Engineering for the Maritime Environment* **2019,** *233* (2), 602-609.
98. Chen, L. W. A.; Chow, J. C.; Watson, J. G.; Moosmuller, H.; Arnott, W. P., Modeling reflectance and transmittance of quartz-fiber filter samples containing elemental carbon particles: Implications for thermal/optical analysis. *Journal of Aerosol Science* **2004,** *35* (6), 765-780.
99. Ammerlaan, B. A. J.; Jedynska, A. D.; Henzing, J. S.; Holzinger, R., On a possible bias in elemental carbon measurements with the Sunset thermal/optical carbon analyser caused by unstable laser signal. *Atmospheric Environment* **2015,** *122*, 571-576.
100. Birch, M. E.; Cary, R. A., Elemental carbon-based method for monitoring occupational exposures to particulate diesel exhaust. *Aerosol Science and Technology* **1996,** *25* (3), 221-241.
101. Presser, C.; Radney, J. G.; Jordan, M. L.; Nazarian, A., Simultaneous transmission and absorption photometry of carbon-black absorption from drop-cast particle-laden filters. *Aerosol Science and Technology* **2019,** *53* (5), 508-525.
102. Birch, M. E., Occupational monitoring of particulate diesel exhaust by NIOSH method 5040. *Applied Occupational and Environmental Hygiene* **2002,** *17* (6), 400-405.
103. Han, Y. M.; Chen, A.; Cao, J. J.; Fung, K.; Ho, F.; Yan, B. Z.; Zhan, C. L. L.; Liu, S. X.; Wei, C.; An, Z. S., Thermal/Optical Methods for Elemental Carbon Quantification in Soils and Urban Dusts: Equivalence of Different Analysis Protocols. *Plos One* **2013,** *8* (12), 13.
104. Park, S.; Allen, R. J., Understanding influences of convective transport and removal processes on aerosol vertical distribution. *Geophysical Research Letters* **2015,** *42* (23), 10438-10444.
105. Allen, G. A.; Lawrence, J.; Koutrakis, P., Field validation of a semi-continuous method for aerosol black carbon (aethalometer) and temporal patterns of summertime hourly black carbon measurements in southwestern PA. *Atmospheric Environment* **1999,** *33* (5), 817-823.

106. Grimes, C. D.; Coney, J. M.; Dickerson, R. R., Evaluation of Thermal Optical Analysis (TOA) using an aqueous binary mixture *Atmospheric Environment* **2020,** *in press*.
107. Zangmeister, C. D.; Grimes, C. D.; Dickerson, R. R.; Radney, J. G., Characterization and demonstration of a black carbon aerosol mimic for instrument evaluation. *Aerosol Science and Technology* **2019**.
108. Zangmeister, C. D.; Radney, J. G., Absorption Spectroscopy of Black and Brown Carbon Aerosol. In *Multiphase Environmental Chemistry in the Atmosphere*, Hunt, S. W.; Laskin, A.; Nizkorodov, S. A., Eds. 2018; Vol. 1299, pp 275-297.
109. Zangmeister, C. D.; You, R.; Lunny, E. M.; Jacobson, A. E.; Okumura, M.; Zachariah, M. R.; Radney, J. G., Measured in-situ mass absorption spectra for nine forms of highly-absorbing carbonaceous aerosol. *Carbon* **2018,** *136*, 85-93.
110. Chen, L. W. A.; Doddridge, B. G.; Dickerson, R. R.; Chow, J. C.; Mueller, P. K.; Quinn, J.; Butler, W. A., Seasonal variations in elemental carbon aerosol, carbon monoxide and sulfur dioxide: Implications for sources. *Geophysical Research Letters* **2001,** *28* (9), 1711-1714.
111. Holloway, T.; Levy, H.; Kasibhatla, P., Global distribution of carbon monoxide. *Journal of Geophysical Research-Atmospheres* **2000,** *105* (D10), 12123-12147.
112. Girach, I. A.; Nair, V. S.; Babu, S. S.; Nair, P. R., Black carbon and carbon monoxide over Bay of Bengal during W_ICARB: Source characteristics. *Atmospheric Environment* **2014,** *94*, 508-517.
113. Spackman, J. R.; Schwarz, J. P.; Gao, R. S.; Watts, L. A.; Thomson, D. S.; Fahey, D. W.; Holloway, J. S.; de Gouw, J. A.; Trainer, M.; Ryerson, T. B., Empirical correlations between black carbon aerosol and carbon monoxide in the lower and middle troposphere. *Geophysical Research Letters* **2008,** *35* (19).
114. McDonald, B. C.; Goldstein, A. H.; Harley, R. A., Long-Term Trends in California Mobile Source Emissions and Ambient Concentrations of Black Carbon and Organic Aerosol. *Environmental Science & Technology* **2015,** *49* (8), 5178-5188.
115. Dickerson, R. R.; Andreae, M. O.; Campos, T.; Mayol-Bracero, O. L.; Neususess, C.; Streets, D. G., Analysis of black carbon and carbon monoxide observed over the Indian Ocean: Implications for emissions and photochemistry. *Journal of Geophysical Research-Atmospheres* **2002,** *107* (D19).
116. Venkatachari, P.; Zhou, L. M.; Hopke, P. K.; Felton, D.; Rattigan, O. V.; Schwab, J. J.; Demerjian, K. L., Spatial and temporal variability of black carbon in New York City. *Journal of Geophysical Research-Atmospheres* **2006,** *111* (D10).
117. Masiol, M.; Hopke, P. K.; Felton, H. D.; Frank, B. P.; Rattigan, O. V.; Wurth, M.; LaDuke, G. H., Analysis of major air pollutants and submicron particles in New York City and Long Island. *Atmospheric Environment* **2017,** *148*, 203-214.
118. Kota, S. H.; Zhang, H.; Chen, G.; Schade, G. W.; Ying, Q., Evaluation of on-road vehicle CO and NOx National Emission Inventories using an urban-scale source-oriented air quality model. *Atmospheric environment* **2014,** *85*, 99-108.
119. Epa, N. E. I., National Emissions Inventory (NEI). *US Environ. Prot. Agency [Online]. Available: https://www. epa. gov/air-emissions-inventories* **2016**.

120. Solazzo, E.; Crippa, M.; Guizzardi, D.; Muntean, M.; Choulga, M.; Janssens-Maenhout, G., Uncertainties in the EDGAR emission inventory of greenhouse gases. *Atmospheric Chemistry and Physics Discussions* **2020**, 1-46.
121. Janssens-Maenhout, G.; Crippa, M.; Guizzardi, D.; Muntean, M.; Schaaf, E.; Dentener, F.; Bergamaschi, P.; Pagliari, V.; Olivier, J. G. J.; Peters, J. A. H. W., EDGAR v4. 3.2 Global Atlas of the three major greenhouse gas emissions for the period 1970–2012. *Earth System Science Data* **2019,** *11* (3), 959-1002.
122. McDonald, B. C.; McBride, Z. C.; Martin, E. W.; Harley, R. A., High-resolution mapping of motor vehicle carbon dioxide emissions. *Journal of Geophysical Research-Atmospheres* **2014,** *119* (9), 5283-5298.
123. McDonald, B. C.; Gentner, D. R.; Goldstein, A. H.; Harley, R. A., Long-Term Trends in Motor Vehicle Emissions in US Urban Areas. *Environmental Science & Technology* **2013,** *47* (17), 10022-10031.
124. McDonald, B. C.; McKeen, S. A.; Cui, Y. Y.; Ahmadov, R.; Kim, S. W.; Frost, G. J.; Pollack, I. B.; Peischl, J.; Ryerson, T. B.; Holloway, J. S.; Graus, M.; Wameke, C.; Gilman, J. B.; de Gouw, J. A.; Kaiser, J.; Keutsch, F. N.; Hanisco, T. F.; Wolfe, G. M.; Trainer, M., Modeling Ozone in the Eastern US using a Fuel-Based Mobile Source Emissions Inventory. *Environmental Science & Technology* **2018,** *52* (13), 7360-7370.
125. Harkins, C.; McDonald, B. C.; Henze, D. K. In *Evaluation and Application of Big Data Derived Datasets for High Resolution Updates to Transport Emissions in the Wake of COVID-19*, 2020; AGU.
126. Dickerson, R. R.; Delany, A. C., Modification of a commercial gas filter correlation CO detector for enhanced sensitivity. *Journal of Atmospheric and Oceanic Technology* **1988,** *5* (3), 424-431.
127. Rattigan, O. V.; Carpenter, A. C.; Civerolo, K. L.; Felton, H. D., Pollutant measurements at near road and urban background sites in New York, USA. *Atmospheric Pollution Research* **2020,** *11* (5), 859-870.
128. Crippa, M.; Oreggioni, G.; Guizzardi, D.; Muntean, M.; Schaaf, E.; Lo Vullo, E.; Solazzo, E.; Monforti-Ferrario, F.; Olivier, J. G. J.; Vignati, E., Fossil CO2 and GHG emissions of all world countries. *Luxemburg: Publication Office of the European Union* **2019**.
129. Ahmed, T.; Dutkiewicz, V. A.; Khan, A. J.; Husain, L., Long term trends in Black Carbon Concentrations in the Northeastern United States. *Atmospheric Research* **2014,** *137*, 49-57.
130. Wang, Z.; Wang, T.; Gao, R.; Xue, L. K.; Guo, J.; Zhou, Y.; Nie, W.; Wang, X. F.; Xu, P. J.; Gao, J. A.; Zhou, X. H.; Wang, W. X.; Zhang, Q. Z., Source and variation of carbonaceous aerosols at Mount Tai, North China: Results from a semi-continuous instrument. *Atmospheric Environment* **2011,** *45* (9), 1655-1667.
131. Wang, F.; Li, Z. Q.; Ren, X. R.; Jiang, Q.; He, H.; Dickerson, R. R.; Dong, X. B.; Lv, F., Vertical distributions of aerosol optical properties during the spring 2016 ARIAs airborne campaign in the North China Plain. *Atmospheric Chemistry and Physics* **2018,** *18* (12), 8995-9010.
132. Green, D.; Alexander, J.; Fuller, G.; Quincey, P.; Butterfield, D., Marylebone Road aethalometer trial report. *King's College London* **2007**.

133. Jennings, S. G.; Spain, T. G.; Doddridge, B. G.; Maring, H.; Kelly, B. P.; Hansen, A. D. A., Concurrent measurements of black carbon aerosol and carbon monoxide at Mace Head. *Journal of Geophysical Research-Atmospheres* **1996,** *101* (D14), 19447-19454.
134. Pan, X. L.; Kanaya, Y.; Wang, Z. F.; Liu, Y.; Pochanart, P.; Akimoto, H.; Sun, Y. L.; Dong, H. B.; Li, J.; Irie, H.; Takigawa, M., Correlation of black carbon aerosol and carbon monoxide in the high-altitude environment of Mt. Huang in Eastern China. *Atmospheric Chemistry and Physics* **2011,** *11* (18), 9735-9747.
135. Subramanian, R.; Kok, G. L.; Baumgardner, D.; Clarke, A.; Shinozuka, Y.; Campos, T. L.; Heizer, C. G.; Stephens, B. B.; de Foy, B.; Voss, P. B.; Zaveri, R. A., Black carbon over Mexico: the effect of atmospheric transport on mixing state, mass absorption cross-section, and BC/CO ratios. *Atmospheric Chemistry and Physics* **2010,** *10* (1), 219-237.
136. Han, S.; Kondo, Y.; Oshima, N.; Takegawa, N.; Miyazaki, Y.; Hu, M.; Lin, P.; Deng, Z.; Zhao, Y.; Sugimoto, N.; Wu, Y., Temporal variations of elemental carbon in Beijing. *Journal of Geophysical Research-Atmospheres* **2009,** *114*, 16.
137. Baumgardner, D.; Raga, G.; Peralta, O.; Rosas, I.; Castro, T.; Kuhlbusch, T.; John, A.; Petzold, A., Diagnosing black carbon trends in large urban areas using carbon monoxide measurements. *Journal of Geophysical Research-Atmospheres* **2002,** *107* (D21).
138. Pollack, I. B.; Ryerson, T. B.; Trainer, M.; Parrish, D. D.; Andrews, A. E.; Atlas, E. L.; Blake, D. R.; Brown, S. S.; Commane, R.; Daube, B. C.; de Gouw, J. A.; Dube, W. P.; Flynn, J.; Frost, G. J.; Gilman, J. B.; Grossberg, N.; Holloway, J. S.; Kofler, J.; Kort, E. A.; Kuster, W. C.; Lang, P. M.; Lefer, B.; Lueb, R. A.; Neuman, J. A.; Nowak, J. B.; Novelli, P. C.; Peischl, J.; Perring, A. E.; Roberts, J. M.; Santoni, G.; Schwarz, J. P.; Spackman, J. R.; Wagner, N. L.; Warneke, C.; Washenfelder, R. A.; Wofsy, S. C.; Xiang, B., Airborne and ground-based observations of a weekend effect in ozone, precursors, and oxidation products in the California South Coast Air Basin. *Journal of Geophysical Research-Atmospheres* **2012,** *117*.
139. Gomez-Pelaez, A. J.; Ramos, R.; Cuevas, E.; Gomez-Trueba, V.; Reyes, E., Atmospheric CO2, CH4, and CO with the CRDS technique at the Izana Global GAW station: instrumental tests, developments, and first measurement results. *Atmospheric Measurement Techniques* **2019,** *12* (4), 2043-2066.
140. Meng, J.; Liu, J. F.; Guo, S.; Li, J. S.; Li, Z.; Tao, S., Trend and driving forces of Beijing's black carbon emissions from sectoral perspectives. *Journal of Cleaner Production* **2016,** *112*, 1272-1281.
141. Bano, T.; Singh, S.; Gupta, N. C.; Soni, K.; Tanwar, R. S.; Nath, S.; Arya, B. C.; Gera, B. S., Variation in aerosol black carbon concentration and its emission estimates at the mega-city Delhi. *International Journal of Remote Sensing* **2011,** *32* (21), 6749-6764.
142. Ackerman, A. S.; Toon, O. B.; Stevens, D. E.; Heymsfield, A. J.; Ramanathan, V.; Welton, E. J., Reduction of tropical cloudiness by soot. *Science* **2000,** *288* (5468), 1042-1047.

143. Lighty, J. S.; Veranth, J. M.; Sarofim, A. F., Combustion aerosols: Factors governing their size and composition and implications to human health. *Journal of the Air & Waste Management Association* **2000,** *50* (9), 1565-1618.
144. Knox, A.; Evans, G. J.; Brook, J. R.; Yao, X.; Jeong, C. H.; Godri, K. J.; Sabaliauskas, K.; Slowik, J. G., Mass Absorption Cross-Section of Ambient Black Carbon Aerosol in Relation to Chemical Age. *Aerosol Science and Technology* **2009,** *43* (6), 522-532.
145. Cui, X. J.; Wang, X. F.; Yang, L. X.; Chen, B.; Chen, J. M.; Andersson, A.; Gustafsson, O., Radiative absorption enhancement from coatings on black carbon aerosols. *Science of the Total Environment* **2016,** *551*, 51-56.
146. Liousse, C.; Cachier, H.; Jennings, S. G., OPTICAL AND THERMAL MEASUREMENTS OF BLACK CARBON AEROSOL CONTENT IN DIFFERENT ENVIRONMENTS - VARIATION OF THE SPECIFIC ATTENUATION CROSS-SECTION, SIGMA (SIGMA). *Atmospheric Environment Part a-General Topics* **1993,** *27* (8), 1203-1211.
147. Carrico, C. M.; Bergin, M. H.; Xu, J.; Baumann, K.; Maring, H., Urban aerosol radiative properties: Measurements during the 1999 Atlanta Supersite Experiment. *Journal of Geophysical Research-Atmospheres* **2003,** *108* (D7), 17.
148. Nordmann, S.; Birmili, W.; Weinhold, K.; Muller, K.; Spindler, G.; Wiedensohler, A., Measurements of the mass absorption cross section of atmospheric soot particles using Raman spectroscopy. *Journal of Geophysical Research-Atmospheres* **2013,** *118* (21), 12075-12085.
149. Benish, S. E.; He, H.; Ren, X.; Roberts, S. J.; Salawitch, R. J.; Li, Z.; Wang, F.; Wang, Y.; Zhang, F.; Shao, M., Measurement Report: Aircraft Observations of Ozone, Nitrogen Oxides, and Volatile Organic Compounds over Hebei Province, China. *Atmospheric Chemistry and Physics Discussions* **2020**, 1-32.
150. Ren, X. R.; Hall, D. L.; Vinciguerra, T.; Benish, S. E.; Stratton, P. R.; Ahn, D.; Hansford, J. R.; Fuentes, J. D.; Cohen, M. D.; Sahu, S.; He, H.; Grimes, C.; Salawitch, R. J.; Ehrman, S. H.; Dickerson, R. R., Methane emissions from the Marcellus Shale in southwestern Pennsylvania and northern West Virginia based on airborne measurements. *Journal of Geophysical Research-Atmospheres* **2019**.
151. Draxler, R. R.; Hess, G. D., Description of the HYSPLIT4 modeling system. **1997**.
152. Stein, A. F.; Draxler, R. R.; Rolph, G. D.; Stunder, B. J. B.; Cohen, M. D.; Ngan, F., NOAA'S HYSPLIT ATMOSPHERIC TRANSPORT AND DISPERSION MODELING SYSTEM. *Bulletin of the American Meteorological Society* **2015,** *96* (12), 2059-2077.
153. Sinha, P. R.; Kondo, Y.; Koike, M.; Ogren, J. A.; Jefferson, A.; Barrett, T. E.; Sheesley, R. J.; Ohata, S.; Moteki, N.; Coe, H.; Liu, D.; Irwin, M.; Tunved, P.; Quinn, P. K.; Zhao, Y., Evaluation of ground-based black carbon measurements by filter-based photometers at two Arctic sites. *Journal of Geophysical Research-Atmospheres* **2017,** *122* (6), 3544-3572.
154. Lee, J. E.; Dubey, M. K.; Aiken, A. C.; Chylek, P.; Carrico, C. M., Optical and Chemical Analysis of Absorption Enhancement by Mixed Carbonaceous Aerosols in the 2019 Woodbury, AZ, Fire Plume. *Journal of Geophysical Research-Atmospheres* **2020,** *125* (15), 19.

155. Sun, J. Y.; Wu, C.; Wu, D.; Cheng, C. L.; Li, M.; Li, L.; Deng, T.; Yu, J. Z.; Li, Y. J.; Zhou, Q. N.; Liang, Y.; Sun, T. L.; Song, L.; Cheng, P.; Yang, W. D.; Pei, C. L.; Chen, Y. N.; Cen, Y. X.; Nian, H. Q.; Zhou, Z., Amplification of black carbon light absorption induced by atmospheric aging: temporal variation at seasonal and diel scales in urban Guangzhou. *Atmospheric Chemistry and Physics* **2020,** *20* (4), 2445-2470.
156. Tian, P. F.; Zhang, L.; Ma, J. M.; Tang, K.; Xu, L. L.; Wang, Y.; Cao, X. J.; Liang, J. N.; Ji, Y. M.; Jiang, J. H.; Yung, Y. L.; Zhang, R. Y., Radiative absorption enhancement of dust mixed with anthropogenic pollution over East Asia. *Atmospheric Chemistry and Physics* **2018,** *18* (11), 7815-7825.
157. Cho, C.; Kim, S. W.; Lee, M.; Lim, S.; Fang, W. Z.; Gustafsson, O.; Andersson, A.; Park, R. J.; Sheridan, P. J., Observation-based estimates of the mass absorption cross-section of black and brown carbon and their contribution to aerosol light absorption in East Asia. *Atmospheric Environment* **2019,** *212*, 65-74.
158. Cappa, C. D.; Zhang, X. L.; Russell, L. M.; Collier, S.; Lee, A. K. Y.; Chen, C. L.; Betha, R.; Chen, S. J.; Liu, J.; Price, D. J.; Sanchez, K. J.; McMeeking, G. R.; Williams, L. R.; Onasch, T. B.; Worsnop, D. R.; Abbatt, J.; Zhang, Q., Light Absorption by Ambient Black and Brown Carbon and its Dependence on Black Carbon Coating State for Two California, USA, Cities in Winter and Summer. *Journal of Geophysical Research-Atmospheres* **2019,** *124* (3), 1550-1577.
159. Kahnert, M.; Kanngießer, F., Modelling optical properties of atmospheric black carbon aerosols. *Journal of Quantitative Spectroscopy and Radiative Transfer* **2020,** *244*, 106849.
160. Yadav, S.; Satsangi, P. G., Characterization of particulate matter and its related metal toxicity in an urban location in South West India. *Environmental Monitoring and Assessment* **2013,** *185* (9), 7365-7379.
161. Feng, Y. L.; Chen, Y. J.; Guo, H.; Zhi, G. R.; Xiong, S. C.; Li, J.; Sheng, G. Y.; Fu, J. M., Characteristics of organic and elemental carbon in PM2.5 samples in Shanghai, China. *Atmospheric Research* **2009,** *92* (4), 434-442.
162. Chow, J. C.; Watson, J. G.; Chen, L. W. A.; Arnott, W. P.; Moosmuller, H.; Fung, K., Equivalence of elemental carbon by thermal/optical reflectance and transmittance with different temperature protocols. *Environmental Science & Technology* **2004,** *38* (16), 4414-4422.
163. Lappi, M. K.; Ristimaki, J. M., Evaluation of thermal optical analysis method of elemental carbon for marine fuel exhaust. *Journal of the Air & Waste Management Association* **2017,** *67* (12), 1298-1318.
164. Wang, Y. P.; Wang, Z. F.; Yu, C.; Zhu, S. Y.; Cheng, L. X.; Zhang, Y.; Chen, L. F., Validation of OMI HCHO Products Using MAX-DOAS observations from 2010 to 2016 in Xianghe, Beijing: Investigation of the Effects of Aerosols on Satellite Products. *Remote Sensing* **2019,** *11* (2).
165. Conny, J. M.; Collins, S. M.; Herzing, A. A., Qualitative Multiplatform Microanalysis of Individual Heterogeneous Atmospheric Particles from High-Volume Air Samples. *Analytical Chemistry* **2014,** *86* (19), 9709-9716.

166. Xie, R. K.; Seip, H. M.; Liu, L.; Zhang, D. S., Characterization of individual airborne particles in Taiyuan City, China. *Air Quality Atmosphere and Health* **2009,** *2* (3), 123-131.
167. Genga, A.; Baglivi, F.; Siciliano, M.; Siciliano, T.; Tepore, M.; Micocci, G.; Tortorella, C.; Aiello, D., SEM-EDS investigation on PM10 data collected in Central Italy: Principal Component Analysis and Hierarchical Cluster Analysis. *Chemistry Central Journal* **2012,** *6*, 15.
168. Xie, R. K.; Seip, H. M.; Leinum, J. R.; Winje, T.; Xiao, J. S., Chemical characterization of individual particles (PM10) from ambient air in Guiyang City, China. *Science of the Total Environment* **2005,** *343* (1-3), 261-272.
169. Ault, A. P.; Peters, T. M.; Sawvel, E. J.; Casuccio, G. S.; Willis, R. D.; Norris, G. A.; Grassian, V. H., Single-Particle SEM-EDX Analysis of Iron-Containing Coarse Particulate Matter in an Urban Environment: Sources and Distribution of Iron within Cleveland, Ohio. *Environmental Science & Technology* **2012,** *46* (8), 4331-4339.
170. Dorozhkin, S. V.; Epple, M., Biological and medical significance of calcium phosphates. *Angewandte Chemie-International Edition* **2002,** *41* (17), 3130-3146.
171. Schauer, J. J., Evaluation of elemental carbon as a marker for diesel particulate matter. *Journal of Exposure Science & Environmental Epidemiology* **2003,** *13* (6), 443-453.
172. Schauer, J. J.; Park, J.; Duvall, R.; Bae, M.; Shafer, M. M.; Chuang, P.; Kim, Y. J., Measurement of Organic and Inorganic Chemical Tracers for Source Apportionment of Tropospheric Aerosols Collected During the ACE-Asia Experiment. *AGUFM* **2001,** *2001*, A21A-0058.
173. Feng, J. L.; Hu, M.; Chan, C. K.; Lau, P. S.; Fang, M.; He, L. Y.; Tang, X. Y., A comparative study of the organic matter in PM2.5 from three Chinese megacities in three different climatic zones. *Atmospheric Environment* **2006,** *40* (21), 3983-3994.
174. Duan, J. C.; Tan, J. H.; Cheng, D. X.; Bi, X. H.; Deng, W. J.; Sheng, G. Y.; Fu, J. M.; Wong, M. H., Sources and characteristics of carbonaceous aerosol in two largest cities in Pearl River Delta Region, China. *Atmospheric Environment* **2007,** *41* (14), 2895-2903.
175. Yang, H.; Yu, J. Z.; Ho, S. S. H.; Xu, J. H.; Wu, W. S.; Wan, C. H.; Wang, X. D.; Wang, X. R.; Wang, L. S., The chemical composition of inorganic and carbonaceous materials in PM2.5 in Nanjing, China. *Atmospheric Environment* **2005,** *39* (20), 3735-3749.
176. Viana, M.; Maenhaut, W.; ten Brink, H. M.; Chi, X.; Weijers, E.; Querol, X.; Alastuey, A.; Mikuska, P.; Vecera, Z., Comparative analysis of organic and elemental carbon concentrations in carbonaceous aerosols in three European cities. *Atmospheric Environment* **2007,** *41* (28), 5972-5983.
177. Lonati, G.; Ozgen, S.; Giugliano, M., Primary and secondary carbonaceous species in PM2.5 samples in Milan (Italy). *Atmospheric Environment* **2007,** *41* (22), 4599-4610.
178. Meng, Z. Y.; Jiang, X. M.; Yan, P.; Lin, W. L.; Zhang, H. D.; Wang, Y., Characteristics and sources of PM2.5 and carbonaceous species during winter in Taiyuan, China. *Atmospheric Environment* **2007,** *41* (32), 6901-6908.

179. Streets, D. G.; Gupta, S.; Waldhoff, S. T.; Wang, M. Q.; Bond, T. C.; Bo, Y. Y., Black carbon emissions in China. *Atmospheric Environment* **2001,** *35* (25), 4281-4296.